# A Study on High-Density Photonic Integrated Circuits for Optical Packet Routing

**Yuhei Ishizaka**

Graduate School of Information Science and Technology
Hokkaido University

This dissertation is submitted for the degree of
*Doctor of Philosophy in Engineering*

# TABLE OF CONTENTS

# Chapter 1

# Introduction

In recent years, a rapid increase in communication traffic has caused an upsurge in device power consumption, which has created a bottleneck effect in telecommunication networks. Electrical packet routers require high power consumption due to optical-to-electrical (O/E) and electrical-to-optical (E/O) conversions. To avoid this redundant procedure, optical packet routing technologies have been widely studied [1-3]. However, conventional packet routing components are not adapted to coherent optical communications, and the integration of the components has not been sufficiently investigated. Therefore, construction of a high-density photonic integrated circuit with coherent detection to increase communication capacity and reduce power consumption in optical packet routing is needed.

In packet switching systems for coherent optical communications, multi-level phase-shift-keying (MPSK) and binary-phase-shift-keying (BPSK) can be employed for the payload and the label, respectively. Because the BPSK signal is the binary logic, it is suited to the label processing by means of optical logic gates. When considering optical packet switching systems for coherent optical communications, most of conventional optical logic gates cannot process the BPSK signal because the conventional optical logic gates [4-15] are operated by employing optical intensity on logical value. Note that, although some optical logic gates for differential-phase-shift-keying have been reported, they are not aimed at coherent detection [16-18]. In this thesis, optical XOR, XNOR, NAND, and OR logic gates with coherent detection for the BPSK signal are presented. The presented optical logic gates are created by connecting 3-dB multi-mode interference waveguides. Additionally, architecture of reconfigurable logic operation is proposed to design flexible circuits.

To achieve a high-density integration of these logic gates, structures of transmission-efficient crossing and bent waveguides should be constructed using silicon-based optical waveguides. Moreover, athermal operation of the devices is required because power saving can be achieved without using Peltier elements or heaters. Among silicon-based optical waveguides, slot waveguides can strongly confine light to the low-index sub-wavelength scale region [19, 20], which can enhance light-matter interactions. Due to the selectiveness of covered low-index materials, slot waveguides are used as athermal waveguides [21, 22]. To date, a design method for transmission-efficient crossing slot waveguides has been reported [23]. However, the numerical results of the conventional study

were obtained from two-dimensional (2-D) simulations based on the finite-difference time-domain (FDTD) method, which assumes infinite core height. In this thesis, a three-dimensional (3-D) vector finite-element method (VFEM) for the waveguide discontinuity problem is developed to analyze a crossing slot waveguide with a finite core height. Through the use of the 3-D VFEM, the transmission characteristics of the crossing slot waveguide with the finite core height is investigated; and the radiation loss caused by the conventional crossing structure due to the mode field mismatch is revealed. To avoid the radiation loss, a transmission-efficient 3-D crossing slot waveguide with a vertical coupler is presented. Additionally, a bent slot waveguide with an asymmetric slot is proposed to realize sharp bends.

When considering further integration, the optical diffraction limit in silicon slot waveguides restricts the scale down of the waveguides. Recently, nanoscale optical waveguides based on surface plasmon polariton (SPP) to overcome this limitation have been attracted much attention because the SPP mode is strongly localized in the nanoscale region [24-36]. Because hybrid plasmonic waveguides (HPWs) achieve sub-wavelength confinement and are able to mitigate the problem of propagation loss [31-36], they are expected to serve as the basic waveguides of next-generation photonic integrated circuits. Although most studies on plasmonic waveguides have concentrated on using the plasmonic mode, it has been reported that the use of the metal-assisted photonic mode has an advantage in the realization of the sharp bend [37, 38]. This thesis reveals that the minor electric field component of the metal-assisted photonic mode contributes to the excitation of SPP. It also investigates the bending characteristics of the metal-assisted photonic mode in Si-based HPW.

The structure of this thesis is as follows: The background and objective of the thesis is given in this chapter. The formulations of the 2-D VFEM for the guided mode analysis and the 2-D finite-element method for the waveguide discontinuity problem are presented in Chapter 2. In Chapter 3, design methods of optical XOR, XNOR, NAND, and OR logic gates with coherent detection for the BPSK signal are presented. In Chapter 4, a 3-D VFEM for the waveguide discontinuity problem is formulated. Through the use of the 3-D VFEM, transmission characteristics of two types of crossing slot-waveguides with finite core height are investigated. In Chapter 5, transmission-efficient structures of bent silicon slot waveguide and crossing silicon slot waveguide for compact silicon slot waveguide-based circuits are presented. In Chapter 6, it is revealed that SPP occurs by the minor electric field component in the metal-assisted photonic mode. Modal properties, and bending and coupling characteristics of the metal-assisted photonic mode in a Si-based HPW are investigated. Finally, the findings of this study are summarized in Chapter 7.

# Chapter 2

# Finite Element Methods

## 2.1 Introduction

The finite-element method (FEM) is one of the useful numerical techniques because the size of the mesh can be adaptively configured, and the mesh can be adapted for various forms. In this chapter, the two-dimensional (2-D) vector FEM (VFEM) for the mode analysis [39] and the 2-D FEM for the waveguide discontinuity problem are formulated [40].

## 2.2 Basic Equations for Light Waves

### 2.2.1 Maxwell's Equations

Light is an electromagnetic wave phenomenon. Its magnetic field is represented by four electromagnetic field vectors that are functions of position $r$ [m] and time $t$ [s]. The four vectors, which are the electric filed $\boldsymbol{E}$ [V/m], magnetic field $\boldsymbol{H}$ [A/m], electric flux density $\boldsymbol{D}$ [C/m$^2$], and magnetic flux density $\boldsymbol{B}$ [Wb/m$^2$], conform to Maxwell's equations:

$$\nabla \times \boldsymbol{E} = -\frac{\partial \boldsymbol{B}}{\partial t}, \tag{2.1}$$

$$\nabla \times \boldsymbol{H} = \frac{\partial \boldsymbol{D}}{\partial t} + \boldsymbol{J}, \tag{2.2}$$

where $\boldsymbol{J}$ [A/m$^2$] is the electric current density. The following current continuity equation (conservation of charge equation) holds for $\boldsymbol{J}$ and the charge density $\rho$ [C/m$^3$]:

$$\nabla \cdot \boldsymbol{J} = -\frac{\partial \rho}{\partial t}. \tag{2.3}$$

From (2.1)-(2.3) and the vector formulas:

$$\nabla \cdot (\nabla \times \boldsymbol{E}) = 0, \tag{2.4}$$

$$\nabla \cdot (\nabla \times \boldsymbol{H}) = 0, \tag{2.5}$$

we obtain

$$\nabla \cdot \boldsymbol{B} = 0, \tag{2.6}$$

$$\nabla \cdot \boldsymbol{D} = \rho. \tag{2.7}$$

(2.1), (2.2), (2.6), and (2.7) are generally called Maxwell's equations. The flow density of the energy carried by electromagnetic filed is expressed by the Poynting vector $\boldsymbol{S}$ [W/m$^2$], which is defined as

$$\boldsymbol{S} = \boldsymbol{E} \times \boldsymbol{H}. \tag{2.8}$$

### 2.2.2 Constitutive Relations

If the medium is anisotropic, linear, and non-dispersive, constitutive relations are given by

$$\boldsymbol{D} = [\varepsilon]\boldsymbol{E} = \varepsilon_0[\varepsilon_{\mathrm{r}}]\boldsymbol{E}, \tag{2.9}$$

$$\boldsymbol{B} = [\mu]\boldsymbol{H} = \mu_0[\mu_{\mathrm{r}}]\boldsymbol{H}, \tag{2.10}$$

where $[\varepsilon]$ and $[\mu]$ are the permittivity and permeability tensors, and $[\varepsilon_{\mathrm{r}}]$ and $[\mu_{\mathrm{r}}]$ are the relative permittivity and the relative permeability tensors, respectively. In addition, $\varepsilon_0$ [F/m] and $\mu_0$ [H/m] are the permittivity and the permeability in free space, respectively, and their values are

$$\varepsilon_0 = 8.8541878 \times 10^{-12}, \tag{2.11}$$

$$\mu_0 = 4\pi \times 10^{-7}. \tag{2.12}$$

### 2.2.3 Wave Equations

When assuming an electromagnetic wave with unit angular frequency $\omega$ [rad/s] and introducing the electric field $\widetilde{\boldsymbol{E}}$, magnetic field $\widetilde{\boldsymbol{H}}$, electric flux density $\widetilde{\boldsymbol{D}}$, and magnetic flux density $\widetilde{\boldsymbol{B}}$, which are indicated as phasors (complex amplitude), four electromagnetic vectors express as

$$\boldsymbol{E}(\boldsymbol{r},t) = \mathrm{Re}\left[\widetilde{\boldsymbol{E}}(\boldsymbol{r})\exp(j\omega t)\right], \tag{2.13}$$

$$\boldsymbol{H}(\boldsymbol{r},t) = \mathrm{Re}\left[\widetilde{\boldsymbol{H}}(\boldsymbol{r})\exp(j\omega t)\right], \tag{2.14}$$

$$\boldsymbol{D}(\boldsymbol{r},t) = \mathrm{Re}\big[\,\widetilde{\boldsymbol{D}}(\boldsymbol{r})\exp(\,j\omega t)\big], \tag{2.15}$$

$$\boldsymbol{B}(\boldsymbol{r},t) = \mathrm{Re}\big[\,\widetilde{\boldsymbol{B}}(\boldsymbol{r})\exp(\,j\omega t)\big]. \tag{2.16}$$

By re-expressing them as $\boldsymbol{E}$, $\boldsymbol{H}$, $\boldsymbol{D}$, and $\boldsymbol{B}$, Maxwell's equations become

$$\nabla\times\boldsymbol{E} = -j\omega\boldsymbol{B} = -j\omega[\,\mu\,]\boldsymbol{H} = -j\omega\mu_0[\,\mu_\mathrm{r}\,]\boldsymbol{H}, \tag{2.17}$$

$$\nabla\times\boldsymbol{H} = j\omega\boldsymbol{D} + \boldsymbol{J} = j\omega[\,\varepsilon\,]\boldsymbol{E} + \boldsymbol{J} = j\omega\varepsilon_0[\,\varepsilon_\mathrm{r}\,]\boldsymbol{E} + \boldsymbol{J}, \tag{2.18}$$

$$\nabla\cdot\boldsymbol{D} = \nabla\cdot([\,\varepsilon\,]\boldsymbol{E}\,) = \varepsilon_0\nabla\cdot([\,\varepsilon_\mathrm{r}\,]\boldsymbol{E}\,) = \rho, \tag{2.19}$$

$$\nabla\cdot\boldsymbol{B} = \nabla\cdot([\,\mu\,]\boldsymbol{H}\,) = \mu_0\nabla\cdot([\,\mu_\mathrm{r}\,]\boldsymbol{H}\,) = 0. \tag{2.20}$$

Deleting $\boldsymbol{H}$ or $\boldsymbol{E}$ from (2.17) and (2.18), the following inhomogeneous wave equations are given:

$$\nabla\times\Big([\,\mu_\mathrm{r}\,]^{-1}\nabla\times\boldsymbol{E}\Big) - k_0^2[\,\varepsilon_\mathrm{r}\,]\boldsymbol{E} = j\omega\mu_0\boldsymbol{J}, \tag{2.21}$$

$$\nabla\times\Big([\,\varepsilon_\mathrm{r}\mu_\mathrm{r}\,]^{-1}\nabla\times\boldsymbol{H}\Big) - k_0^2[\,\mu_\mathrm{r}\,]\boldsymbol{H} = -\nabla\times\Big([\,\varepsilon_\mathrm{r}\,]^{-1}\boldsymbol{J}\Big), \tag{2.22}$$

where $k_0$ [rad/m] is

$$k_0 = \omega\sqrt{\varepsilon_0\mu_0} \tag{2.23}$$

and is called the free-space wave number. When $\boldsymbol{J}$ = 0, (2.21) and (2.22) become the homogeneous wave equations:

$$\nabla\times\Big([\,\mu_\mathrm{r}\,]^{-1}\nabla\times\boldsymbol{E}\Big) - k_0^2[\,\varepsilon_\mathrm{r}\,]\boldsymbol{E} = 0, \tag{2.24}$$

$$\nabla\times\Big([\,\varepsilon_\mathrm{r}\,]^{-1}\nabla\times\boldsymbol{H}\Big) - k_0^2[\,\mu_\mathrm{r}\,]\boldsymbol{H} = 0. \tag{2.25}$$

Here, time-average value, <S>, of the energy flow density is expressed as

$$\langle S\rangle = \frac{1}{2}\mathrm{Re}\big[\,\boldsymbol{E}\times\boldsymbol{H}^*\big], \tag{2.26}$$

where $\boldsymbol{E}\times\boldsymbol{H}^*$ is called the complex Poynting vector.

## 2.3 2-D Vector Finite Element Method for Mode Analysis

We consider an *x*-*y* plane of a 3-D optical waveguide surrounded by the perfectly matched layer (PML) regions 1-8 with thickness $d_i$ ($i$ = 1, 2, 3, 4), as shown in Fig. 2.1. By using the PML for anisotropic media [41], the relative permittivity and relative permeability tensors in the analysis region are expressed as

$$[\,\varepsilon_\mathrm{r}\,] = n^2[\,\Lambda\,], \quad [\,\mu_\mathrm{r}\,] = [\,\Lambda\,] \tag{2.27}$$

with

$$\Lambda = \begin{bmatrix} \dfrac{s_y}{s_x} & 0 & 0 \\ 0 & \dfrac{s_x}{s_y} & 0 \\ 0 & 0 & s_x s_y \end{bmatrix}, \tag{2.28}$$

where $n$ is the refractive index, and $s_x$ and $s_y$ listed in Table 2.1 are the PML parameters in the PML region. In non-PML region, $s_x$ and $s_y$, are set to 1. Here, we assume parabolic profiles of complex value of $s_i$ in Table 2.1 as

$$s_i = 1 - j\left(\frac{\rho}{d_i}\right)^2 \tan\delta_i, \tag{2.29}$$

where $\rho$ is the distance from the beginning of the PML and $\delta_i$ is the loss angle at the end of the PML ($\rho = d_i$). From Maxwell's equations, the following vectorial wave equation is derived:

$$\nabla \times ([\,p\,]\nabla \times \boldsymbol{\Phi}) - k_0^2 [\,q\,]\boldsymbol{\Phi} = 0 \tag{2.30}$$

with

$$[\,p\,] = [\,\mu_{\mathrm{r}}\,]^{-1}, \quad [\,q\,] = [\,\varepsilon_{\mathrm{r}}\,], \quad \text{for } \boldsymbol{\Phi} = \boldsymbol{E} \tag{2.31}$$

$$[\,p\,] = [\,\varepsilon_{\mathrm{r}}\,]^{-1}, \quad [\,q\,] = [\,\mu_{\mathrm{r}}\,], \quad \text{for } \boldsymbol{\Phi} = \boldsymbol{H} \tag{2.32}$$

where $k_0$, $\boldsymbol{E}$, and $\boldsymbol{H}$ are the free-space wavenumber, the electric and the magnetic fields, respectively. In the finite element analysis, solution is obtained by minimizing energy corresponding to the functional $F$ instead of solving (2.30) directly. The minimum of the functional is found by setting the derivative of the functional to zero. The functional is given as an integral form for whole analysis region, and its degree of the derived function is first order lower than that of (2.30). After multiplying left-hand side of (2.30) to $\boldsymbol{\Phi}^*$, we integrate the obtained equation over the region $\Omega$ and perform formula manipulation. Then, $F$ for (2.30) can be expressed as

$$\begin{aligned} F = &\iint_{\Omega} \left[ \left(\nabla \times \boldsymbol{\Phi}^*\right) \cdot \left(\nabla \times ([\,p\,]\nabla \times \boldsymbol{\Phi}) - k_0^2 [\,q\,]\boldsymbol{\Phi}\right) \right] dxdy \\ &+ \int_{\Gamma} \boldsymbol{\Phi}^* \cdot [\,\boldsymbol{i}_n \times ([\,p\,]\nabla \times \boldsymbol{\Phi})\,] d\Gamma = 0, \end{aligned} \tag{2.33}$$

where $^*$ and $\boldsymbol{i}_n$ denote the complex conjugate and the outward unit normal vector, respectively. We divide the analysis region into a number of higher-order edge elements [42] as shown in Fig. 2.2 and expand the transverse field components ($\Phi_x$ and $\Phi_y$), and the longitudinal field component ($\Phi_z$) in each element:

$$\boldsymbol{\Phi} = \begin{bmatrix} \Phi_x \\ \Phi_y \\ \Phi_z \end{bmatrix} = \begin{bmatrix} \{U\}^T \{\phi_t\}_e \\ \{V\}^T \{\phi_t\}_e \\ j\beta \{N\}^T \{\phi_z\}_e \end{bmatrix}, \tag{2.34}$$

where $\beta$ is the propagation constant, $T$ denotes the transpose of matrix, $\{\phi_t\}_e$ is a vector composed of all the edge variables in the hybrid edge/nodal element, and $\{\phi_z\}_e$ is a vector composed of all the nodal variables in the hybrid edge/nodal element. $\{U\}$, $\{V\}$ are the shape

function vectors for curvilinear edge element, and $\{N\}$ is the shape function vector for the curvilinear nodal element. They are given in Tables 2.2 and 2.3, where $L_1$, $L_2$, and $L_3$ are the area coordinate variables.

Substituting (2.34) into (2.33) and applying the finite element technique, the following matrix equation is obtained:

$$\begin{bmatrix} [K_{tt}] & [0] \\ [0] & [0] \end{bmatrix} - \beta^2 \begin{bmatrix} [M_{tt}] & [M_{tz}] \\ [M_{zt}] & [M_{zz}] \end{bmatrix} = \{0\} \tag{2.35}$$

with

$$\begin{aligned} [K_{tt}] = \sum\nolimits_e \iint_e \Big[ & k_0^2 q \{U\}\{U\}^T + k_0^2 q \{V\}\{V\}^t \\ & - p\{U_y\}\{U_y\}^t - p\{V_x\}\{V_x\}^t + p\{U_y\}\{V_x\}^t + p\{V_x\}\{U_y\}^t \Big] dxdy \end{aligned} \tag{2.36}$$

$$[M_{tz}] = \sum\nolimits_e \iint_e \Big[ p\{U\}\{N_x\}^T + p\{V\}\{N_y\}^T \Big] dxdy \tag{2.37}$$

$$[M_{zt}] = [M_{tz}]^t \tag{2.38}$$

$$[M_{zz}] = \sum\nolimits_e \iint_e \Big[ p\{N_x\}\{N_x\}^T + p\{N_y\}\{N_y\}^T - k_0^2 q \{N\}\{N\}^T \Big] dxdy \tag{2.39}$$

$$[M_{tt}] = \sum\nolimits_e \iint_e \Big[ p\{U\}\{U\}^T + p\{V\}\{V\}^T \Big] dxdy \tag{2.40}$$

where $\{0\}$ is a null vector, [0] is a null matrix, $\Sigma_e$ extends over all different elements, and $\{N_x\}$, $\{N_y\}$, $\{U_y\}$, and $\{V_x\}$ are given in Tables 2.4 and 2.5. As a consequence, the problem results in eigenvalue equation.

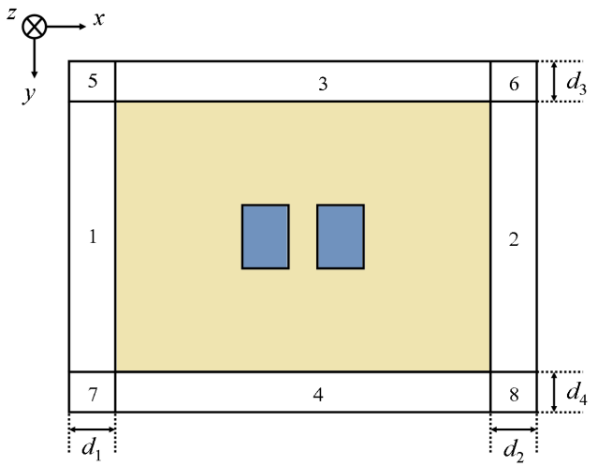


**Fig. 2.1:** Schematic of a cross section of a 3-D optical waveguide surrounded by the PML.

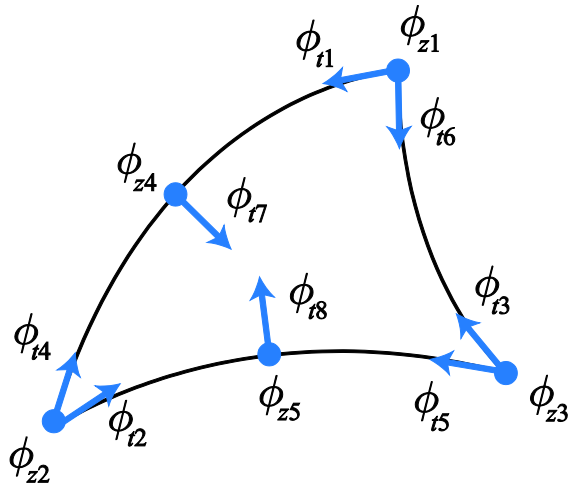


**Fig. 2.2:** Curvilinear hybrid edge/nodal element.

**Table 2.1:** Values of PML parameters in the 2-D VFEM analysis.

| PML | PML region | | | | | | | |
|---|---|---|---|---|---|---|---|---|
| Parameter | 1 | 2 | 3 | 4 | 5 | 6 | 7 | 8 |
| $s_x$ | $s_1$ | $s_2$ | 1 | 1 | $s_1$ | $s_2$ | $s_1$ | $s_2$ |
| $s_y$ | 1 | 1 | $s_3$ | $s_4$ | $s_3$ | $s_3$ | $s_4$ | $s_4$ |

**Table 2.2:** Shape function vector for nodal elements.

| | Fundamental element | Higher-order element |
|---|---|---|
| $\{N\}$ | $\begin{bmatrix} L_1 \\ L_2 \\ L_3 \end{bmatrix}$ | $\begin{bmatrix} L_1(2L_1-1) \\ L_2(2L_2-1) \\ L_3(2L_3-1) \\ 4L_1L_2 \\ 4L_2L_3 \\ 4L_3L_1 \end{bmatrix}$ |

**Table 2.3:** Shape function vector for edge elements.

| | Fundamental element | Higher-order element |
|---|---|---|
| $\{U\}$ | $\begin{bmatrix} l_1\left(L_1\frac{\partial L_2}{\partial x} - L_2\frac{\partial L_1}{\partial x}\right) \\ l_2\left(L_2\frac{\partial L_3}{\partial x} - L_3\frac{\partial L_2}{\partial x}\right) \\ l_3\left(L_3\frac{\partial L_1}{\partial x} - L_1\frac{\partial L_3}{\partial x}\right) \end{bmatrix}$ | $\begin{bmatrix} l_1L_1\frac{\partial L_2}{\partial x} \\ l_2L_2\frac{\partial L_3}{\partial x} \\ l_3L_3\frac{\partial L_1}{\partial x} \\ l_1L_2\frac{\partial L_1}{\partial x} \\ l_2L_3\frac{\partial L_2}{\partial x} \\ l_3L_1\frac{\partial L_3}{\partial x} \\ \frac{8A_e}{l_1}L_1L_2\frac{\partial L_3}{\partial x} \\ \frac{8A_e}{l_2}L_2L_3\frac{\partial L_1}{\partial x} \end{bmatrix}$ |
| $\{V\}$ | $\begin{bmatrix} l_1\left(L_1\frac{\partial L_2}{\partial y} - L_2\frac{\partial L_1}{\partial y}\right) \\ l_2\left(L_2\frac{\partial L_3}{\partial y} - L_3\frac{\partial L_2}{\partial y}\right) \\ l_3\left(L_3\frac{\partial L_1}{\partial y} - L_1\frac{\partial L_3}{\partial y}\right) \end{bmatrix}$ | $\begin{bmatrix} l_1L_1\frac{\partial L_2}{\partial y} \\ l_2L_2\frac{\partial L_3}{\partial y} \\ l_3L_3\frac{\partial L_1}{\partial y} \\ l_1L_2\frac{\partial L_1}{\partial y} \\ l_2L_3\frac{\partial L_2}{\partial y} \\ l_3L_1\frac{\partial L_3}{\partial y} \\ \frac{8A_e}{l_1}L_1L_2\frac{\partial L_3}{\partial y} \\ \frac{8A_e}{l_2}L_2L_3\frac{\partial L_1}{\partial y} \end{bmatrix}$ |

**Table 2.4:** Differentiation of Shape function vector for nodal elements.

| | Fundamental element | Higher-order element |
|---|---|---|
| $\{N_x\}$ | $\begin{bmatrix} \frac{\partial L_1}{\partial x} \\ \frac{\partial L_2}{\partial x} \\ \frac{\partial L_3}{\partial x} \end{bmatrix}$ | $\begin{bmatrix} \frac{\partial L_1}{\partial x}(4L_1-1) \\ \frac{\partial L_2}{\partial x}(4L_2-1) \\ \frac{\partial L_3}{\partial x}(4L_3-1) \\ 4\left(L_2\frac{\partial L_1}{\partial x}L_1\frac{\partial L_2}{\partial x}\right) \\ 4\left(L_3\frac{\partial L_2}{\partial x}L_2\frac{\partial L_3}{\partial x}\right) \\ 4\left(L_1\frac{\partial L_3}{\partial x}L_3\frac{\partial L_1}{\partial x}\right) \end{bmatrix}$ |
| $\{N_y\}$ | $\begin{bmatrix} \frac{\partial L_1}{\partial y} \\ \frac{\partial L_2}{\partial y} \\ \frac{\partial L_3}{\partial y} \end{bmatrix}$ | $\begin{bmatrix} \frac{\partial L_1}{\partial y}(4L_1-1) \\ \frac{\partial L_2}{\partial y}(4L_2-1) \\ \frac{\partial L_3}{\partial y}(4L_3-1) \\ 4\left(L_2\frac{\partial L_1}{\partial y}L_1\frac{\partial L_2}{\partial y}\right) \\ 4\left(L_3\frac{\partial L_2}{\partial y}L_2\frac{\partial L_3}{\partial y}\right) \\ 4\left(L_1\frac{\partial L_3}{\partial y}L_3\frac{\partial L_1}{\partial y}\right) \end{bmatrix}$ |

**Table 2.5:** Differentiation of Shape function vector for edge elements.

| | Fundamental element | Higher-order element |
|---|---|---|
| $\{U_y\}$ | $\begin{bmatrix} l_1\left(\frac{\partial L_2}{\partial x}\frac{\partial L_1}{\partial y}-\frac{\partial L_1}{\partial x}\frac{\partial L_2}{\partial y}\right) \\ l_2\left(\frac{\partial L_3}{\partial x}\frac{\partial L_2}{\partial y}-\frac{\partial L_2}{\partial x}\frac{\partial L_3}{\partial y}\right) \\ l_3\left(\frac{\partial L_1}{\partial x}\frac{\partial L_3}{\partial y}-\frac{\partial L_3}{\partial x}\frac{\partial L_1}{\partial y}\right) \end{bmatrix}$ | $\begin{bmatrix} l_1\frac{\partial L_2}{\partial x}\frac{\partial L_1}{\partial y} \\ l_2\frac{\partial L_3}{\partial x}\frac{\partial L_2}{\partial y} \\ l_3\frac{\partial L_1}{\partial x}\frac{\partial L_3}{\partial y} \\ l_1\frac{\partial L_1}{\partial x}\frac{\partial L_2}{\partial y} \\ l_2\frac{\partial L_2}{\partial x}\frac{\partial L_3}{\partial y} \\ l_3\frac{\partial L_3}{\partial x}\frac{\partial L_1}{\partial y} \\ \frac{8A_e}{l_1}\frac{\partial L_3}{\partial x}\left(L_2\frac{\partial L_1}{\partial y}L_1\frac{\partial L_2}{\partial y}\right) \\ \frac{8A_e}{l_2}\frac{\partial L_1}{\partial x}\left(L_3\frac{\partial L_2}{\partial y}L_2\frac{\partial L_3}{\partial y}\right) \end{bmatrix}$ |
| $\{V_x\}$ | $\begin{bmatrix} l_1\left(\frac{\partial L_1}{\partial x}\frac{\partial L_2}{\partial y}-\frac{\partial L_2}{\partial x}\frac{\partial L_1}{\partial y}\right) \\ l_2\left(\frac{\partial L_2}{\partial x}\frac{\partial L_3}{\partial y}-\frac{\partial L_3}{\partial x}\frac{\partial L_2}{\partial y}\right) \\ l_3\left(\frac{\partial L_3}{\partial x}\frac{\partial L_1}{\partial y}-\frac{\partial L_1}{\partial x}\frac{\partial L_3}{\partial y}\right) \end{bmatrix}$ | $\begin{bmatrix} l_1\frac{\partial L_1}{\partial x}\frac{\partial L_2}{\partial y} \\ l_2\frac{\partial L_2}{\partial x}\frac{\partial L_3}{\partial y} \\ l_3\frac{\partial L_3}{\partial x}\frac{\partial L_1}{\partial y} \\ l_1\frac{\partial L_2}{\partial x}\frac{\partial L_1}{\partial y} \\ l_2\frac{\partial L_3}{\partial x}\frac{\partial L_2}{\partial y} \\ l_3\frac{\partial L_1}{\partial x}\frac{\partial L_3}{\partial y} \\ \frac{8A_e}{l_1}\frac{\partial L_3}{\partial y}\left(L_2\frac{\partial L_1}{\partial x}L_1\frac{\partial L_2}{\partial x}\right) \\ \frac{8A_e}{l_2}\frac{\partial L_1}{\partial y}\left(L_3\frac{\partial L_2}{\partial x}L_2\frac{\partial L_3}{\partial x}\right) \end{bmatrix}$ |

## 2.4 2-D Finite Element Method for Waveguide Discontinuity Problem

We consider a 2-D optical waveguide discontinuity problem, as shown in Fig. 2.3. Surrounding the analysis region $\Omega$ by the anisotropic PML [41], the relative permittivity and relative permeability tensors in the analysis region are expressed as

$$[\varepsilon_{\mathrm{r}}] = n^2[\Lambda], \quad [\mu_{\mathrm{r}}] = [\Lambda] \tag{2.41}$$

with

$$\Lambda = \begin{bmatrix} s_y s_z & 0 & 0 \\ 0 & \dfrac{s_z}{s_y} & 0 \\ 0 & 0 & \dfrac{s_y}{s_z} \end{bmatrix}, \tag{2.42}$$

where $n$ is the refractive index, and $s_y$ and $s_z$ listed in Table 2.6 are the PML parameters in the PML region. In non-PML region, $s_y$ and $s_z$ are set to 1. Here, we assume parabolic profiles of complex value of $s_i$ in Table 2.6 as

$$s_i = 1 - j\left(\frac{\rho}{d_i}\right)^2 \tan\delta_i, \tag{2.43}$$

where $\rho$ is the distance from the beginning of the PML and $\delta_i$ is the loss angle at the end of the PML ($\rho = d_i$). From Maxwell's equations, the following basic equation is derived:

$$\frac{\partial}{\partial y}\left(p\frac{s_z}{s_y}\frac{\partial\Phi}{\partial y}\right) + \frac{\partial}{\partial z}\left(p\frac{s_y}{s_z}\frac{\partial\Phi}{\partial z}\right) + k_0^2 s_y s_z q\Phi = 0 \tag{2.44}$$

$$\Phi = E_x, \quad p = 1, \quad q = n^2 \quad \text{for TE mode} \tag{2.45}$$

$$\Phi = H_x, \quad p = \frac{1}{n^2}, \quad q = 1 \quad \text{for TM mode} \tag{2.46}$$

where $k_0$, $E_x$, and $H_x$ are the free-space wavenumber and the $x$ components of the electric and magnetic fields, respectively.

Dividing the analysis region into quadratic triangular elements, the fields $\Phi$ within each element can be approximated as

$$\Phi = [N]^T \{\phi\}_e, \tag{2.47}$$

where $\{N\}$ and $\{\phi\}_e$ are the shape function vector for the quadratic triangular element and the nodal $\phi$ vector for each element.

Here, we consider the incidence plane $\Gamma$ as shown in Fig. 2.3 and divide the region $\Omega$ into two subregions, $\Omega_1$ and $\Omega_2$. Applying the Galerkin procedure to (2.44), the element equation is obtained. Next, we assemble the complete matrix for $\Omega$ by adding the contributions of all the different elements. Then, the boundary integral terms vanish except for the incidence plane $\Gamma$,

owing to the continuity conditions of the electric and magnetic fields, and we obtain the following matrix equation:

$$[p]\{\phi\} = \sum\nolimits_e^{'} \int_e p \frac{s_y}{s_z} \{N\}_\Gamma \left( \frac{\partial \phi_1}{\partial z} - \frac{\partial \phi_2}{\partial z} \right) d\Gamma \tag{2.48}$$

with

$$[p] = \sum\nolimits_e^{'} \int_e \left[ p \frac{s_z}{s_y} \frac{\partial \{N\}}{\partial y} \frac{\partial \{N\}^T}{\partial y} + p \frac{s_y}{s_z} \frac{\partial \{N\}}{\partial z} \frac{\partial \{N\}^T}{\partial z} - k_0^2 q s_y s_z \{N\}\{N\}^T \right] dydz\,, \tag{2.49}$$

where the components of vector $\{\phi\}$ are the values of $\phi$ at all nodal points in $\Omega$, $\Sigma_e$ extends over all elements, and $\Sigma_e^{'}$ extends over the elements related to $\Gamma$. The field $\phi$ in the region $\Omega_i$ ($i$ =1, 2) is expressed as $\phi_i$. We define the incident field as $\phi_{\text{in}}$ and the scattering field as $\phi_{\text{scat}}$. Then, the field in $\Omega_i$ is expressed as

$$\phi_i = \phi_{\text{in},i} + \phi_{\text{scat},i} \tag{2.50}$$

and the continuity condition of the electric and magnetic fields on the incident plane $\Gamma$ is given by

$$\frac{\partial \phi_{\text{scat},1}}{\partial z} = \frac{\partial \phi_{\text{scat},2}}{\partial z}\,. \tag{2.51}$$

Then, (2.48) is rewritten as

$$[P]\{\phi\} = \sum\nolimits_e^{'} \int_e p \frac{s_y}{s_z} \{N\}_\Gamma \left( \frac{\partial \phi_{\text{in},1}}{\partial z} - \frac{\partial \phi_{\text{in},2}}{\partial z} \right) d\Gamma\,. \tag{2.52}$$

If we can express the arbitrary incident fields $\phi_{\text{in},1}$ and $\phi_{\text{in},2}$ using the eigen modes as

$$\phi_{\text{in},1} = \sum_m A_m f_m(y) \exp(-j\beta_m z)\,, \tag{2.53}$$

$$\phi_{\text{in},2} = \sum_m A_m f_m(y) \exp(j\beta_m z)\,. \tag{2.54}$$

Then (2.52) becomes

$$[P]\{\phi\} = [Q]\{\Psi\}_\Gamma \tag{2.55}$$

with

$$[Q] = \sum\nolimits_e^{'} \int_e p \frac{s_y}{s_z} \{N\}_\Gamma \{N\}_\Gamma^T dy \tag{2.56}$$

$$\{\Psi\}_\Gamma = -2 \sum_m j\beta_m A_m \{f_m\}_\Gamma\,, \tag{2.57}$$

where $A_m$, $f_m(y)$, $\beta_m$ are the amplitude, modal field function, and propagation constant of $m$-th mode, respectively. $\{N\}_\Gamma$ and $\{f_m\}_\Gamma$ are the shape function vector and the field vector of $f_m(y)$ on the incidence plane $\Gamma$, respectively. When defining the vector composed of the values of $\phi$ at nodal points on the incidence plane $\Gamma$ as $\{\phi\}_\Gamma$ and the vector related to the remaining nodes as $\{\phi\}_0$, (2.55) can be written as

$$\begin{bmatrix} [p]_{00} & [p]_{0\Gamma} \\ [p]_{\Gamma 0} & [p]_{\Gamma\Gamma} \end{bmatrix} \begin{bmatrix} \{\phi\}_0 \\ \{\phi\}_\Gamma \end{bmatrix} = \begin{bmatrix} \{0\} \\ [Q]\{\Psi\}_\Gamma \end{bmatrix}, \tag{2.58}$$

where $[P]_{00}$, $[P]_{0\Gamma}$, $[P]_{\Gamma 0}$, and $[P]_{\Gamma\Gamma}$ are the partial matrices of $[P]$.

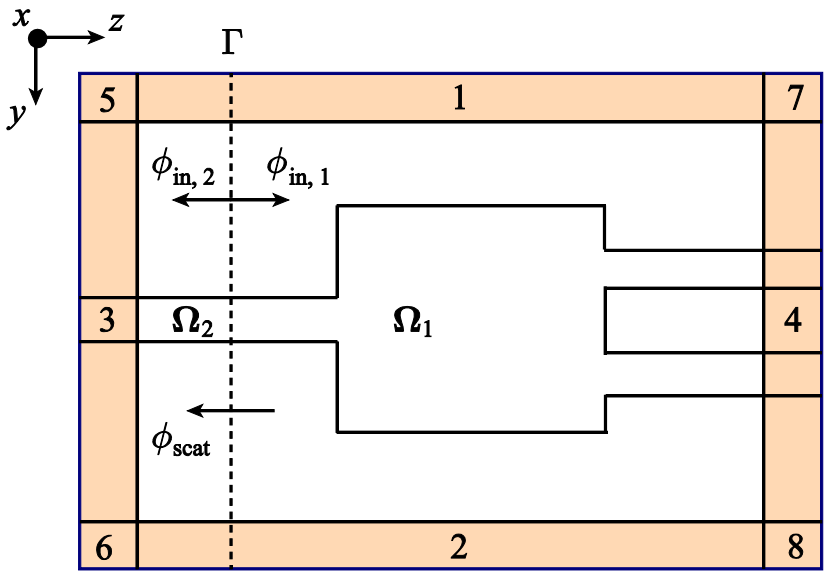


**Fig. 2.3:** Schematic of a 2-D optical waveguide surrounded by the PML.

**Table 2.6:** Values of PML parameters in the 2-D FEM for the discontinuity problem.

| PML | PML region | | | | | | | |
|---|---|---|---|---|---|---|---|---|
| parameter | 1 | 2 | 3 | 4 | 5 | 6 | 7 | 8 |
| $s_y$ | $s_1$ | $s_2$ | 1 | 1 | $s_1$ | $s_2$ | $s_1$ | $s_2$ |
| $s_z$ | 1 | 1 | $s_3$ | $s_4$ | $s_3$ | $s_3$ | $s_4$ | $s_4$ |

# Chapter 3

# Optical Logic Gates for BPSK Signals

## 3.1 Introduction

Optical logic gates [4-15, 43, 44] have attracted increasing attention due to their practical utility in networks and systems, such as optical label swapping and recognition for optical packet switching schemes [1, 2]. Optical logic gates are applied to label swapping architectures [3] and optical packet time-to-live processors [45]. Optical packet switching systems have some advantages, such as high throughputs, low power consumption, and high band efficiency, compared to conventional electrical routers.

However, different modulation formats will be selectively used according to different network scales and applications in future networks [46, 47]. For example, on-off-keyed (OOK) modulation formats and binary-phase-shift-keyed (BPSK) modulation formats are expected to be simultaneously used in networks. This is because the OOK formats are cost-effective for access area networks and metropolitan area networks, whereas the BPSK formats improve receiver sensitivity and enhance tolerance to fiber nonlinearity in long-haul transmission systems [48-50]. Differential-phase-shift-keyed (DPSK) receivers have been studied for many years [51], and the use of the delay-interferometer with direct detection has been extensively studied [52, 53]. Compared to the OOK formats, the DPSK formats have the advantage of a 3-dB reduction in the required optical signal-to-noise ratio (OSNR) [52, 53]. To process the DPSK signal, optical logic gates for the DPSK signal using semiconductor optical amplifiers [16, 17] or periodically poled lithium niobate [18] have been reported. Recently, for further efficiency upgrades of transmission, coherent detection has again become a topic of interest [54-56] due to the advantage of OSNR [54] and the availability of ultra-dense wavelength division multiplexing [57] compared to direct detection. However, to our knowledge, optical logic gates with coherent detection have not been reported.

Here, we consider the optical packet switching system for OOK modulation formats as shown in Fig. 3.1(a). Because most of the reported optical logic gates are operated by employing optical intensity on logical value [4-15], these logic gates can be directly utilized for components of the label recognition as arithmetic processing devices for OOK signals. Next, we consider the optical packet switching system for BPSK modulation formats as shown in Fig. 3.1(b). In this system, some sort of phase-to-amplitude converter is required to use conventional optical logic gates that employ optical intensity as bit information [4-15]. However, this situation makes the label recognition architectures complicated.

To avoid cumbersome architectures, in this chapter, we propose optical XOR, XNOR, NAND, and OR logic gates with coherent detection based on multi-mode interference (MMI) waveguides for BPSK signals. The optical logic gates include functions as phase-to-amplitude converters and operate as logic gates, as shown in Fig. 3.1(c). In the optical logic gates, the logical value of the input is determined by the phase information, whereas the logical value of the output is determined by the amplitude. Moreover, we adopt silicon-based MMI waveguides for the base structure of the logic gates because MMI-based devices have several advantages, including their simple configuration, large bandwidth, and compact size [58-60]. We employ the finite element method (FEM) [40] for numerical simulations and calculate the spectrum of the ON to OFF logic-level contrast ratio.

## 3.2 MMI Theory

MMI devices are based on the self-imaging property, in which the guided modes of a MMI region are excited and interfere constructively when a smaller input field of input waveguide is launched. Then, the excited fields in the MMI region transmute periodically along the propagation direction. Here, the beat length $L_\pi$ in the MMI region is given by

$$L_\pi = \frac{\pi}{\beta_0 - \beta_1} = \frac{\lambda}{2(n_{\mathrm{eff0}} - n_{\mathrm{eff1}})}, \tag{3.1}$$

where $\beta_0$ and $\beta_1$ indicate the propagation constant of the fundamental mode and first-order mode, respectively, $n_{\mathrm{eff0}}$ and $n_{\mathrm{eff1}}$ represent the effective refractive indices of the fundamental mode and first-order mode, respectively, and $\lambda$ is the wavelength. From the MMI theory [61], (3.1) is rewritten as follows:

$$L_\pi \cong \frac{4 n_{\mathrm{c}} W_{\mathrm{eff}}^2}{3\lambda}, \tag{3.2}$$

where $n_{\mathrm{c}}$ and $W_{\mathrm{eff}}$ are the refractive index and effective width of the MMI region, respectively. In the two-input waveguide case, there are two self-imaging mechanisms. One is the general interference (GI). In this case, the distance of first $N$-fold images $L$ is defined as

$$L = \frac{3L_\pi}{N}, \tag{3.3}$$

where $N \geqq 1$ is integer. The other mechanism is the restricted interference (RI). In this case, $L$ is defined as

$$L = \frac{L_\pi}{N} . \tag{3.4}$$

From (3.3) and (3.4), it can be seen that the coupling length of the RI mechanism is three times shorter than that of the GI mechanism.

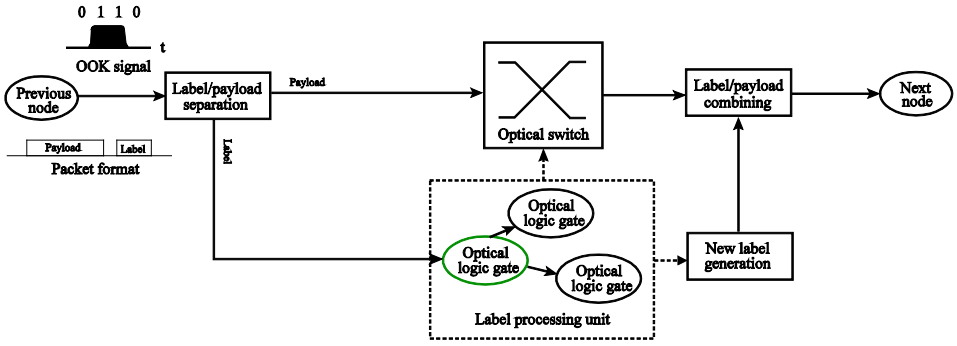


(a)

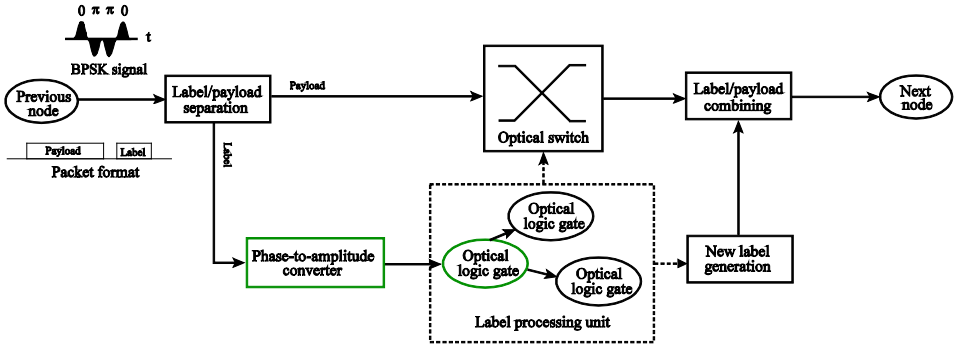


(b)

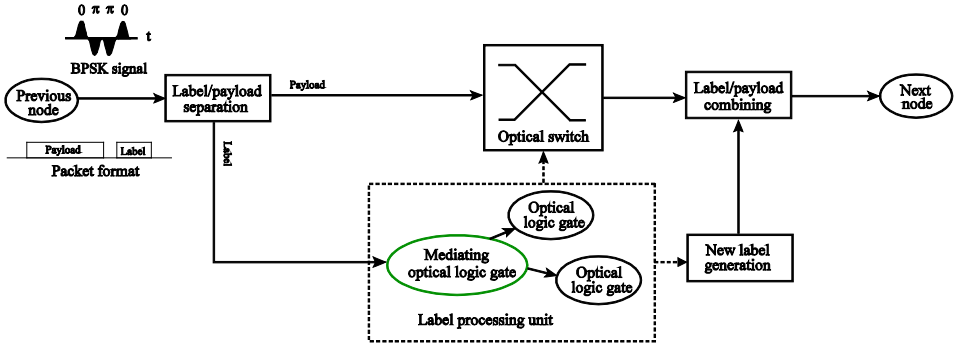


(c)

**Fig. 3.1:** General constitution of an optical packet switching system. (a) Label processing scheme for OOK signals. (b) Label processing scheme for BPSK signals with phase-to-amplitude converter. (c) Label processing scheme for BPSK signals with an optical logic gate that employs the phase of input-light as bit information.

## 3.3 Optical Logic Gates with Phase-Locked Loop

### 3.3.1 Structure Description

Fig. 3.2(a) shows a schematic of optical XOR, XNOR, NAND and OR logic gates. The logic gates are composed of three MMI waveguides-based 3-dB couplers. Ports B and C are input ports corresponding to logical input, and port F is output port to obtain logical output. In addition, ports A and D are input ports to input the local oscillator (LO) light. Ports E and H are ports for coherent detection, and port G is an idle port. In coherent detection, the LO laser and photodetector (PD) are required to construct an optical phase-locked loop (PLL) with a single blanch whose role is tracking the phase of the BPSK signal [55, 62, 63]. Fig. 3.2(b) shows the structure of the MMI-based 3-dB coupler. To shorten the length of device, we employ the restricted self-imaging effect. Under the RI condition, the input/output waveguide of the MMI-based 3-dB coupler should be placed at a lateral offset $\pm W_{MMI}/6$ with respect to the center of the MMI region [61]. We assume that the materials of the core and cladding are Si with a refractive index of 3.5 and $SiO_2$ with a refractive index of 1.45, respectively. The width and length of the MMI region are defined as $W_{MMI}$ and $L_{MMI}$, respectively, and the width of input/output waveguide $w$ is 0.3 μm. Moreover, a taper is introduced between the input/output waveguide and MMI region to improve the transmission characteristics [60]. We set the width and length of the taper as $W_{taper}$ = 0.9 μm and $L_{taper}$ = 1.5 μm, respectively.

Fig. 3.3 shows the normalized power variation when changing the $L_{MMI}$ from 12.5 μm to 14.0 μm. Here, we describe how to design $W_{MMI}$ and $L_{MMI}$ of the MMI-based 3-dB coupler using the results shown in Fig. 3.3. From (3.2), it is obvious that as the width of the MMI region is wider, the length of the MMI region becomes longer. Accordingly, we select $W_{MMI}$ = 3.0 μm so that the total size of the device is as small as possible. When setting $W_{MMI}$ = 3.0 μm, and assuming $W_{eff} = W_{MMI}$, from (3.2) and (3.4), we can see that $L$ becomes 13.5 μm at $\lambda$ = 1.55 μm (first 2-fold images). Next, we calculate the distance of first 2-fold images from (3.1). By using the mode-analysis-FEM solver, $n_{eff0}$ = 3.49 and $n_{eff1}$ = 3.46 for the TM mode are obtained. As a result, $L$ becomes 13.7 μm at $\lambda$ = 1.55 μm from (3.4). This result is in excellent agreement with that from (3.2).

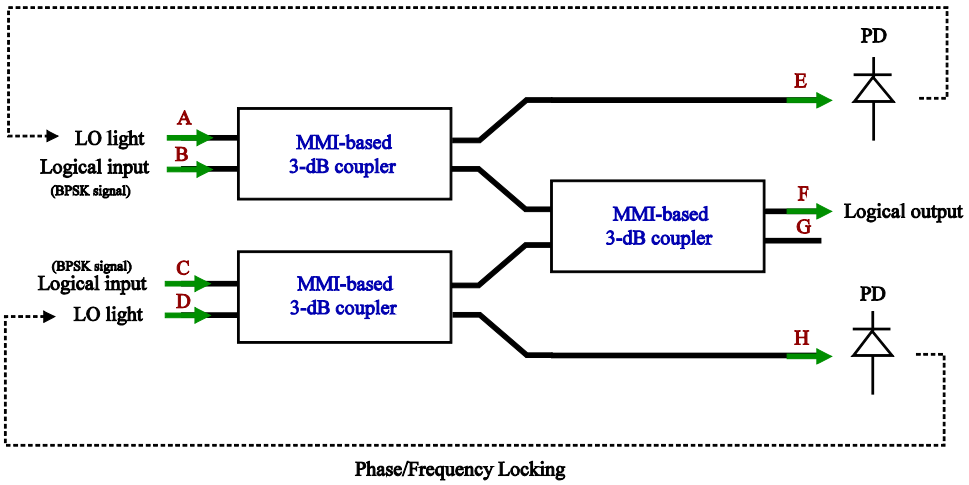


(a)

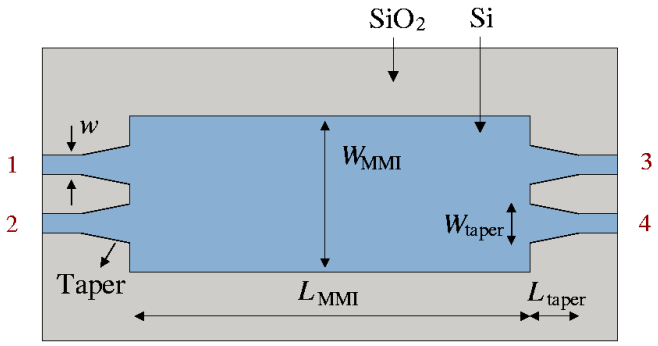


(b)

**Fig. 3.2:** (a) Schematic of optical XOR, XNOR, NAND and OR logic gates. (b) Structure of the MMI-based 3-dB coupler.

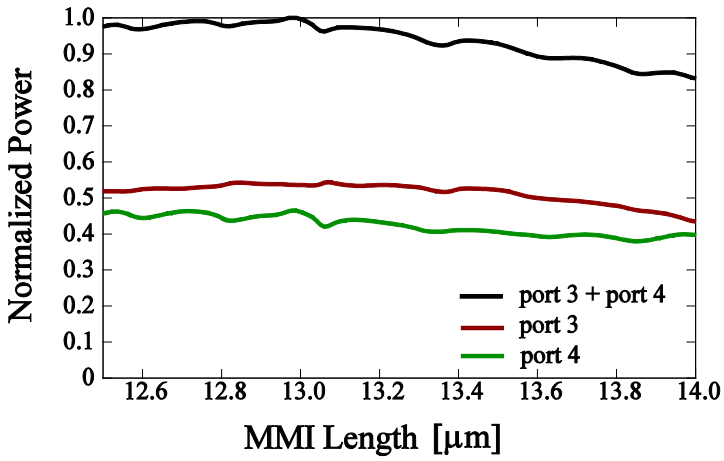


**Fig. 3.3:** Normalized power variation when changing the $L_{MMI}$ from 12.5 μm to 14.0 μm.

### 3.3.2 Operation Principle of MMI-Based 3-dB Couplers

To explain the operation principle of the MMI-based 3-dB coupler, at first, we consider that a beam is inputted into port 1. Because the 3-dB coupler is treated, the power is equally divided between port 3 and port 4. Then, the phase difference between port 3 and port 4 is consistently "$\pi/2$". Under this condition, we assume that the phase on port 3 and port 4 are, respectively, $\pi/2$ and 0, as shown in Fig. 3.4(a) (State 1). If a beam having the same phase for State 1 is inputted into port 2, the phase in port 3 and port 4 become 0 and $\pi/2$, respectively, as shown in Fig. 3.4(b) (State 2).

Next, we consider the case in which beams are inputted with the same phase into both port 1 and port 2. Because our proposed structure is a linear device, the structure satisfies the principle of superposition. Thus, it is able to add the complex amplitude of State 1 and State 2, and the lights on port 3 and port 4 have the same phase and amplitude, as shown in Fig. 3.4(c). We consider the condition that there exists a certain phase difference between port 1 and port 2. If the phase difference is $+\pi/2$ (the phase at port 2 is faster than that of port 1), the phase lead of outputted lights is $\pi/2$ compared to the output phase relation of State 1. In this case, the light on port 4 are negated due to the opposite phase, and consequently, the light is outputted from only port 3, as shown in Fig. 3.4(d). On the other hand, if the phase difference is $-\pi/2$ (the phase at port 2 is slower than that of port 1), the phase lag of outputted lights is $\pi/2$ compared to the output phase relation of State 1. Then, the light on port 3 is negated due to the opposite phase, and consequently, the light is outputted from only port 4, as shown in Fig. 3.4(e). We apply these physical phenomena to the basic operating principle of the logic gates. Thus, the MMI-based 3-dB coupler fulfills the role of converter that converts the phase information of the input signal to amplitude at the output.

In practice, there is a phase error between the BPSK signal and the LO light. Therefore, the conversion efficiency when there is the phase error becomes an important indicator for practical implementation. Fig. 3.5 shows the conversion efficiency spectra of the MMI-based 3-dB coupler as a function of the phase difference ($\Delta\Phi$) between port 1 and port 2. The conversion efficiency $\eta$ is defined as

$$\eta = \frac{P_{\text{port3}}}{P_{\text{max}}} \times 100 \tag{3.5}$$

where, $P_{\text{max}}$ and $P_{\text{port3}}$ are, respectively, the maximum output power and the power of port 3. Moreover, we show the insertion loss of the MMI-based 3-dB coupler. Fig. 3.6 shows the wavelength dependence of the insertion loss in the whole C-band. The insertion loss $IL$ is defined as

$$IL = 10\log_{10}\frac{P_{\text{port3}} + P_{\text{port4}}}{P_{\text{port1}}} \tag{3.6}$$

where $P_{\text{port1}}$ and $P_{\text{port3}} + P_{\text{port4}}$ are, respectively, the normalized input power and the total output power. The largest insertion loss is $-0.14$ dB in the whole C-band. The cause of the

loss is radiation and reflection around the connections between the MMI region and the input/output waveguides.

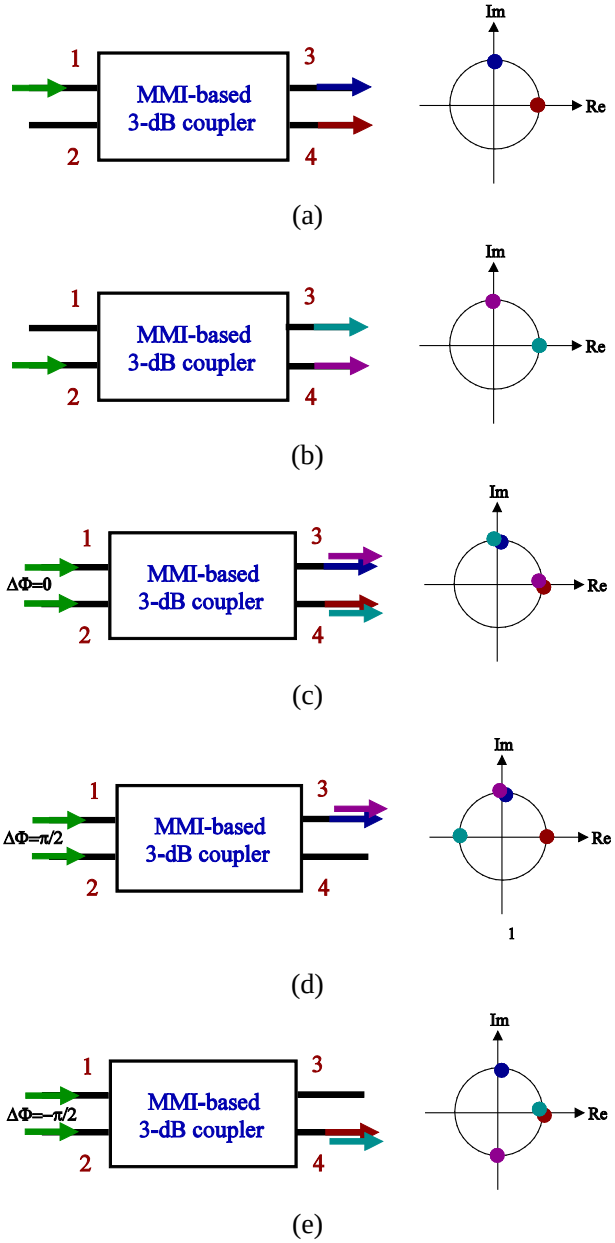


**Fig. 3.4:** Operation principle of the MMI-based 3-dB coupler. $\Delta\Phi$ is the phase difference between port 1 and port 2. The color of the arrow corresponds to the dot on the complex plane.

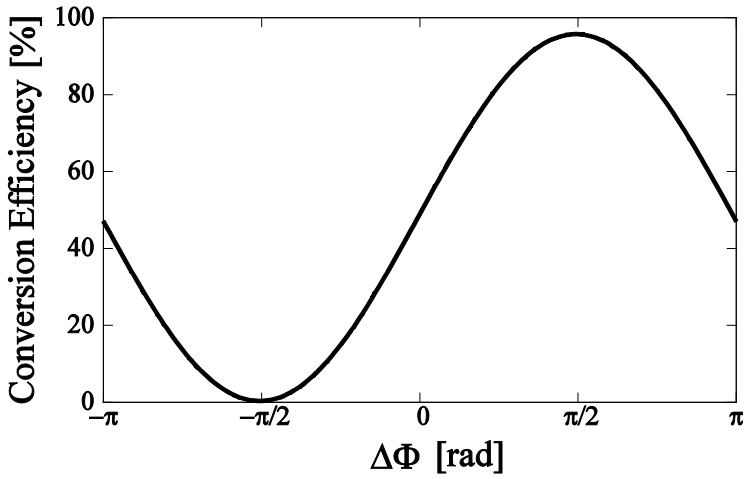


**Fig. 3.5:** The conversion efficiency as a function of the phase difference at $\lambda$ = 1.55 μm operating wavelength. $\Delta\Phi$ is the phase difference between port 1 and port 2.

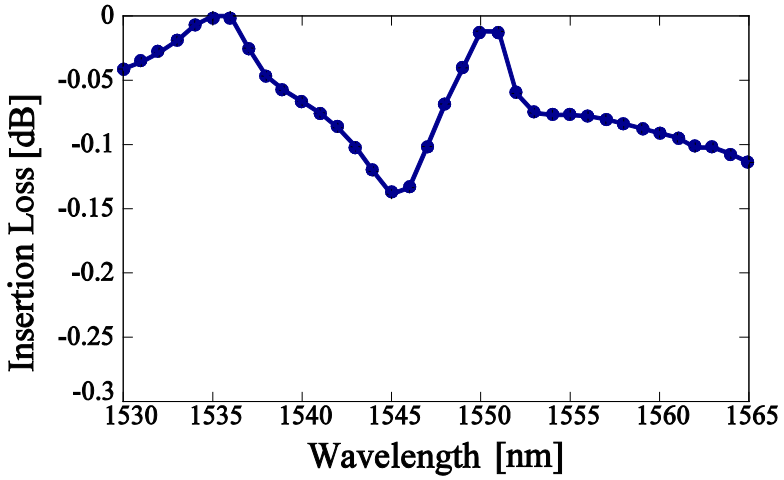


**Fig. 3.6:** The spectrum of the insertion loss.

### 3.3.3 XOR Logic Gate

To realize a XOR logic gate, we assume the ideal conditions that the phases of the LO light on ports A and D are $\pi/2$ and 0, respectively. Moreover, we assume the same wavelength and polarization between the input-signal light and the LO light. In the BPSK format, 0-phase corresponds to logic 0, while $\pi$-phase corresponds to logic 1. Here, we assume that a $-\pi/2$ phase sifter is inserted in front of port C to realize a XOR logic gate. In this way, on port C, $\pi/2$-phase corresponds to logic 1, whereas $-\pi/2$-phase corresponds to logic 0. If these requirements have been satisfied, the XOR logic gate operates as follows:

i) When an input-beam on port B has a phase $\varphi = 0$ (corresponding to logic 0) and an input-beam on port C has $\varphi = -\pi/2$ (corresponding to logic 0), logic 0 is obtained from port F.

ii) When an input-beam on port B has $\varphi = 0$ (corresponding to logic 0) and an input-beam on port C has $\varphi = \pi/2$ (corresponding to logic 1), logic 1 is obtained from port F.

iii) When an input-beam on port B has phase $\varphi = \pi$ (corresponding to logic 1) and an input-beam on port C has $\varphi = -\pi/2$ (corresponding to logic 0), logic 1 is obtained from port F.

iv) When an input-beam on port B has $\varphi = \pi$ (corresponding to logic 1) and an input-beam on port C has $\varphi = \pi/2$ (corresponding to logic 1), logic 0 is obtained from port F. These operations are summarized in Table 3.1.

To gain further insight into the physics of the XOR logic gate, the field distributions at $\lambda$ = 1.55 μm are illustrated in Fig. 3.7, from which it is recognized that the structure functions as an XOR gate. To show the effectiveness of XOR operation, we calculate the spectrum of the ON to OFF logic-level contrast ratio on port F. We need to evaluate the contrast ratio by taking the worst combination of the logic 1 and logic 0 states because there are two identical logical output states of logic 0 or logic 1. Therefore, we select XOR operation of (i) as logic 0 state and (iii) as logic 1 state in the calculation of the contrast ratio. The contrast ratio *CR* is defined as

$$CR = 10\log_{10}\frac{P_1}{P_0} \tag{3.7}$$

where $P_0$ and $P_1$ are the output powers for obtaining logic 0 and logic 1, respectively. Fig. 3.8 shows the spectrum of the *CR* of the XOR logic gate. It is found that the smallest ON to OFF logic-level contrast ratio for the XOR logic gate is 21.5 dB in the whole C-band.

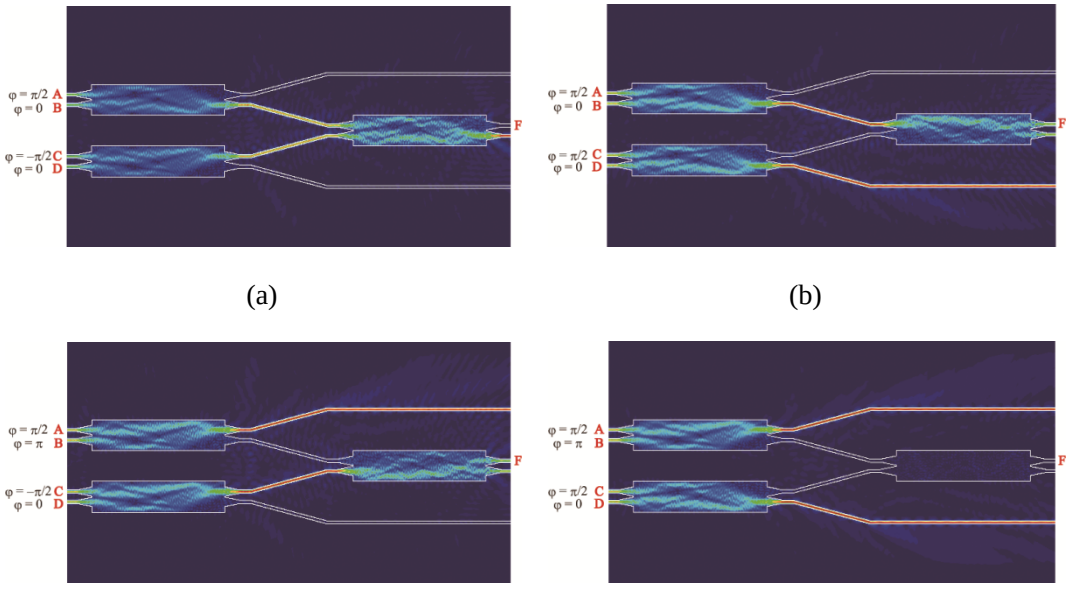


**Fig. 3.7:** Field distributions of the XOR logic gate at an operating wavelength of $\lambda$ = 1.55 μm. (a)-(d) correspond to explanations of the XOR operation (i)-(iv), respectively.

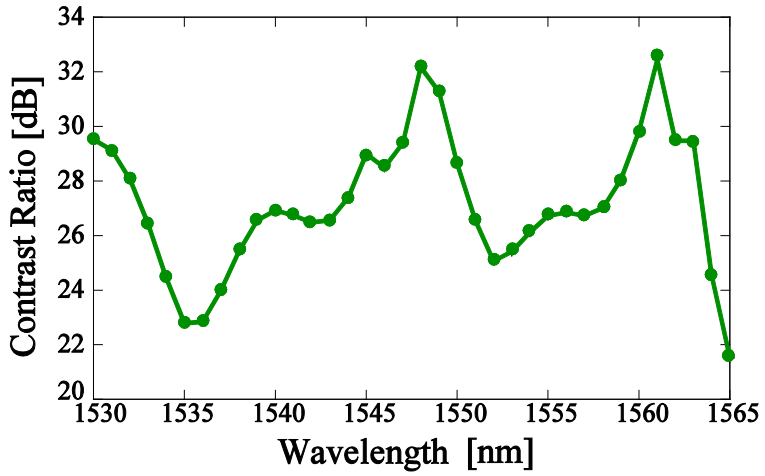


**Fig. 3.8:** The spectrum of the ON to OFF logic-level contrast ratio for the XOR logic gate.

**Table 3.1:** Functions of the XOR logic gate.

| Logical inputs | | | | Logical output |
|---|---|---|---|---|
| B | | C | | F |
| **logic** | $\varphi$ | **logic** | $\varphi$ | **Logic** |
| **0** | 0 | **0** | $-\pi/2$ | **0** |
| **0** | 0 | **1** | $\pi/2$ | **1** |
| **1** | $\pi$ | **0** | $-\pi/2$ | **1** |
| **1** | $\pi$ | **1** | $\pi/2$ | **0** |

### 3.3.4 XNOR Logic Gate

To realize an XNOR logic gate, we assume the ideal conditions that the phases of the LO light on ports A and D are $\pi/2$ and 0, respectively. Moreover, we suppose the same wavelength and polarization between the input-signal light and the LO light. In the BPSK format, the 0-phase corresponds to logic 0, whereas the $\pi$-phase corresponds to logic 1. Here, we assume that a $\pi/2$ phase sifter is inserted in front of port C to realize an XNOR logic gate. In this way, on port C, $\pi/2$-phase corresponds to logic 0, whereas $-\pi/2$-phase corresponds to logic 1. If these requirements have been satisfied, the XNOR logic gate operates as follows:

i) When an input-beam on port B has a phase $\varphi = 0$ (corresponding to logic 0) and an input-beam on port C has $\varphi = \pi/2$ (corresponding to logic 0), logic 1 is obtained from port F.

ii) When an input-beam on port B has $\varphi = 0$ (corresponding to logic 0) and an input-beam on port C has $\varphi = -\pi/2$ (corresponding to logic 1), logic 0 is obtained from port F.

iii) When an input-beam on port B has a phase $\varphi = \pi$ (corresponding to logic 1) and an input-beam on port C has $\varphi$
$= \pi/2$ (corresponding to logic 0), logic 0 is obtained from port F.

iv) When an input-beam on port B has $\varphi = \pi$ (corresponding to logic 1) and an input-beam on port C has $\varphi = -\pi/2$ (corresponding to logic 1), logic 1 is obtained from port F. These operations are summarized in Table 3.2. To gain more insight into the physics of the XNOR logic gate, the field distributions at $\lambda = 1.55\,\mu$m are illustrated in Fig. 3.9, from which it is recognized that the structure functions as an XNOR gate. For the XNOR logic gate, the smallest ON to OFF logic-level contrast ratio is 21.5 dB. We should note that this result is the same as the case of the XOR logic gate because the differences in operation between the XOR case and the XNOR case are the phase relation on port C.

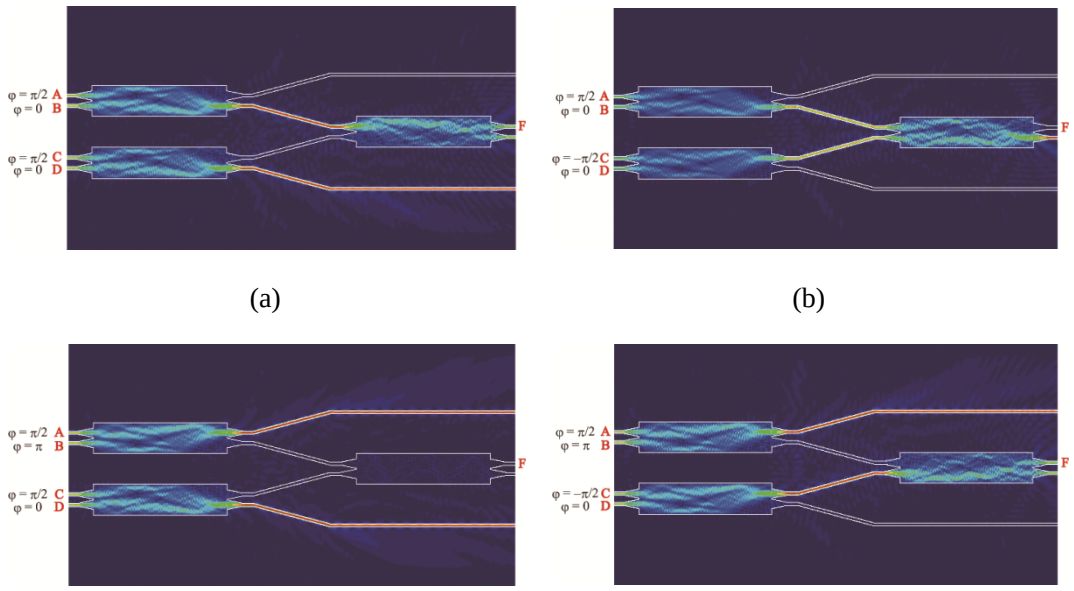


**Fig. 3.9:** Field distributions of the XNOR logic gate at an operating wavelength of $\lambda$ = 1.55 μm. (a)-(d) correspond to explanations of the XNOR operation (i)-(iv), respectively.

**Table 3.2:** Functions of the XNOR logic gate.

| Logical inputs | | | | Logical output |
|---|---|---|---|---|
| B | | C | | F |
| **logic** | $\varphi$ | **logic** | $\varphi$ | **Logic** |
| **0** | 0 | **0** | $\pi/2$ | **1** |
| **0** | 0 | **1** | $-\pi/2$ | **0** |
| **1** | $\pi$ | **0** | $\pi/2$ | **0** |
| **1** | $\pi$ | **1** | $-\pi/2$ | **1** |

### 3.3.5 NAND Logic Gate

To realize a NAND logic gate, we assume the ideal conditions that the phase of the LO light on ports A and D is $\pi/2$ when the phase of the BPSK signal is 0 or $\pi$. Moreover, we assume the same wavelength and polarization between the input-signal light and the LO light. If these requirements have been satisfied, the NAND logic gate operates as follows:

i) When an input-beam on port B has $\varphi = 0$ (corresponding to logic 0) and an input-beam on port C has $\varphi = 0$ (corresponding to logic 0), logic 1 is obtained from port F.

ii) When an input-beam on port B has $\varphi = 0$ (corresponding to logic 0) and an input-beam on port C has $\varphi = \pi$ (corresponding to logic 1), logic 1 is obtained from port F.

iii) When an input-beam on port B has a phase $\varphi = \pi$ (corresponding to logic 1) and an input-beam on port C has $\varphi = 0$ (corresponding to logic 0), logic 1 is obtained from port F.

iv) When an input-beam on port B has $\varphi = \pi$ (corresponding to logic 1) and an input-beam on port C has $\varphi = \pi$ (corresponding to logic 1), logic 0 is obtained from port F. These operations are summarized in Table 3.3. To gain more insight into the physics of the NAND logic gate, the field distributions at $\lambda = 1.55$ μm are illustrated in Fig. 3.10, from which it is recognized that the structure functions as a NAND gate. Fig. 3.11 shows the spectrum of the ON to OFF logic-level contrast ratio for the NAND logic gate. Here, we should add that there are three logic 1 states in the NAND operation, but we need to evaluate the worst state in which the least light intensity on port F is obtained. Therefore, we choose the NAND operation of (iii) as the logic 1 state in the calculation of contrast ratio. Then, the smallest ON to OFF logic-level contrast ratio is 22.3 dB in the whole C-band.

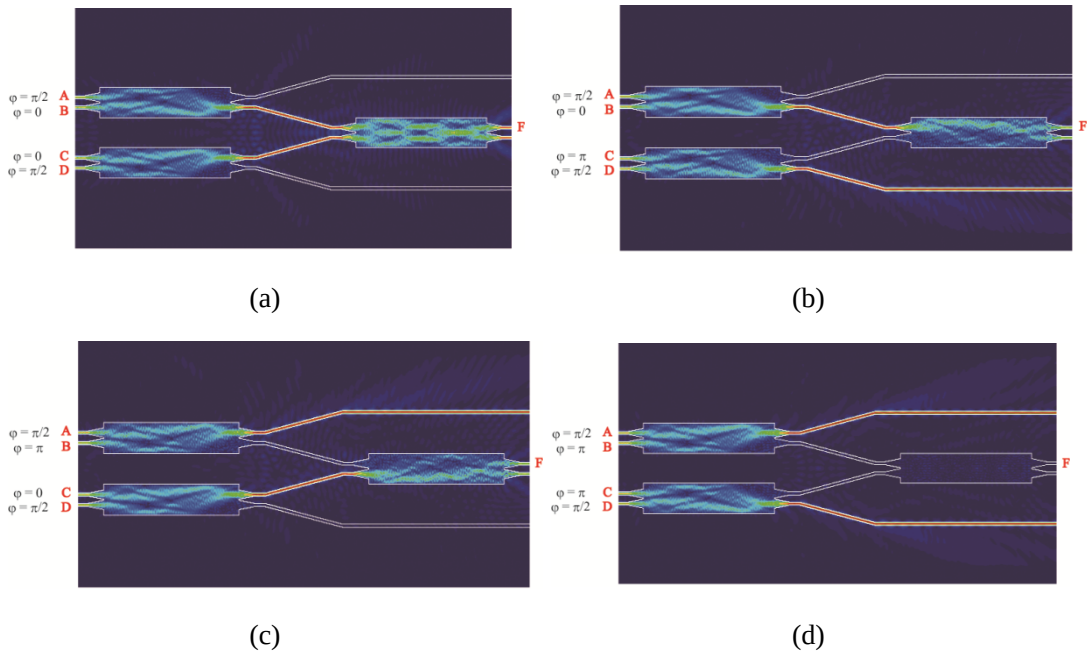


**Fig. 3.10:** Field distributions of the NAND logic gate at an operating wavelength of $\lambda$ = 1.55 μm. (a)-(d) correspond to explanations of the NAND operation (i)-(iv), respectively.

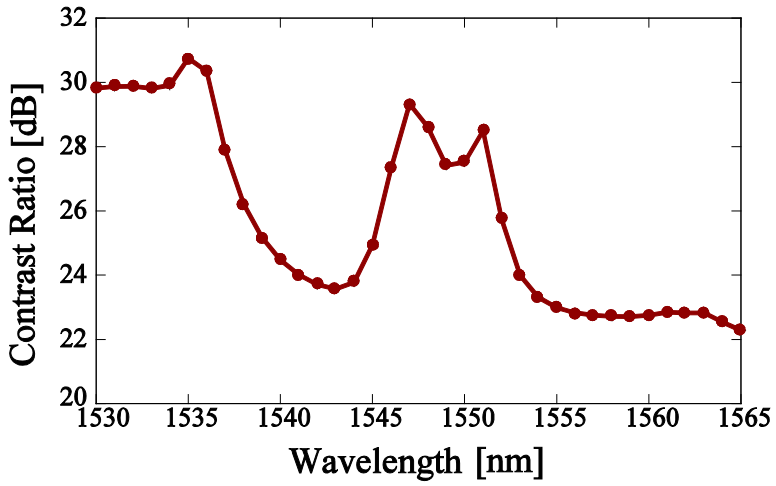


**Fig. 3.11:** The spectrum of the ON to OFF logic-level contrast ratio for the NAND logic gate.

**Table 3.3:** Functions of the NAND logic gate.

| Logical inputs | | | | Logical output |
|---|---|---|---|---|
| B | | C | | F |
| **logic** | $\varphi$ | **logic** | $\varphi$ | **Logic** |
| **0** | 0 | **0** | 0 | **1** |
| **0** | 0 | **1** | $\pi$ | **1** |
| **1** | $\pi$ | **0** | 0 | **1** |
| **1** | $\pi$ | **1** | $\pi$ | **0** |

### 3.3.6 OR Logic Gate

To realize an OR logic gate, the phase of the LO light on ports A and D is $-\pi/2$ when the phase of the BPSK signal is 0 or $\pi$. Moreover, we suppose the same wavelength and polarization between the input-signal light and the LO light. If these requirements have been satisfied, the OR logic gate operates as follows:

i) When an input-beam on port B has $\varphi$ = 0 (corresponding to logic 0) and an input-beam on port C has $\varphi$ = 0 (corresponding to logic 0), logic 0 is obtained from port F.

ii) When an input-beam on port B has $\varphi$ = 0 (corresponding to logic 0) and an input-beam on port C has $\varphi = \pi$ (corresponding to logic 1), logic 1 is obtained from port F.

iii) When an input-beam on port B has a phase $\varphi = \pi$ (corresponding to logic 1) and an input-beam on port C has $\varphi$ = 0 (corresponding to logic 0), logic 1 is obtained from port F.

iv) When an input-beam on port B has $\varphi = \pi$ (corresponding to logic 1) and an input-beam on port C has $\varphi = \pi$ (corresponding to logic 1), logic 1 is obtained from port F. These operations are summarized in Table 3.4.

To gain more insight into the physics of the OR logic gate, the field distributions at $\lambda$ = 1.55 μm are illustrated in Fig. 3.12, from which it is recognized that the structure functions as an OR gate. For the OR logic gate, the smallest ON to OFF logic-level contrast ratio is 22.3 dB. We should note that this result is the same as the case of the NAND logic gate because the differences in operation between the NAND case and the OR case are merely the phase of LO light on the port.

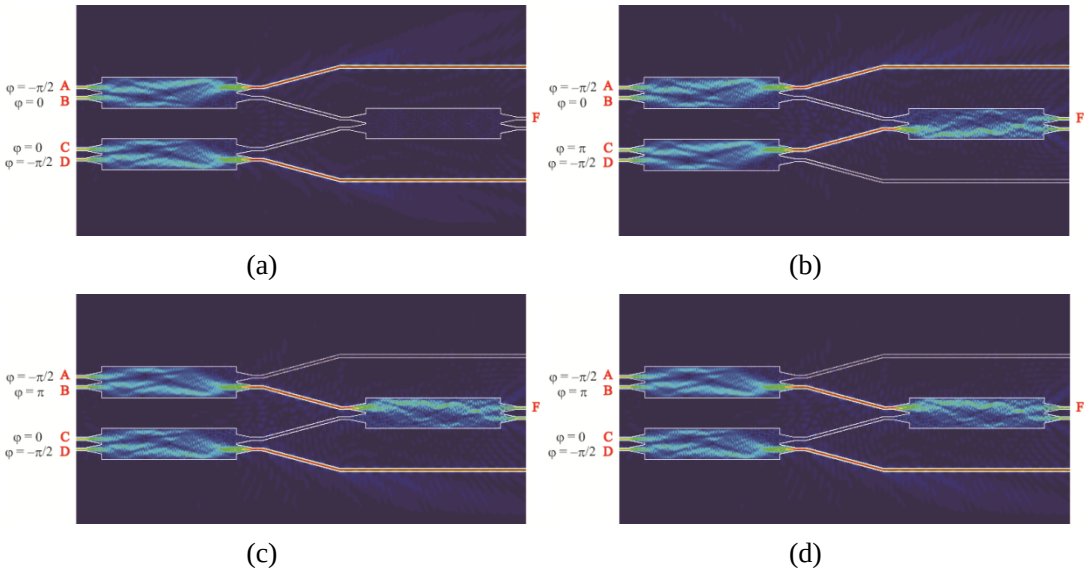


**Fig. 3.12:** Field distributions of the OR logic gate at an operating wavelength of $\lambda$ = 1.55 μm. (a)-(d) correspond to explanations of the OR operation (i)-(iv), respectively.

**Table 3.4:** Functions of the OR logic gate.

| Logical inputs | | | | Logical output |
|---|---|---|---|---|
| B | | C | | F |
| **logic** | $\varphi$ | **logic** | $\varphi$ | **Logic** |
| **0** | 0 | **0** | 0 | **0** |
| **0** | 0 | **1** | $\pi$ | **1** |
| **1** | $\pi$ | **0** | 0 | **1** |
| **1** | $\pi$ | **1** | $\pi$ | **1** |

## 3.4 Architecture of Reconfigurable Optical Logic Gates

Fig. 3.13 shows a schematic of a reconfigurable optical logic gate. The logic gate is composed of three 3-dB couplers based on the MMI waveguide. Ports B' and C' are input ports corresponding to the logical input, and port F is an output port to obtain logical output. In addition, ports A' and D' are input ports for the incident LO light. Also, ports E and H are ports for optical detection, and port G is an idle port. The LO laser and PD are required to construct the PLL whose role is tracking the phase of the BPSK signal [55, 62, 63].

To show operations of the reconfigurable optical logic gate for the BPSK signal, we assume ideal conditions that the phase of the LO light on ports A' and D' should be "0" when the phase of the BPSK signal on ports B' and C' are just "0" or "$\pi$". In the BPSK format, 0-phase corresponds to "logical 0", whereas $\pi$-phase corresponds to "logical 1". Under these conditions, by changing phase of input-lights appropriately ($\Delta\Phi_x$) by means of certain phase shifters, arbitrary logic functions can be realized. Table 3.5 shows operation principles of NAND, OR, XOR, and XNOR logic functions, respectively. As an example, we explain an operation of the NAND logic gate in detail. In the NAND case, the conditions of the phase control are $\Delta\Phi_1 = +\pi/2$, $\Delta\Phi_2 = 0$, $\Delta\Phi_3 = 0$, and $\Delta\Phi_4 = +\pi/2$, respectively. Then, we set the phase of the LO light on ports A and D are "$\pi/2$" and the phase of the BPSK signal is just "0" or "$\pi$".

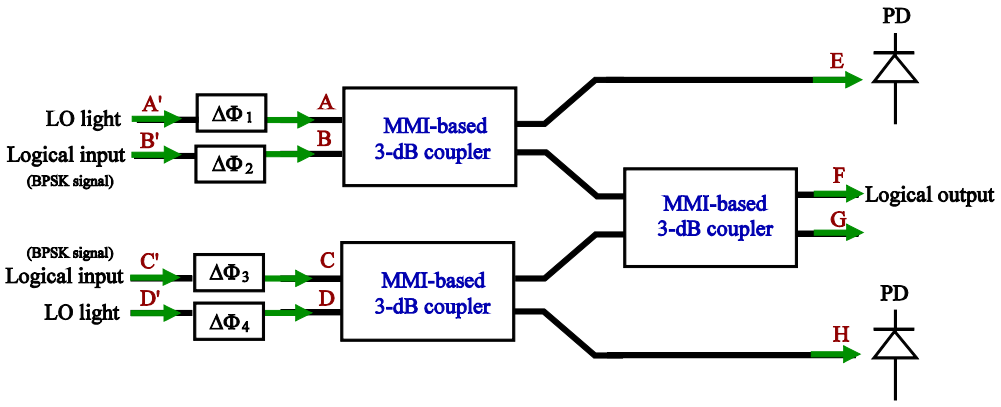


**Fig. 3.13:** Schematic of a reconfigurable optical logic gate. $\Delta\Phi_x$ ($x$ = 1, 2, 3, 4) indicates the amount of phase change of the phase shifter, and the value of $\Delta\Phi_x$ is selected from $+\pi/2$, 0, or $-\pi/2$.

**Table 3.5:** Operation principle of the reconfigurable logic.

| | NAND | OR | XOR | XNOR |
|---|---|---|---|---|
| $\Delta\Phi_1$ | $+\pi/2$ | $-\pi/2$ | $+\pi/2$ | $+\pi/2$ |
| $\Delta\Phi_2$ | 0 | 0 | 0 | 0 |
| $\Delta\Phi_3$ | 0 | 0 | $-\pi/2$ | $+\pi/2$ |
| $\Delta\Phi_4$ | $+\pi/2$ | $-\pi/2$ | 0 | 0 |

# Chapter 4

# 3-D Analysis of Crossing Slot Waveguides

## 4.1 Introduction

Slot waveguides have attracted much attention due to their unique property of strongly confining light to the sub-wavelength scale region [19, 20]. These are useful for active devices because nonlinear optical effects can be greatly enhanced [64]. Many applications have been reported, e.g., all-optical switching [65], polarization splitter [66], and sensing [67-69]. In order to efficiently integrate these devices, interconnect technologies such as slot-waveguide bends and crossing slot waveguides need to be established. So far, slot waveguide bends have been studied [70-72] and recently, a design method for efficient transmission of a crossing slot waveguide has been proposed [23], which gives us a novel perspective and open up a new horizon for the interconnects of slot waveguide-based devices. In [23], by filling up the slots around the cross the transmission was drastically improved, compared with conventional direct-crossings. However, the numerical results were obtained by two-dimensional (2-D) simulations based on the finite-difference time-domain (FDTD) method. In practice, it is necessary to evaluate devices with finite core height as three-dimensional (3-D) structures. For analyzing the characteristics of a certain 3-D structure, the FDTD method [73, 74] is widely used, which is one of the most popular numerical methods. The efficiency in its implementation is the main reason of using the FDTD method, but the FDTD method usually requires a large amount of memory, which brings about increase of computing-time. On the other hand, the finite element method (FEM) [75] is also well known as a useful numerical scheme. The FEM has possibility to reduce consumption of

memory because the size of the mesh can be adaptively configured, and the mesh can be adapted for various forms.

In this chapter, we newly formulate and implement a 3-D vector finite element method (VFEM) for the waveguide discontinuity problem. Through the use of the 3-D VFEM, we investigate transmission characteristics of two types of crossing slot waveguides with finite core height. For direct crossing, 3-D simulation results show almost the same tendency with the earlier 2-D simulation results [23]. On the other hand, for crossing filling up the slots locally, the value of the maximum transmission (78.2%) is relatively low compared with the 2-D structure (97.2%). In the crossing slot waveguide with finite core height, the radiation loss cannot be sufficiently suppressed.

## 4.2 3-D Vector Finite Element Method for Waveguide Discontinuity Problem

### 4.2.1 Historic Background

The Waveguide discontinuity problem is a basic and important subject for designing waveguide devices and circuits [76]. The FEM [40, 77-83] is one of the powerful analysis methods to solve this problem. In the earlier works, the FEM was applied to the finite region including discontinuities, and the mode expansion technique was used for representing infinite uniform waveguides connected to the input and output ports [77-79]. Since the techniques involving the mode expansion boundary condition require the calculation of many modes of the accessing waveguide, as a result, the complicated procedure of numerical framework brings about increase of computation time. During the last decade, the perfectly matched layer (PML) [41, 84] boundary condition was implemented in a number of numerical calculation algorithms for optical waveguides. The PML is an effective non-reflective boundary condition for all incident waves with arbitrary incident angle. By replacing the input and output ports by the PML absorbers, the FEM can be applied to the waveguide discontinuity problem without using the mode expansion technique [40, 80-83]. However, the conventional approaches are limited to 2-D analysis. In 2-D analysis, it is insufficient to evaluate a complicated microstructure with the reflection and the radiation because an analytical approach, e.g. the effective index method, is hard to be applied in regard to the remaining third dimension.

In this work, we implement a 3-D VFEM using port truncation by the PML for the discontinuity problem of optical waveguides, which is our novelty. We use the tetrahedral edge element based on the linear-tangential and quadratic-normal (LT/QN) vector basis function [85]. Additionally incident condition is given by an eigenmode of a uniform waveguide when extracting a 2-D mesh on an incident plane from a 3-D mesh. The eigenmode on the incident plane is determined by using 2-D VFEM based on the hybrid edge/nodal element [39]. We use the commercial software GiD [86] as a mesh generator.

Typical mesh size for a 3-D structure is 572,877. On the other hand, mesh size for a 2-D excitation plane is 2,264. All simulations are conducted on a single core of a 2.5 GHz Quad-Core AMD Optron (tm) Processor 8380. CPU times for 3-D analysis and 2-D analysis are 5823 seconds and 0.9 seconds, respectively.

### 4.2.2 Formulation

We consider a 3-D optical waveguide discontinuity problem surrounded by the PML regions 1-7 with thickness $d_i$ ($i$ = 1, 2, 3), as shown in Fig. 4.1(a). By using the PML for anisotropic media [41], the relative permittivity and relative permeability tensors in the analysis region are expressed as

$$[\varepsilon_{\mathrm{r}}] = n^2[\Lambda], \quad [\mu_{\mathrm{r}}] = [\Lambda] \tag{4.1}$$

with

$$\Lambda = \begin{bmatrix} \frac{s_y s_z}{s_x} & 0 & 0 \\ 0 & \frac{s_z s_x}{sy} & 0 \\ 0 & 0 & \frac{s_x s_y}{s_z} \end{bmatrix}, \tag{4.2}$$

where $n$ is the refractive index, and $s_x$, $s_y$, and $s_z$ listed in Table 4.1 are the PML parameters in the PML region. In non-PML region, $s_x$, $s_y$, and $s_z$ are set to 1. Here, we assume parabolic profiles of complex value of $s_i$ in Table 4.1 as

$$s_i = 1 - j\left(\frac{\rho}{d_i}\right)^2 \tan\delta_i, \tag{4.3}$$

where $\rho$ is the distance from the beginning of the PML and $\delta_i$ is the loss angle at the end of the PML ($\rho = d_i$). From Maxwell's equations, the following vectorial wave equation is derived:

$$\nabla \times ([p]\nabla \times \boldsymbol{\Phi}) - k_0^2[q]\boldsymbol{\Phi} = 0 \tag{4.4}$$

with

$$[p] = [\mu_{\mathrm{r}}]^{-1}, \quad [q] = [\varepsilon_{\mathrm{r}}], \quad \text{for } \boldsymbol{\Phi} = \boldsymbol{E} \tag{4.5}$$

$$[p] = [\varepsilon_{\mathrm{r}}]^{-1}, \quad [q] = [\mu_{\mathrm{r}}], \quad \text{for } \boldsymbol{\Phi} = \boldsymbol{H} \tag{4.6}$$

where $k_0$, $\boldsymbol{E}$, and $\boldsymbol{H}$ are the free-space wavenumber, the electric and the magnetic fields, respectively. In the finite element analysis, solution is obtained by minimizing energy corresponding to the functional $F$ instead of solving (4.4) directly. The minimum of the functional is found by setting the derivative of the functional to zero. The functional is given as an integral form for whole analysis region, and its degree of the derived function is first order lower than that of (4.4). After multiplying left-hand side of (4.4) to $\boldsymbol{\Phi}^*$, we integrate the obtained equation over the region $\Omega$ and perform formula manipulation. Then, $F$ for (4.4) can be expressed as

$$F = \iiint_{\Omega} \left[ \left( \nabla \times \boldsymbol{\Phi}^* \right) \cdot \left( \nabla \times ([p] \nabla \times \boldsymbol{\Phi}) - k_0^2 [q] \boldsymbol{\Phi} \right) \right] dxdydz + \iint_{\Gamma} \boldsymbol{\Phi}^* \cdot [\boldsymbol{i}_n \times ([p] \nabla \times \boldsymbol{\Phi})] d\Gamma = 0, \tag{4.7}$$

where * and $\boldsymbol{i}_n$ denote complex conjugate and the outward unit normal vector, respectively. Dividing the analysis region into the LT/QN tetrahedral edge elements [85], the field $\boldsymbol{\Phi}$ within each element can be approximated as

$$\boldsymbol{\Phi} = \begin{bmatrix} \Phi_x \\ \Phi_y \\ \Phi_z \end{bmatrix} = \begin{bmatrix} \{U\}^T \{\phi\}_e \\ \{V\}^T \{\phi\}_e \\ \{W\}^T \{\phi\}_e \end{bmatrix} = [N]^T \{\phi\}_e \tag{4.8}$$

with

$$[N] = [\{U\} \quad \{V\} \quad \{W\}], \tag{4.9}$$

where $\{\phi\}_e$ is the element edge variable vector, $T$ denotes the transpose of matrix, and $\phi$ represents the amplitude of the electromagnetic field at each edge. $\{U\}$, $\{V\}$, and $\{W\}$ are the shape function vectors for $\Phi_x$, $\Phi_y$, and $\Phi_z$, respectively. We calculate $\nabla \times \boldsymbol{\Phi}$ by using (4.8):

$$\nabla \times \boldsymbol{\Phi} = \begin{bmatrix} \left( \{W_y\}^T - \{V_z\}^T \right) \{\phi\}_e \\ \left( \{U_z\}^T - \{W_x\}^T \right) \{\phi\}_e \\ \left( \{V_x\}^T - \{U_y\}^T \right) \{\phi\}_e \end{bmatrix} = [D]^T \{\phi\}_e \tag{4.10}$$

with

$$[D] = \left[ \{W_y\} - \{V_z\} \quad \{U_z\} - \{W_x\} \quad \{V_x\} - \{U_y\} \right] \tag{4.11}$$

and

$$\begin{aligned} \{U_y\} &\equiv \frac{\partial \{U\}}{\partial y}, \quad \{U_z\} \equiv \frac{\partial \{U\}}{\partial z}, \\ \{V_z\} &\equiv \frac{\partial \{V\}}{\partial z}, \quad \{V_z\} \equiv \frac{\partial \{V\}}{\partial x}, \\ \{W_x\} &\equiv \frac{\partial \{W\}}{\partial x}, \quad \{W_y\} \equiv \frac{\partial \{W\}}{\partial y}. \end{aligned} \tag{4.12}$$

We consider that the incidence plane $\Gamma$ is perpendicular to $z$ axis as shown in Fig. 4.1(b) and divide the region $\Omega$ into two subregions, $\Omega_1$ and $\Omega_2$. The electric/magnetic field in each of subregions represents $\boldsymbol{\Phi}_1$ and $\boldsymbol{\Phi}_2$, respectively. After substituting (4.8) and (4.10) for (4.7), we calculate the sum of all the elements. Then, the boundary integral terms vanish except for $\Gamma$ and the outer boundary of the PML owing to the continuity conditions of the electromagnetic field. Considering that the electromagnetic field on the outer boundary of the PML becomes 0, (4.7) can be written as:

$$F = \left\{ \phi^* \right\}^T [P] \{\phi\} \tag{4.13}$$

with

$$
\begin{aligned}
[P] &= \sum\nolimits_e \iiint_e \left( [D][p][D]^T - k_0^2 [N][q][N]^T \right) dxdydz \\
&= \sum\nolimits_e \iiint_e \Big[ p_x \left( \{W_y\}\{W_y\}^T - \{W_y\}\{W_z\}^T \right. \\
&\quad \left. - \{W_z\}\{W_y\}^T + \{W_y\}\{W_y\}^T \right) + p_y \left( \{U_z\}\{U_z\}^T - \{U_z\}\{W_x\}^T \right. \\
&\quad \left. - \{W_x\}\{U_z\}^T - \{W_x\}\{W_x\}^T \right) + p_z \left( \{V_x\}\{V_x\}^T - \{V_x\}\{U_y\}^T \right. \\
&\quad \left. - \{U_y\}\{V_x\}^T - \{U_y\}\{U_y\}^T \right) \\
&\quad - k_0^2 \left( q_x \{U\}\{U\}^T + q_y \{V\}\{V\}^T + q_z \{W\}\{W\}^T \right) \Big] dxdydz,
\end{aligned}
\tag{4.14}
$$

where $\Sigma_e$ extends over all elements. $[N]_\Gamma$ is a matrix composed of the shape function vectors for $\Gamma$. $p_x$, $p_y$, and $p_z$ are the diagonal elements of $[p]$, and $q_x$, $q_y$, and $q_z$ are the diagonal elements of $[q]$.

Applying the variational principle to (13), the following matrix equation is derived:

$$
\begin{bmatrix} [P]_{00} & [P]_{0\Gamma} \\ [P]_{\Gamma 0} & [P]_{\Gamma\Gamma} \end{bmatrix} \begin{bmatrix} \{\phi\}_0 \\ \{\phi\}_\Gamma \end{bmatrix} = \begin{bmatrix} \{0\} \\ \{\Psi\} \end{bmatrix} \tag{4.15}
$$

with

$$
\{\Psi\}_\Gamma = \sum\nolimits_e{}' \iint [N]_\Gamma [\boldsymbol{i}_z \times ([p]\nabla \times \boldsymbol{\Phi}_1) - \boldsymbol{i}_z \times ([p]\nabla \times \boldsymbol{\Phi}_2)] d\Gamma, \tag{4.16}
$$

where $\{\phi\}_0$ is a vector composed of all the edge variables in the analysis region except for $\Gamma$, and $\{\phi\}_\Gamma$ is a vector composed of all the edge variables on $\Gamma$. $[P]_{00}$, $[P]_{0\Gamma}$, $[P]_{\Gamma 0}$, and $[P]_{\Gamma\Gamma}$ are the partial matrices of $[P]$. $\Sigma_e'$ extends over the elements related to $\Gamma$. Representing the electric/magnetic field $\boldsymbol{\Phi}_i$ ($i$ = 1, 2) as the sum of the incident field $\boldsymbol{\Phi}_{\text{in},\,i}$ and the scattering field $\boldsymbol{\Phi}_{\text{scat},\,i}$, the following equation can be obtained [40]:

$$
\boldsymbol{\Phi}_i = \boldsymbol{\Phi}_{\text{in},i} + \boldsymbol{\Phi}_{\text{scat},i} \tag{4.17}
$$

From the continuity conditions of the tangential electromagnetic components on $\Gamma$, we obtain

$$
\boldsymbol{i}_z \times ([p]\nabla \times \boldsymbol{\Phi}_{\text{scat},1}) = \boldsymbol{i}_z \times ([p]\nabla \times \boldsymbol{\Phi}_{\text{scat},2}). \tag{4.18}
$$

Then, (4.16) becomes

$$
\{\Psi\}_\Gamma = \sum\nolimits_e{}' \iint [N]_\Gamma [\boldsymbol{i}_z \times ([p]\nabla \times \boldsymbol{\Phi}_{\text{in},1}) - \boldsymbol{i}_z \times ([p]\nabla \times \boldsymbol{\Phi}_{\text{in},2})] d\Gamma, \tag{4.19}
$$

Now, we define the incident field as

$$
\boldsymbol{\Phi}_{\text{in},1} = A\boldsymbol{\Phi}_{\text{2D},1}(x, y)\exp(-j\beta z) \tag{4.20}
$$

$$
\boldsymbol{\Phi}_{\text{in},2} = A\boldsymbol{\Phi}_{\text{2D},2}(x, y)\exp(j\beta z) \tag{4.21}
$$

with

$$
\boldsymbol{\Phi}_{\text{2D},1} = \begin{bmatrix} \{U_{\text{2D}}\}_\Gamma^T \{\phi_t\}_e \\ \{V_{\text{2D}}\}_\Gamma^T \{\phi_t\}_e \\ j\beta \{N_{\text{2D}}\}_\Gamma^T \{\phi_z\}_e \end{bmatrix}, \tag{4.22}
$$

$$\mathbf{\Phi}_{2\mathrm{D},2}=\begin{bmatrix}\{U_{2\mathrm{D}}\}_{\Gamma}^{T}\{\phi_t\}_e\\ \{V_{2\mathrm{D}}\}_{\Gamma}^{T}\{\phi_t\}_e\\ -j\beta\{N_{2\mathrm{D}}\}_{\Gamma}^{T}\{\phi_z\}_e\end{bmatrix}, \tag{4.23}$$

where $A$, $\mathbf{\Phi}_{2\mathrm{D},\,i}$, and $\beta$ are amplitude, the 2-D distribution function, and the propagation constant of the incident field, respectively. $\{\phi_t\}_e$ is a vector composed of all the edge variables in the hybrid edge/nodal element, and $\{\phi_z\}_e$ is a vector composed of all the nodal variables in the hybrid edge/nodal element. $\{U_{2\mathrm{D}}\}$, $\{V_{2\mathrm{D}}\}$ are the shape function vectors for the curvilinear edge element, and $\{N_{2\mathrm{D}}\}$ is the shape function vector for the curvilinear nodal element. Substituting (4.20) and (4.21) into (4.19), (4.19) can be written as

$$\begin{aligned}\{\Psi\}_{\Gamma}=2j\beta\sum\nolimits_e{}'\iint\Big[&\Big(p_y\{U_{2\mathrm{D}}\}_{\Gamma}\{U_{2\mathrm{D}}\}_{\Gamma}^{T}+p_x\{V_{2\mathrm{D}}\}_{\Gamma}\{V_{2\mathrm{D}}\}_{\Gamma}^{T}\Big)\{\phi_t\}_e\\&+\left(p_y\{U_{2\mathrm{D}}\}_{\Gamma}\frac{\partial\{N_{2\mathrm{D}}\}_{\Gamma}^{T}}{\partial x}+p_x\{V_{2\mathrm{D}}\}_{\Gamma}\frac{\partial\{N_{2\mathrm{D}}\}_{\Gamma}^{T}}{\partial x}\right)\{\phi_z\}_e\Big]d\Gamma.\end{aligned} \tag{4.24}$$

Note that the discretized 2-D distribution function and the propagation constant are calculated by the 2-D VFEM [39].

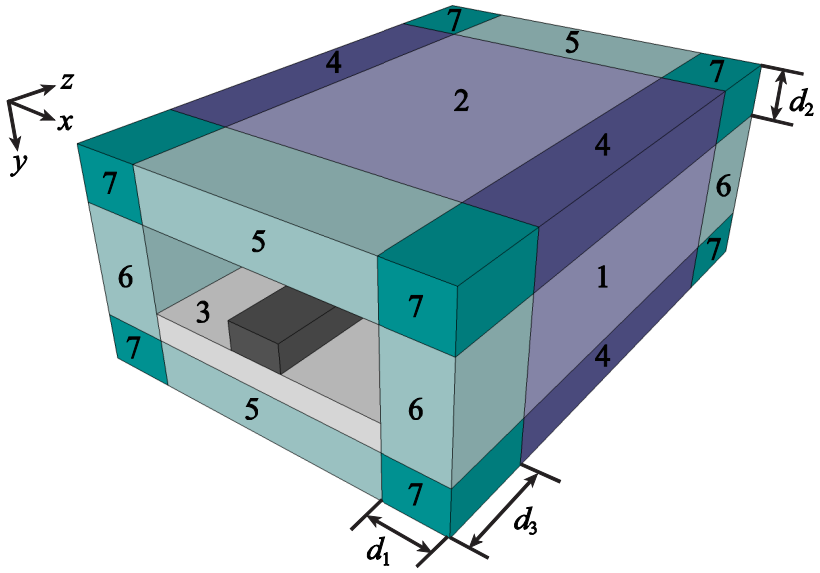


(a)

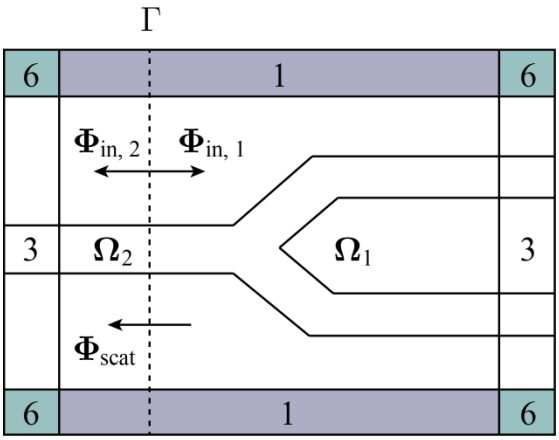


(b)

**Fig. 4.1:** (a) Schematic of a 3-D optical waveguide surrounded by the PML. (b) The *x*-*z* plane for the center of the waveguide.

**Table 4.1:** Values of PML parameters.

| PML | PML region | | | | | | |
|---|---|---|---|---|---|---|---|
| parameters | 1 | 2 | 3 | 4 | 5 | 6 | 7 |
| $s_x$ | $s_1$ | 1 | 1 | $s_1$ | 1 | $s_1$ | $s_1$ |
| $s_y$ | 1 | $s_2$ | 1 | $s_2$ | $s_2$ | 1 | $s_2$ |
| $s_z$ | 1 | 1 | $s_3$ | 1 | $s_3$ | $s_3$ | $s_3$ |

## 4.3 Finite Element Analysis of Crossing Silicon Slot Waveguides

Fig. 4.2 shows 3-D structures of crossing slot-waveguides. We call a direct crossing of a slot waveguide as the non-filled-type crossing (Fig. 4.2(a)), and a crossing filling up the slots around the cross as the filled-type crossing (Fig. 4.2(b)). We assume that the high refractive index medium constructing slot waveguides, upper cladding, and substrate are, respectively, Si with the refractive index of 3.48, air, and $SiO_2$ with the refractive index of 1.46. We set the slot width and height as $w_s$ = 0.05 μm and $h$ = 0.3 μm, respectively. The Si-width is defined as $w_h$ and in the filled-type crossing, the crossing region is filled with Si whose length is $l$.

First, we investigate transmission characteristics of the non-filled-type crossing (Fig. 4.2(a)), where $w_h$ = 0.25 μm and an operation wavelength $\lambda$ is assumed to be 1.55 μm. Table 4.2 shows the normalized maximum transmission power ($T$), and the corresponding normalized reflection power ($R$), crosstalk ($C$), and radiation loss ($RL = 1-T-R-2C$), and the electric-field intensity distribution is shown in Fig. 4.3(a). We can see that 3-D simulation results agree roughly with the earlier 2-D simulation results [23] and that the radiation loss is caused by the diffraction and scattering at the crossing region. To improve the property degradation of the non-filled-type crossing, the filled-type crossing of 2-D structure has been proposed in Ref. [23].

Next, we investigate transmission characteristics of the filled-type crossing (Fig. 4.2 (b)). According to Ref. [23], the radiation loss and the crosstalk can be suppressed by filling up the crossing region for reducing the diffraction angle. Also, the reflection can be suppressed by regarding the filled segments as the Fabry-Perot-like behavior. These are based on mechanisms of increasing the transmission. To confirm the Fabry-Perot-like behavior of the filled segments, we change $l$ from 0.2 μm to 1.4 μm as shown in Fig. 4.4(a). Since the normalized power for the reflection has periodicity, it is recognized that the filled segments perform as the Fabry-Perot-like.

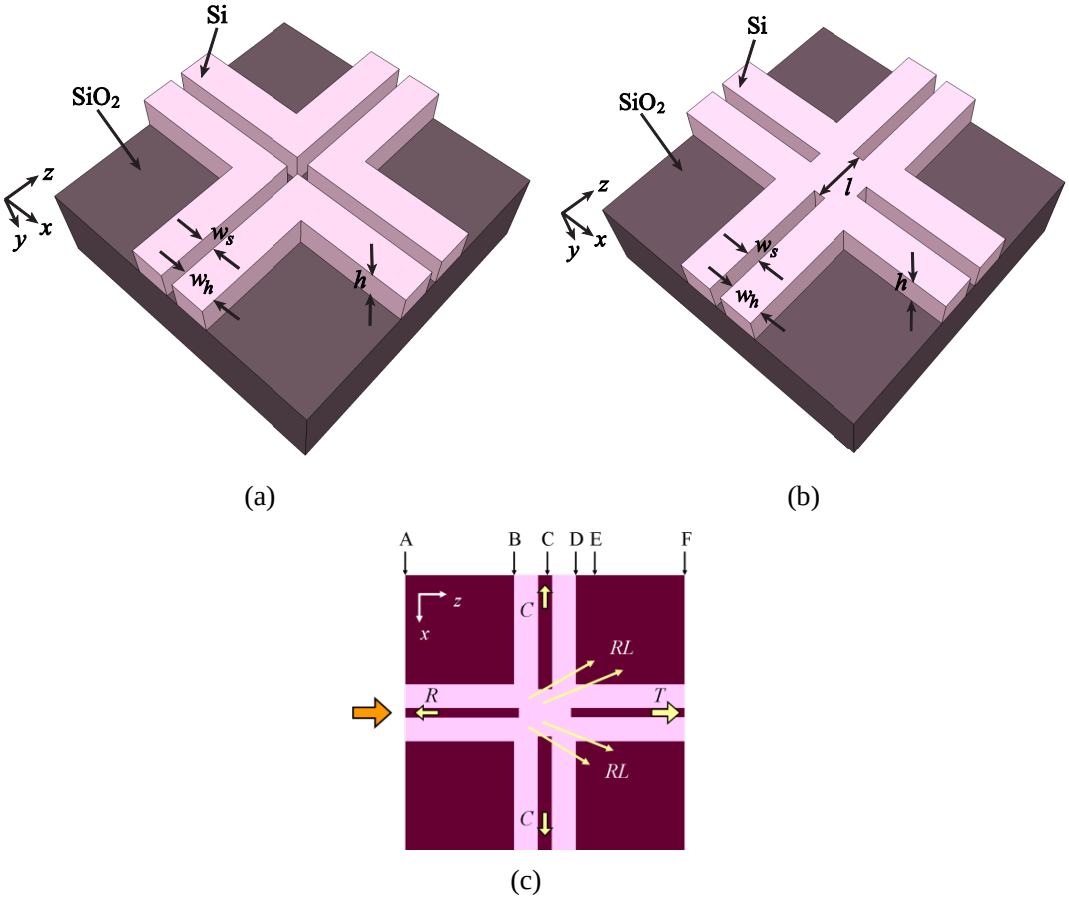


**Fig. 4.2:** 3-D structures of the crossing slot-waveguides defined as (a) non-filled-type, and (b) filled-type crossings. (c) The *x*-*z* plane for the center of the waveguides.

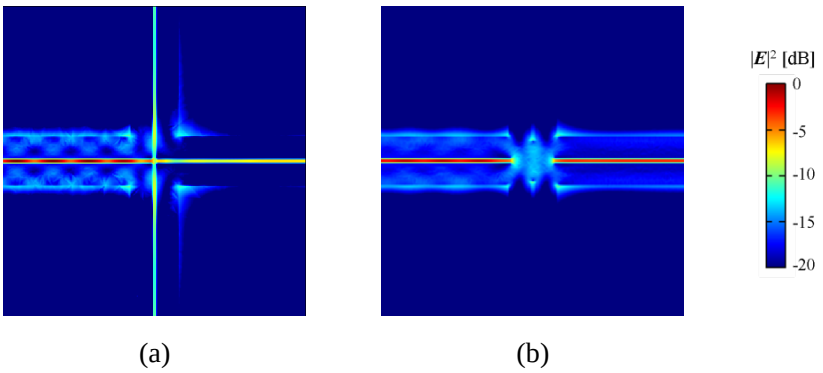


**Fig. 4.3:** Electric field intensity distributions of (a) non-filled-type and (b) filled-type crossings at $\lambda$ = 1.55 μm.

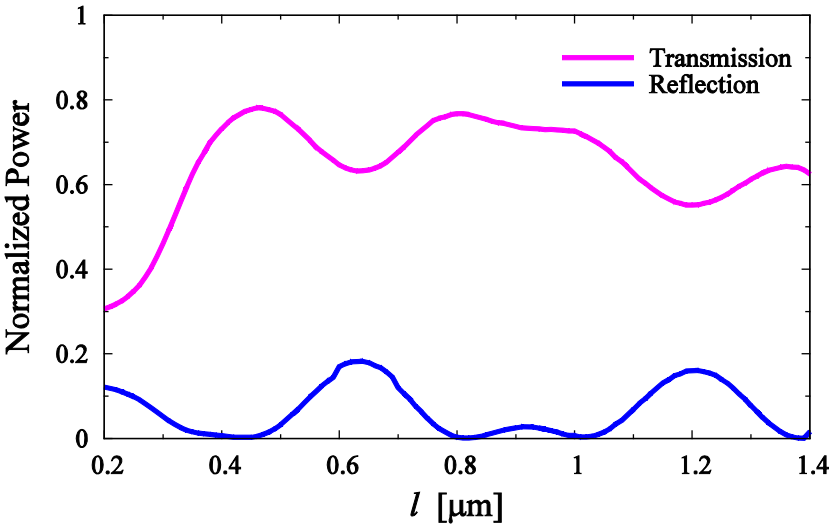


(a)

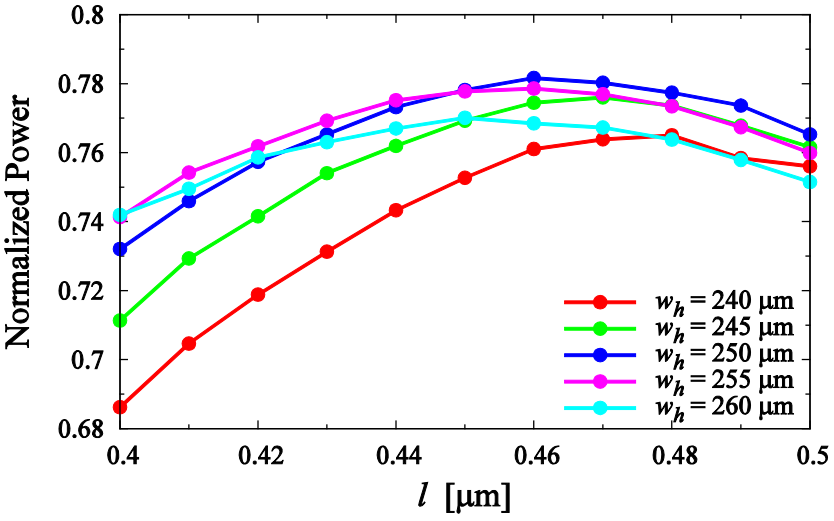


(b)

**Fig. 4.4:** (a) Changes of $l$ from 0.2 μm to 1.4 μm when $w_h$ = 0.25 μm and $h$ = 0.3 μm. (b) Normalized transmission power as a function of length ($l$) filled with Si around the cross, taking Si-width ($w_h$) constructing slot-waveguides as a parameter.

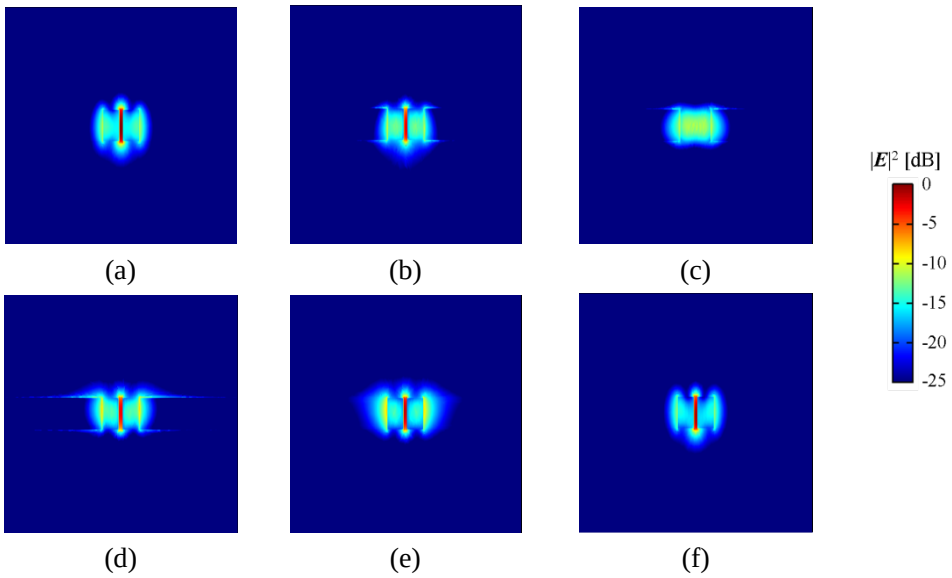


**Fig. 4.5:** The electric field intensity distributions on the *x*-*y* plane in several *z*-positions at $\lambda$ = 1.55 μm. Each of (a)-(f) corresponds to the *z* coordinates of A-F in Fig. 2(c), respectively.

**Table 4.2:** Transmission characteristics of non-filled-type and filled-type crossings.

| Normalized powers | Non-filled-type crossings | | Filled-type crossings | |
|---|---|---|---|---|
| | 2-D [23] | 3-D | 2-D [23] | 3-D |
| $T$ | 35% | 28.5% | 97.2% | 78.2% |
| $R$ | 12% | 6.3% | 0.1% | 0.5% |
| $C$ | 8% | 13.6% | 0.3% | 0.0% |
| $RL = 1-T-R-2C$ | 37% | 38% | 2.0% | 21.4% |

## 4.4 Radiation Loss in 3-D Crossing Structure

To explore a structure having better transmittance of the filled-type crossing when $h$ = 0.3 μm, we change $l$ and $w_h$ in accordance with the design guide mentioned in Ref. [23]. Fig. 4.4(b) shows normalized transmission power as a function of length ($l$) filled with Si around the cross, taking Si-width ($w_h$) constructing slot waveguides as a parameter. The maximum transmission is obtained at $l$ = 0.46 μm and $w_h$ = 0.25 μm. The electric filed intensity distribution is shown in Fig. 4.3(b). By filling up the slots around the cross, the transmission increases from 28.5% to 78.2%, while the reflection $R$ and the crosstalk $C$ both decrease to negligible small due to the Fabry-Perot-like behavior and the diffraction-angle reduction, respectively [23]. However, the value of maximum transmission (78.2%) is relatively low compared with the 2-D structure (97.2%), and the radiation loss is not sufficiently suppressed in the 3-D structure. The cause of this radiation loss can be associated to the coupling loss between the air slot and the Si-filled regions due to the mode field mismatch [87]. For understanding the differences of mode fields intuitively, the electric field intensity distributions on the $x$-$y$ plane in several $z$-positions are illustrated in Fig. 4.5. Here, to reveal components of radiation loss, we consider a coupler of a slot waveguide and a strip waveguide as shown in Fig. 4.6. Fig 4.7 shows the normalized transmission power when changing $l_c$, from which the maximal transmittance is 85.9%. Therefore, the radiation loss (21.4%) shown in Table 4.2 can be roughly divided into the coupling loss (14.1%) and the scattering loss (7.3%) due to having cross ports.

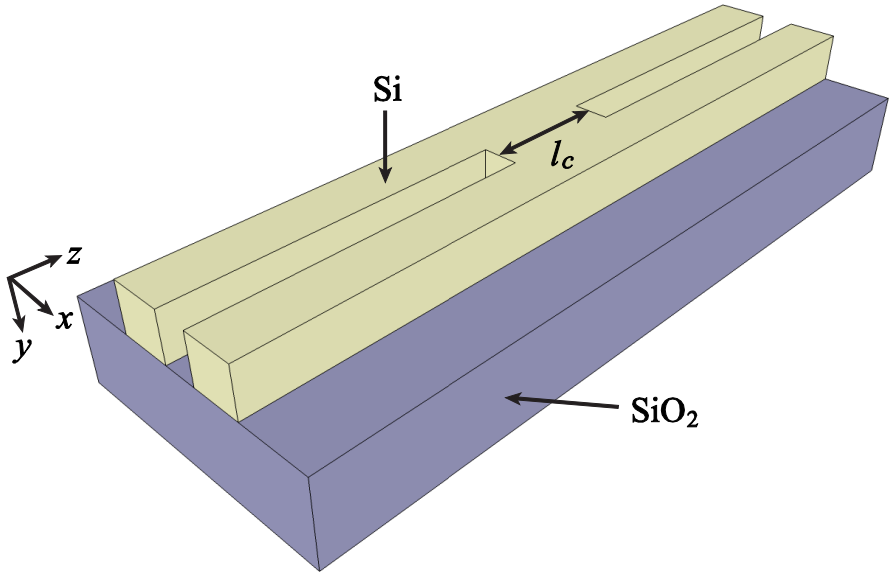


**Fig. 4.6:** Structure of a coupler between a slot waveguide and a strip waveguide, where $l_c$ is the length of the strip waveguide corresponding to the filled segment. The Si-width clipping slot, slot width, and height are, respectively, 0.25 μm, 0.05 μm and 0.3 μm.

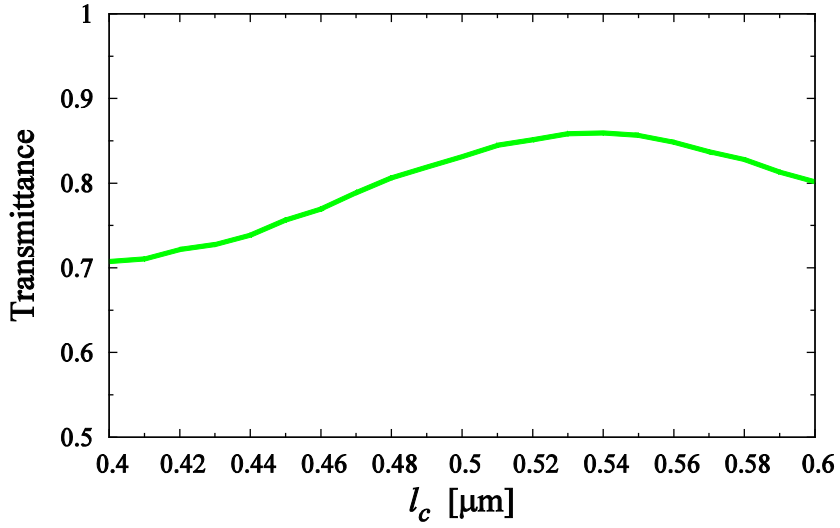


**Fig. 4.7:** Transmission when characteristics changing $l_c$.

# Chapter 5

# Bent and Crossing Silicon Slot Waveguides

## 5.1 Introduction

Slot waveguides can strongly confine light to the low-index sub-wavelength scale region [19, 20], which can enhance light-matter interactions. Due to the selectiveness of covered low-index materials, slot waveguides are used in several applications, such as optical modulators [88, 89], optical nonlinear devices [64, 65, 90], biosensing circuits [67, 68, 91], and athermal waveguides [21, 22]. To efficiently integrate these devices, transmission-efficient bent slot waveguides and crossing slot waveguides need to be developed. Anderson *et al.* improved bending efficiency using asymmetric slot-based structures, but did not consider losses due to transitions from a straight waveguide to a bent slot waveguide [70]. Ma *et al.* presented right-angle bends based on a corner mirror and different resonant cavities, but their numerical results were limited to two-dimensional (2-D) analysis [71]. Su *et al.* proposed a design method for transmission-efficient 2-D crossing slot waveguides [23]. In [23], by filling up slots around the crossing, the transmission efficiency was improved compared with that of direct crossings. The numerical results of Su *et al*. were obtained by 2-D simulations based on the finite-difference time-domain (FDTD) method, which assumes infinite core height. In Chapter 4, we have revealed that when considering a core height of the crossing slot waveguide in [23], the finite height caused a large coupling loss between an air slot and a Si-filled region due to the mode field mismatch [87].

In this chapter, we present a transmission-efficient bent silicon slot waveguide and crossing silicon slot waveguide. To evaluate the transmission efficiency, we use the three-dimensional (3-D) vector finite-element method (VFEM) for the waveguide discontinuity problem [92]. First, we investigate the transmission characteristics of a bent

silicon slot waveguide that has straight input and output waveguides. To construct the bent waveguide, an asymmetric geometry is employed [70]. We introduce a taper to efficiently connect the bent region to the straight waveguides. Numerical results show that the transmission efficiency is increased by optimizing parameters of the taper geometry. When the bending radius is 1 μm, the transmission efficiency is greatly improved from 33.8% to 84.2%. Next, we investigate the transmission characteristics of a 3-D crossing slot waveguide that has a vertical coupler. A comparison between the proposed structure and the conventional crossing structure [23] shows that the maximum transmission efficiency increases from 78.2% to 95.9%.

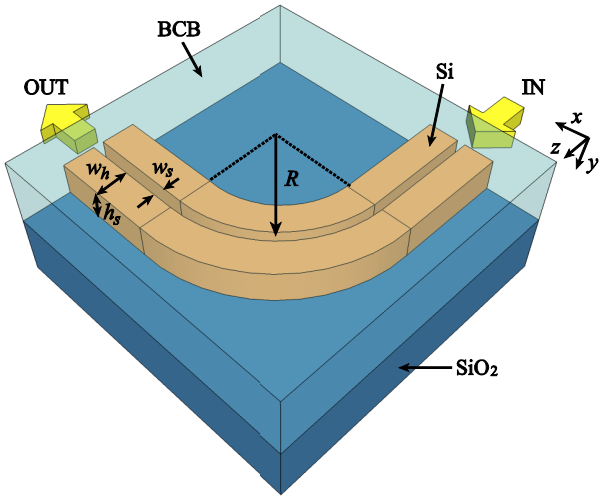


(a)

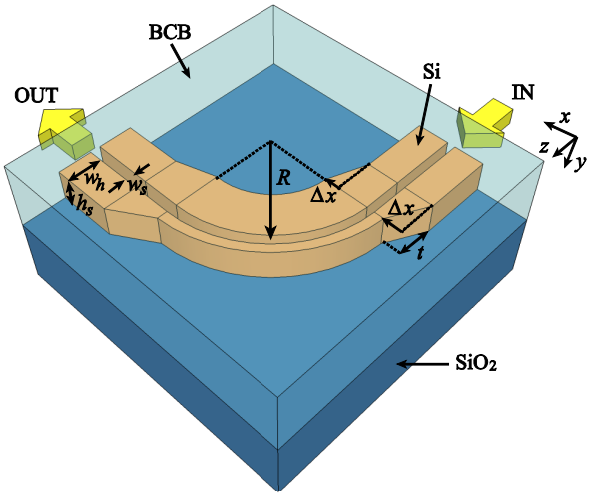


(b)

**Fig. 5.1:** Schematics of (a) a conventional silicon slot waveguide bend and (b) a silicon slot waveguide bend with an asymmetric slot.

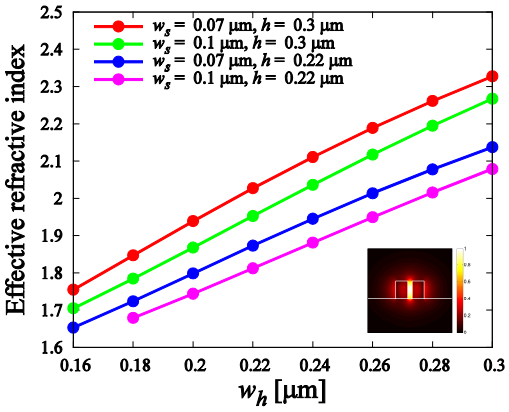


(a)

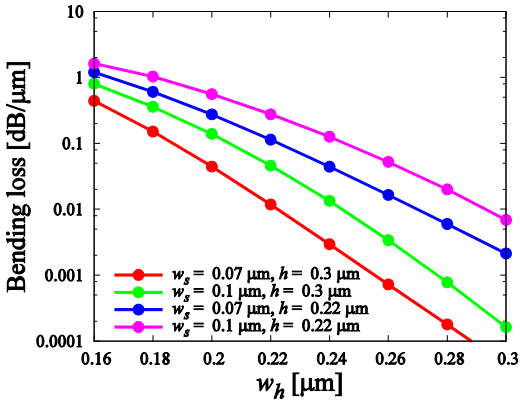


(b)

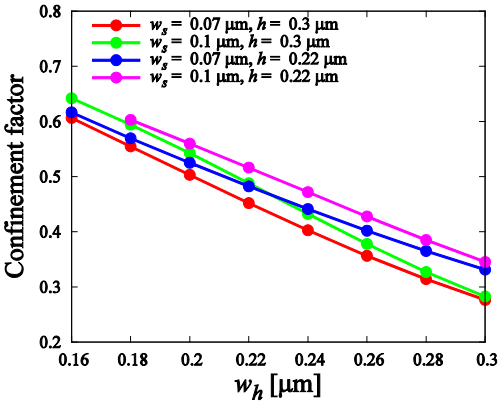


(c)

**Fig. 5.2:** (a) The effective refractive index, (b) the bending loss, and (c) the confinement factor of the silicon slot waveguide as a function of the Si-width $w_h$.

## 5.2 Bent Silicon Slot Waveguides

Figs. 5.1(a) and (b) show schematics of a conventional silicon slot waveguide bend and a silicon slot waveguide bend that has an asymmetric slot, respectively. Typically, the slot region is filled with certain materials, for example, electro-optic material [88], nonlinear material [64], aqueous solution [67], and materials for athermal waveguides [21, 22]. In our work, the silicon slot waveguide is embedded with Benzocyclobutene (BCB), which can be used for athermal on-chip interconnects [22]. We assume that the refractive indexes of Si, $SiO_2$, and BCB are 3.47, 1.45, and 1.54, respectively. In the structure, the length of the straight input/output waveguide is 2 μm. We define the slot width, the waveguide height, and the Si-width as $w_s$, $h$, and $w_h$, respectively. The bending radius is defined as $R$. In addition, we define the taper length and the offset distance as $t$ and $\Delta x$, respectively.

To investigate the influence of the parameter selection, we evaluated the effective refractive index $n_{\text{eff}}$, bending loss, and the confinement factor when changing the slot width and the waveguide height. Figs. 5.2(a) and (b) show the effective refractive index and the bending loss of the silicon slot waveguide as a function of $w_h$, respectively. The effective refractive index increases as $w_h$ becomes lager. From Figs. 5.2(a) and (b), we can see that the bending loss is related to the effective refractive index. Specifically, it has been noted that a high effective refractive index leads to reduction of the bending loss. Fig. 5.2(c) shows the confinement factor in the cover medium (slot region) when changing $w_h$. The confinement factor Γ is evaluated using the following equation [93]:

$$\Gamma = \frac{\iint_{\text{slot}} \text{Re}\left( \boldsymbol{E} \times \boldsymbol{H}^* \right) \cdot \boldsymbol{i}_z dxdy}{\iint_{\text{total}} \text{Re}\left( \boldsymbol{E} \times \boldsymbol{H}^* \right) \cdot \boldsymbol{i}_z dxdy}, \tag{5.1}$$

where $\boldsymbol{E}$ and $\boldsymbol{H}$ are the electric field and the magnetic field, respectively, and $^*$ denotes the complex conjugate. If we choose parameters that result in a high effective refractive index, we can obtain a low bending loss. However, the effect of the slot waveguide, namely, the contribution of the strong light confinement in the slot region, becomes weaker if the confinement factor is small. In other words, there exists a trade-off between the bending loss and the effect of the light confinement in the slot region. Here, we set the slot width of 0.07 μm and the waveguide height of 0.3 μm, which have been used for the conventional slot waveguides [23, 92]. Then, considering the trade-off relation, we set $w_h$ to 0.2 μm ($n_{\text{eff}}$ = 1.939) for the bent silicon slot waveguide. Indeed, several studies set the effective refractive index of less than 2.0 [22, 94].

To investigate the influence of the coupling loss between a bent region and straight waveguides, we evaluated the transmission characteristics of the bent silicon slot waveguide having straight input/output ports (Fig. 5.1(a)) and a uniform 90-degree bend without straight

input/output ports as shown in Fig. 5.3(a). In the 3-D simulation, the normalized transmission power $P$ is obtained by the mode overlap integral:

$$P = \left| \frac{\iint \left( \boldsymbol{E}_{\text{out}} \times \boldsymbol{H}_0^* \right) \cdot \boldsymbol{i}_z dzdy}{\iint \left( \boldsymbol{E}_{\text{in}} \times \boldsymbol{H}_{in}^* \right) \cdot \boldsymbol{i}_x dxdy} \right|, \tag{5.2}$$

where $\boldsymbol{E}_{\text{in}}$ and $\boldsymbol{H}_{\text{in}}$ are the electric field and the magnetic field at the input port, respectively. $\boldsymbol{E}_{\text{out}}$ and $\boldsymbol{H}_0$ are the propagated electric field and the intrinsic magnetic field at the output port, respectively. On the other hand, the transmission efficiency of the uniform 90-degree bend (Fig. 5.3(a)) is evaluated using the cylindrical coordinate-based 2-D VFEM [95], from which the bending loss [dB/μm] is obtained. The transmission efficiency $P_{\text{uniform}}$ of the uniform 90-degree bend is calculated using the following equation:

$$10 \log P_{\text{uniform}} = (\textit{Bending loss}\,[\text{dB/}\mu\text{m}]) \frac{\pi R}{2}. \tag{5.3}$$

In Fig. 5.3(b), the difference of transmission efficiency at the same bending radius corresponds to the coupling loss between the bent region and the straight input and output waveguides. When $R$ = 5 μm and $R$ = 2 μm, the coupling losses are 0.11 dB and 0.69 dB, respectively.

We consider the silicon slot waveguide bend with an asymmetric slot (Fig. 5.1(b)). We introduce a taper to connect the asymmetric slot bend to the straight input/output waveguides. At the junction points, the slot geometry is not changed, while the outer geometry near the cladding is transformed because the light intensity in the cladding is weaker than that in the slot. Fig. 5.4(a) shows the transmission efficiency with respect to $\Delta x$ when $t$ = 0.5 μm. Results of the normalized transmission power at $\Delta x$ = 0 μm correspond to the case of the conventional silicon slot waveguide bend. We can see that the transmission efficiency at each bending radius is improved by optimizing $\Delta x$. Compared with the conventional silicon slot waveguide bend ($\Delta x$ = 0), the transmission efficiency increases from 88.0% to 94.9% when $R$ = 3 μm and from 97.1% to 98.7% when $R$ = 5 μm. When $R$ = 1 μm, the transmission efficiency is drastically improved from 33.8% to 84.2%. We can see that the improvement of the transmission efficiency becomes larger as the bending radius decreases. The offset distance that results in the maximum transmission efficiency also becomes larger as the bending radius decreases. These comparisons are summarized in Table 5.1. To optimize the taper geometry, we evaluated the normalized transmission power as functions of the taper length $t$ and the offset distance $\Delta x$ as shown in Figs. 5.4(b)-(d). In the case of $R$ = 1 μm and $R$ = 2 μm, the transmission is improved as the taper length becomes shorter. On the other hand, when $R$ = 3 μm, the transmission is slightly improved as the taper length becomes shorter. In other words, the influence of the taper length is low when the bending radius is large. Compared with the right-angle slot waveguide bend whose maximum transmission was 94.3% [71] (state-of-the-art), our bent structure can achieve a high transmission when $R$ > 3 μm.

We estimate the propagation loss of our proposed bent structure. According to [96], the measured propagation loss of the silicon slot waveguide that has $w_s$ = 0.1 μm, $h$ = 0.22 μm, and $w_h$ = 0.27 μm was 16.7 dB/cm. After conducting five cycles of the RCA clean, the propagation loss of the silicon slot waveguide was reduced from 16.7 dB/cm to 7.0 dB/cm for the quasi-TE mode [96]. The propagation loss for the mode is approximately given by the product of the confinement factor and the scattering attenuation coefficient in the sidewalls [96]. The confinement factor of the reported silicon slot waveguide is 0.4 as shown Fig. 5.2(c). Therefore, the propagation loss of our structure is estimated to be about 25% larger than the reported silicon slot waveguide because the confinement factor of our structure is 0.5.

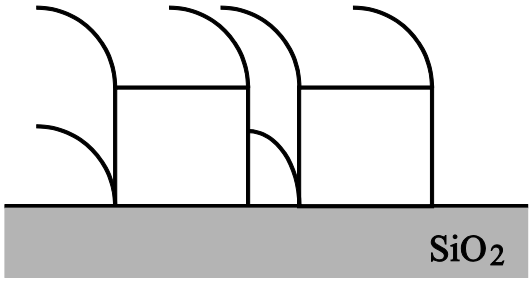


(a)

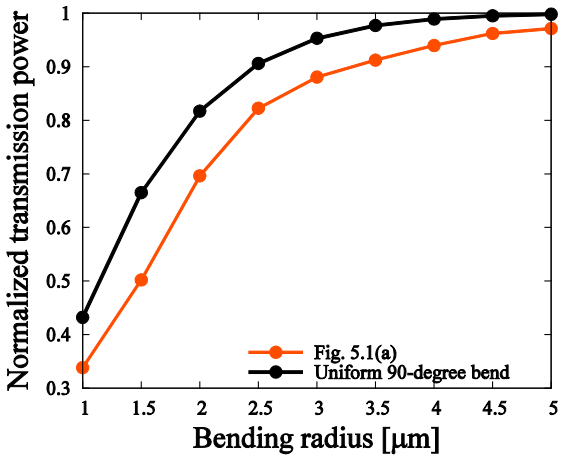


(b)

**Fig. 5.3:** (a) Schematic of a uniform 90-degree bend of the silicon slot waveguide without straight input/output ports, and (b) the transmission characteristics of the bent silicon slot waveguide with straight input/output ports (Fig. 5.1(a)) and the uniform 90-degree bend.

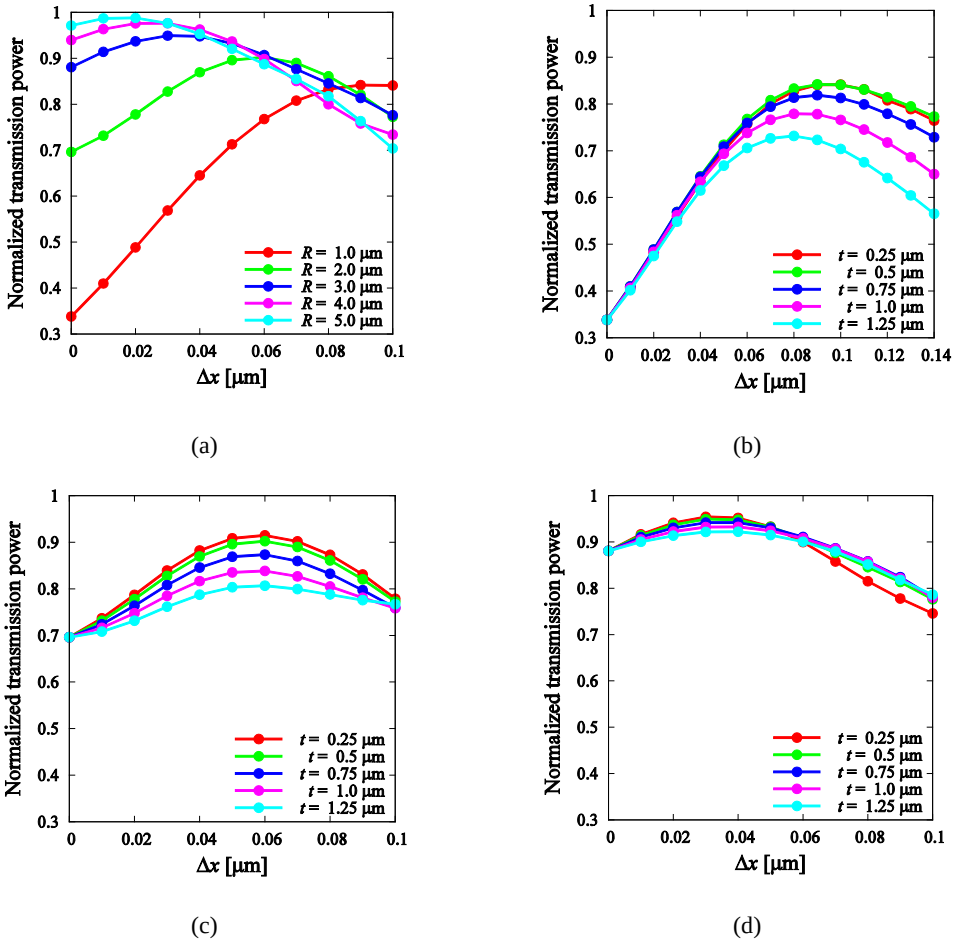


**Fig. 5.4:** (a) The transmission efficiency with respect to $\Delta x$ when $t$ = 0.5 μm, and the transmission efficiency as functions of $\Delta x$ and t when (b) $R$ = 1 μm, (c) $R$ = 2 μm, and (d) $R$ = 3 μm.

**Table 5.1:** Comparison between the conventional bent structure and our bent structure when $t$ = 0.5 μm.

| $R$ [μm] | Transmission efficiency for Fig. 5.1(a) [%] | Maximum transmission efficiency for Fig. 5.1(b) [%] |
|---|---|---|
| 1 | 33.8 | 84.2 |
| 2 | 69.6 | 90.2 |
| 3 | 88.0 | 94.9 |
| 4 | 93.9 | 97.6 |
| 5 | 97.1 | 98.7 |

## 5.3 Crossing Silicon Slot Waveguides

A method for designing efficiently transmitting crossing silicon slot waveguides was proposed [23]. By filling up the slots around the cross, the transmission was improved compared with conventional direct crossings. However, their numerical results were obtained by 2-D simulations based on the FDTD method. In Chapter 4, we have investigated the transmission characteristics of a crossing silicon slot waveguide with finite core height and have revealed that the conventional crossing structure has a large coupling loss between the slot waveguide and the Si-filled segment [92]. To avoid the coupling loss due to the mode field mismatch, we propose in this section a 3-D crossing silicon slot waveguide with a vertical coupler as shown in Figs. 5.5(a) and (b). The Slot waveguide is embedded with BCB, and a Si wire waveguide, which is the vertical coupler, is bonded on the BCB surface. We assume that the refractive indexes of Si, $SiO_2$, and BCB are 3.47, 1.45, and 1.54, respectively. In the proposed structure, the slot width and height are $w_s$ = 0.07 μm and $h_s$ = 0.3 μm, respectively [92]. To make the coupling length as short as possible, we set $w_h$ to 0.18 μm. The coupling length is determined by the overlap of the evanescent fields in two parallel waveguides. To obtain a large overlap of the evanescent fields, a structure that has a low effective refractive index should be selected. We define the width and height of the Si wire as $w$ and $h$, respectively. The distance between the Si wire waveguide and the slot waveguide is defined as $h_g$, and the length of the parallel region is $L$. Our proposed crossing silicon slot waveguide can be fabricated as follows. A Si under layer is first etched to form slot waveguides, and BCB can be spin-coated on the slot waveguides [21]. Next, a Si wire waveguide can be bonded on the BCB surface [97]. Another possible fabrication way is to deposit amorphous silicon. After embedding BCB, amorphous silicon can be deposited on the BCB surface [98]. And then, the amorphous silicon layer can be etched to form a Si wire waveguide. Fig. 5.6 shows the effective refractive index of the Si wire waveguide as a function of the width of the Si wire when $h$ = 0.2 μm. To achieve the phase matching between modes of the slot waveguide and the Si wire, we set the width of the Si wire to 0.36 μm because the effective refractive index of the slot waveguide is 1.847 (Fig. 5.2(a)). To determine a value of $L$, we conducted an eigen mode analysis for an $x$-$y$ plane in the coupling region (Fig. 5.5(b)). Using the obtained effective refractive indexes of supermodes, we can calculate the coupling length $L_c$ as follows:

$$L_c = \frac{\lambda}{2(n_{\mathrm{eff}\,0} - n_{\mathrm{eff}\,1})}, \tag{5.4}$$

where $n_{\mathrm{eff}0}$ and $n_{\mathrm{eff}1}$ are the effective refractive indexes of the fundamental supermode and the first order supermode, respectively, and $\lambda$ is the operating wavelength. From (5.4), $L_c$ becomes 6.25 μm when $h_g$ = 0.35 μm.

First, we set $L$ to 6.25 μm and $h_g$ to 0.35 μm. Fig. 5.7(a) shows the wavelength dependence of the normalized transmission and reflection powers when light is inputted from port A. We find that the transmission efficiency is over 79.5% in the whole C-band, whereas

the normalized reflection is less than 0.5% in the whole C-band. Typically, the crosstalk in a 3-D crossing waveguide is smaller than the back reflection [99]. Our structure can also achieve this condition. The maximum transmission efficiency increases from 78.2% for the conventional crossing structure [92] to 95.9% for our proposed structure. Fig. 5.7(b) shows the wavelength dependence of the normalized transmission and reflection powers when light is inputted from port B. We find that the transmission efficiency is over 95.3% in the whole C-band. However, the transmission efficiency when light is inputted from port B is somewhat low, even though light is not coupled into the Si wire waveguide. To understand this result, we evaluated the transmission efficiency with respect to $h_g$. Fig. 5.8(a) shows the normalized transmission power as a function of $h_g$ when light is inputted from port B. From this figure, we can see that the transmission efficiency exceeds 99% if $h_g$ is over 0.5 μm. A possible explanation is that the scattering loss occurs due to a collision with the Si wire waveguide when $h_g$ is small. Fig. 5.8(b) shows the wavelength dependence of the normalized transmission power with respect to $h_g$ when light is inputted from port A. Here, the values of $L$, which is given by (5.4), are summarized in Table 5.2. When choosing a large $h_g$, the transmission bandwidth tends to become narrower. On the other hand, the transmission bandwidth tends to become wider when choosing a small $h_g$, while the maximal transmission decreases. We can conclude that there exists a trade-off between the transmission bandwidth and the highest transmission power when light is inputted from port A. Recently, a crossing slot waveguide using the slot-to-strip mode converter and the strip-multimode-waveguide crossing has been proposed [100] (state-of-the-art). The reported structure has a large bandwidth and a high transmission of 98%, but results were obtained by the 2-D simulations. In the 3-D structure of the multimode-interference-based crossing waveguide, transmission was 95.3% at the wavelength of 1.55 μm [101]. Therefore, although the bandwidth is reduced, our crossing structure achieves a high transmission compared with the state-of-the-art [100].

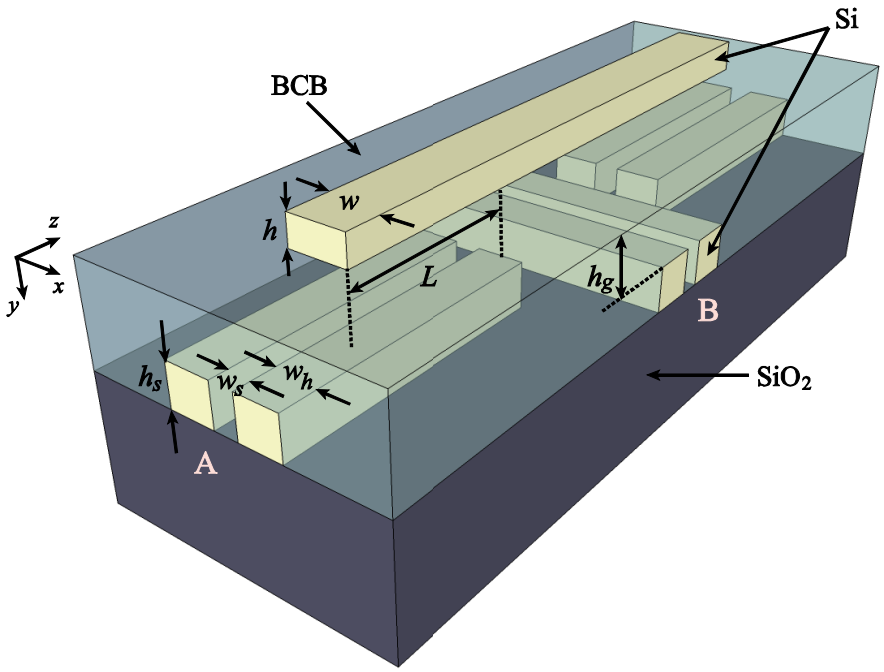


(a)

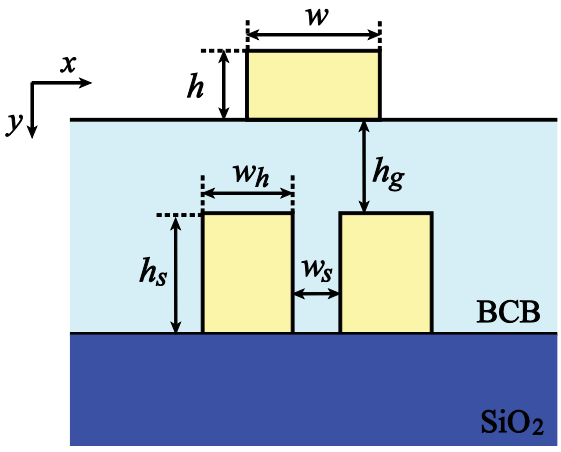


(b)

**Fig. 5.5:** Schematic of (a) a three-dimensional crossing silicon slot waveguide with a vertical coupler and (b) the *x*-*y* plane in the coupling region.

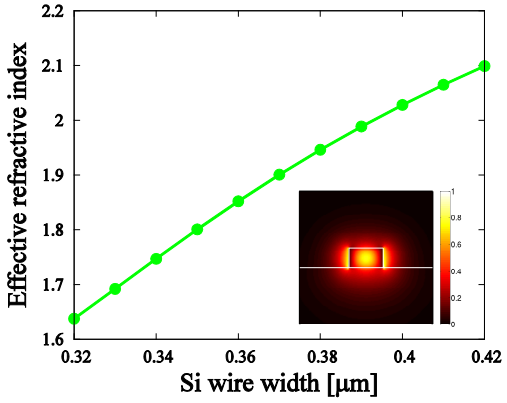


**Fig. 5.6:** The effective refractive index of the Si wire waveguide as a function of the width of the Si wire when $h$ = 0.2 μm.

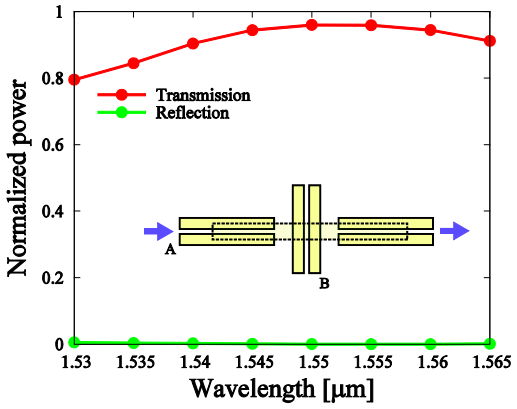


(a)

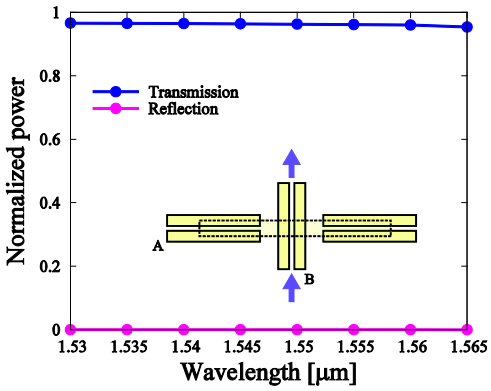


(b)

**Fig. 5.7:** The wavelength dependence of the normalized transmission and reflection powers when light is inputted from (a) port A and (b) port B.

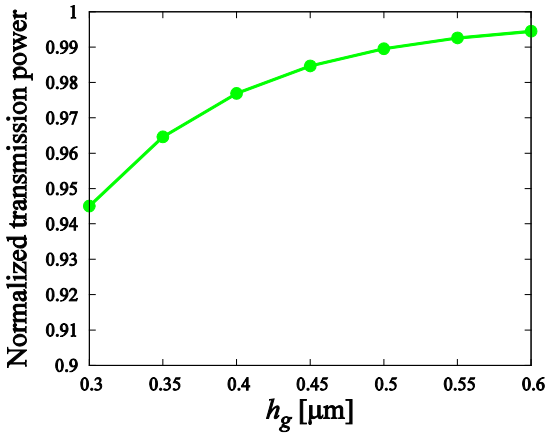


(a)

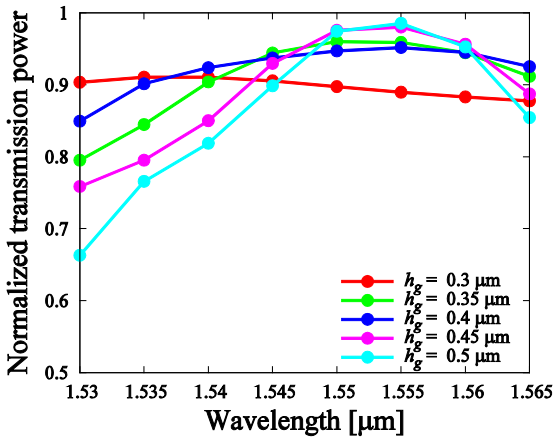


(b)

**Fig. 5.8:** (a) The normalized transmission power as a function of $h_g$ when light is inputted from port B, and (b) the wavelength dependence of the normalized transmission power with respect to $h_g$ when light is inputted from port A.

**Table 5.2:** The values of $h_g$ and $L$.

| $h_g$ [μm] | $L$ [μm] |
|---|---|
| 0.3 | 4.8 |
| 0.35 | 6.25 |
| 04 | 8.11 |
| 0.45 | 10.45 |
| 0.5 | 13.4 |

# Chapter 6

# Metal-Assisted Photonic Modes in Hybrid Plasmonic Waveguides

## 6.1 Introduction

Photonic integration chips play a key role in optical communications, information processing, and biological sensing in terms of cost and energy consumption. A well-established approach to the photonic integration is to use a high-index-contrast waveguide such as a Si wire waveguide [74, 102]. Recently, nanoscale optical waveguides based on surface plasmon polariton (SPP) have attracted researchers because the SPP mode is strongly localized in the nanoscale region. To date, various types of SPP-based waveguides have been reported, for example, metallic wire [103], metallic nanoparticle [104], metal-insulator-metal (MIM) [24, 25], V-groove [26, 27], and dielectric-loaded SPP (DLSPP) [28-30] waveguides. A hybrid plasmonic waveguide (HPW) was proposed [31] that achieves sub-wavelength confinement and is able to mitigate the problem of propagation loss. The HPW is constructed by sandwiching a low-index material between metal and a high-index material. By adjusting the thickness of the low-index material, hybridization of the photonic mode and the SPP (plasmonic) mode can be controlled. Since this initial study, various HPW structures have been proposed [32-36, 105-108] to realize low-loss propagation and sub-wavelength confinement simultaneously. HPW structures are compatible with CMOS technology [32-36], which is important for photonic integrations. Moreover, Si-based HPWs with metal under cladding structures are suitable to realize a higher index contrast compared with Si wire waveguides with $SiO_2$ under claddings [35, 36]. Although most studies on plasmonic waveguides have concentrated on using the plasmonic mode, Yang et al., showed that the metal-assisted photonic mode has a five times longer propagation length and higher transmission efficiency for the 90-degree bend compared with the plasmonic mode in a

DLSPP waveguide [37]. Considering the above-mentioned advantages for the plasmonic mode in Si-based HPWs with metal under claddings, these effectiveness and characteristics for the metal-assisted photonic mode should be discussed.

In this chapter, we theoretically investigate fundamental characteristics of the metal-assisted photonic mode in a Si-based HPW with a metal under cladding using the two-dimensional (2-D) vector finite element method (VFEM) [39]. The Si-based HPW is CMOS compatible and can achieve a higher index contrast compared with Si wire waveguides. Numerical results show that the metal-assisted photonic mode can achieve long-range propagations and large confinement factors in the over cladding. In addition, a superior balance of the bending and the coupling can be obtained compared with the Si wire waveguide, as it enables dense photonic integrations.

## 6.2 Metal-Assisted Photonic Modes

In this section, we explain about the metal-assisted photonic mode in view of the optical waveguide theory, and then show that SPP occurs by the minor electric field component in the metal-assisted photonic mode. Figs. 6.1(a) and (b) show the visualized definitions of the quasi-TE mode and the quasi-TM mode for the electric field, respectively. While the quasi-TE mode has $E_x$ and $E_z$ components, it does not have an $E_y$ component. In contrast, the quasi-TM mode does not have an $E_x$ component. The guided modes of the high-index-contrast 3-D waveguides represented by the Si wire waveguide are frequently treated as the quasi-TE and the quasi-TM modes. Although these modal descriptions include approximations, they are convenient in most cases. Specifically, the minor electric field components of the quasi-TE mode ($E_y$) and quasi-TM mode ($E_x$) are approximated to zero. However, all electric field components originally existed in 3-D optical waveguides [109]. In this case, the guided modes are defined as $E^x_{pq}$ and $E^y_{pq}$ modes [109] as shown in Figs. 6.1(c) and (d), where the subscripts $p$ and $q$ represent the mode order in the $x$ and $y$ directions, respectively. Since the $E_y$ component in the $E^x_{pq}$ mode is perpendicular to the metal surface, the minor component will excite SPP.

To verify this consideration, we analyzed modes of a Si wire waveguide and a Si-based plasmonic waveguide [30] using the 2-D VFEM [39]. In this simulation, the cores and the over claddings of these waveguides are Si and air, respectively, and the waveguide width and height are 0.4 μm and 0.22 μm, respectively. Figs. 6.2(a) and (b) show the electric field distributions of the Si wire waveguide for the $E^x_{11}$ mode and the $E^y_{11}$ mode, respectively. The subscript "*11*" denotes the fundamental mode. In Figs. 6.2(a) and (b), all electric field components are observed for each mode. The optical intensities of the $E_y$ component in the $E^x_{11}$ mode and the $E_x$ component in the $E^y_{11}$ mode are feeble. Figs. 6.2(c) and (d) show the electric field distributions of the Si-based plasmonic waveguide for the $E^x_{11}$ mode and the $E^y_{11}$ mode, respectively. From Fig. 6.2(c), we can see that SPP is excited by the $E_y$ component. Note that the $E_y$ component is strongly attracted to the metal surface. On the other hand, the plasmonic

mode as shown in Fig. 6.2(d) is excited by the major component ($E_y$) of the $E_{11}^y$ mode; this modal property was investigated in Ref. [30]. To distinguish from the photonic modes (Figs. 6.2(a) and (b)), in this thesis, we call the metal-assisted photonic mode shown in Fig. 6.2(c) the "i-TE mode". This mode is associated with the **mi**nor component-coupled TE mode. Additionally, we call the plasmonic mode shown in Fig. 6.2(d), which is associated with the m**a**jor component-coupled TM mode, the "a-TM mode".

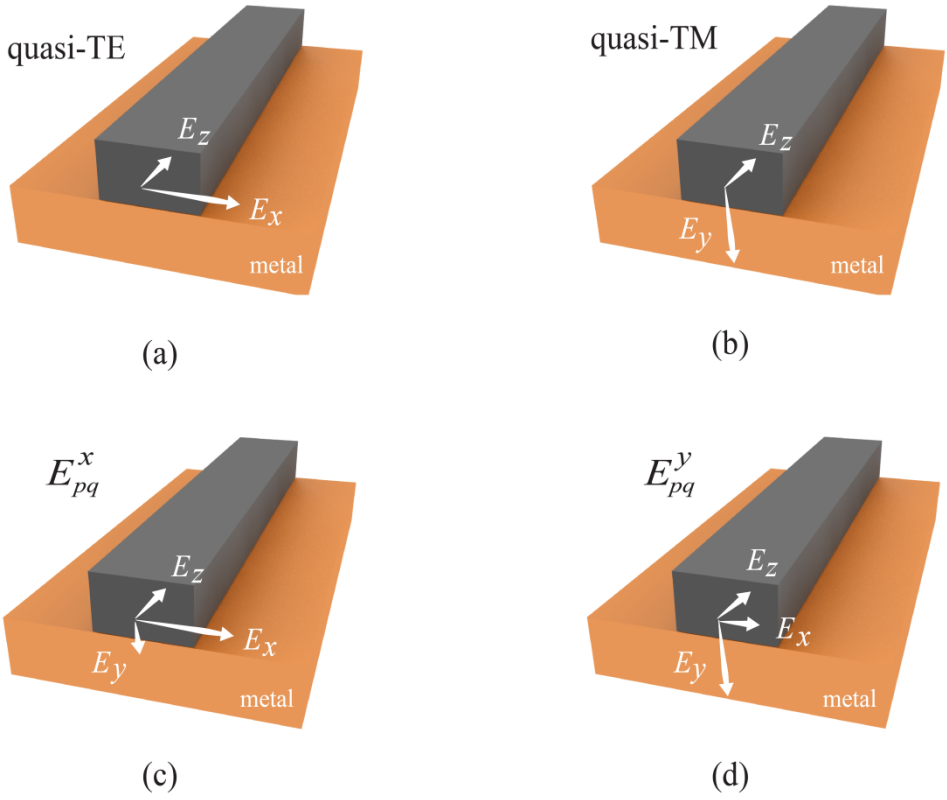


**Fig. 6.1:** Visualized definitions of (a) the quasi-TE mode, (b) the quasi-TM mode, (c) the $E_{pq}^x$ mode, and (d) the $E_{pq}^y$ mode for the electric field. Note that the magnetic field is not displayed.

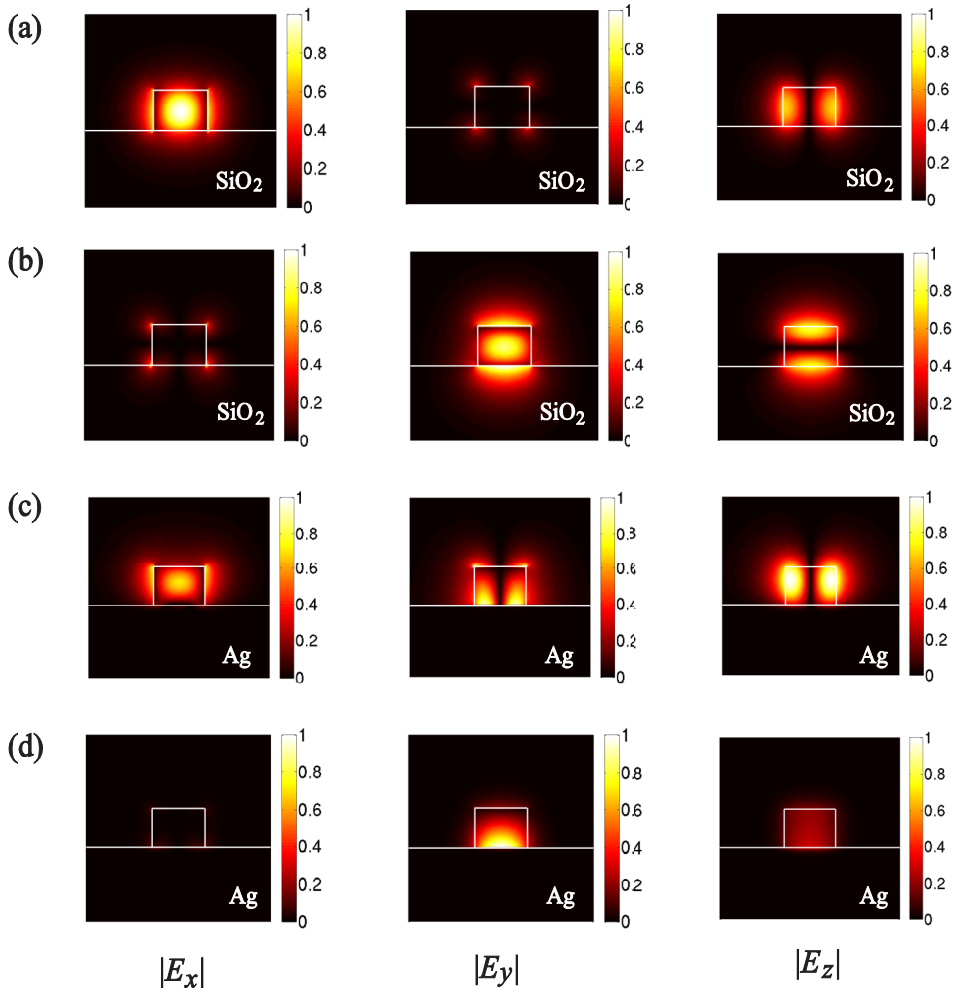


**Fig. 6.2:** The electric field distributions of the Si wire waveguide for (a) the $E_{11}^{x}$ mode and (b) the $E_{11}^{y}$ mode. Also shown are the electric field distributions of the Si-based plasmonic waveguide for (c) the $E_{11}^{x}$ mode (i-TE mode) and (d) the $E_{11}^{y}$ mode (a-TM mode). These waveguides have Si cores, and the waveguide width and height are 0.4 μm and 0.22 μm, respectively.

## 6.3 Silicon-Based Hybrid Plasmonic Waveguides

### 6.3.1 The i-TE Modes in Si-Based HPWs

Figure 6.3(a) shows a schematic of a hybrid plasmonic waveguide with a meal under cladding. The thin $SiO_2$ layer is sandwiched between Ag and Si on the SOI wafer, and the over cladding is air. We assume that the refractive indexes of Si, $SiO_2$, and Ag are 3.455, 1.445, and $0.1453 - j11.3587$ [33], respectively. The waveguide width and height are defined as $w$ and $h$, respectively, and the thickness of the $SiO_2$ layer is defined as $t$. Figures 6.3(b)-(d) show the $|E_x|$, $|E_y|$, and $|E_z|$ components of the metal-assisted photonic mode (i-TE mode) at the wavelength of 1.55 μm. We can see that SPP is excited by the $E_y$ component (minor component). Then, the $E_y$ component is in the hybrid state of the plasmonic and photonic modes. We evaluated fundamental characteristics of the i-TE mode in the Si-based HPW using the full-vector finite element method, with the wavelength set to 1.55 μm in all following simulations. We set $h$ to 0.22 μm, which is a frequently used height. Figure 6.4(a) shows the effective refractive index $n_{\text{eff}}$ of the i-TE mode as a function of the waveguide width. In the case of $w$ = 0.28 μm and $t$ = 0.15 or 0.2 μm, the i-TE modes are the radiated modes rather than the guided modes. What is the interesting here is that some effective indexes of the guided modes are not greater than 1.445 if the waveguide width is narrow. This does not apply to the case of the typical Si wire waveguide with $SiO_2$ cladding because the confined light is radiated to the under cladding region in that case. Fig. 6.4(b) shows the propagation length as a function of the waveguide width. The propagation length $L_{\text{prop}}$ is given by

$$L_{\text{prop}} = \frac{1}{|2\,\text{Im}(\beta)|}, \tag{6.1}$$

where $\beta$ is the propagation constant. From Fig. 6.4(b), we can see that the i-TE mode can achieve long-range propagations (ranging from 70 μm to over 1000 μm), which are larger than those of the plasmonic mode [35]. Additionally, we find that the propagation length increases as $t$ and $w$ become larger. Figures 6.4(c) and (d) show the effective mode area $A_{\text{eff}}$ and the confinement factor $\Gamma$ in air as a function of the waveguide width, respectively. Because the high-index-contrast waveguide has a relatively large $E_z$ component [110], we need to introduce the effective mode area and the confinement factor based on the pointing vector. Hence, the effective mode area is defined by the following equation [111]:

$$A_{\text{eff}} = \frac{\left[\iint_{\text{total}} \text{Re}\left(\boldsymbol{E} \times \boldsymbol{H}^*\right) \cdot \boldsymbol{i}_z dxdy\right]^2}{\iint_{\text{total}} \left[\text{Re}\left(\boldsymbol{E} \times \boldsymbol{H}^*\right)\right]^2 \cdot \boldsymbol{i}_z dxdy}, \tag{6.2}$$

and the confinement factor is given by the following equation [93]:

$$\Gamma = \frac{\iint_{\text{air}} \text{Re}\left( \boldsymbol{E} \times \boldsymbol{H}^* \right) \cdot \boldsymbol{i}_z dxdy}{\iint_{\text{total}} \text{Re}\left( \boldsymbol{E} \times \boldsymbol{H}^* \right) \cdot \boldsymbol{i}_z dxdy}, \tag{6.3}$$

where $\boldsymbol{E}$ and $\boldsymbol{H}$ are the electric field vector and the magnetic field vector, respectively, and * denotes the complex conjugate. From Figs. 6.4(c) and (d), it is clear that the effective mode area and the confinement factor both increase as the waveguide width becomes narrower. This means that the confinement in the silicon core is weak when the waveguide width is narrower.

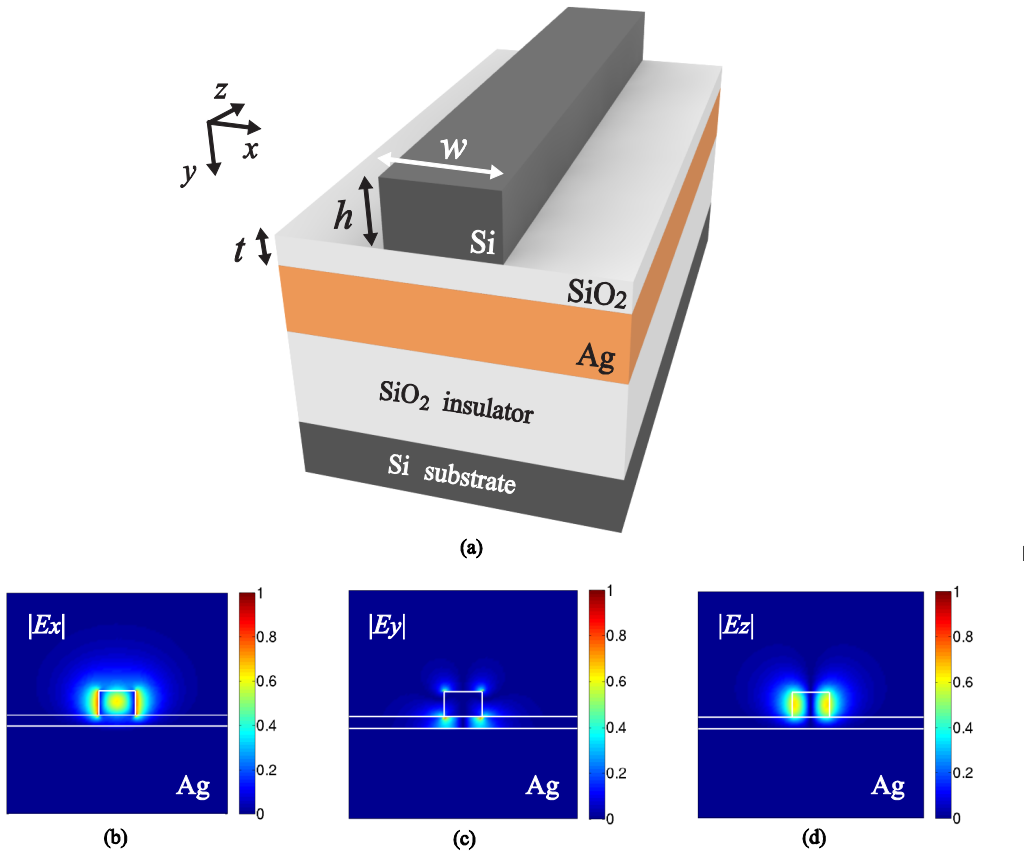


**Fig. 6.3:** (a) Schematic of a hybrid plasmonic waveguide with a metal under cladding, and (b) $|E_x|$, (c) $|E_y|$, and (d) $|E_z|$ of the i-TE mode at the wavelength of 1.55 μm.

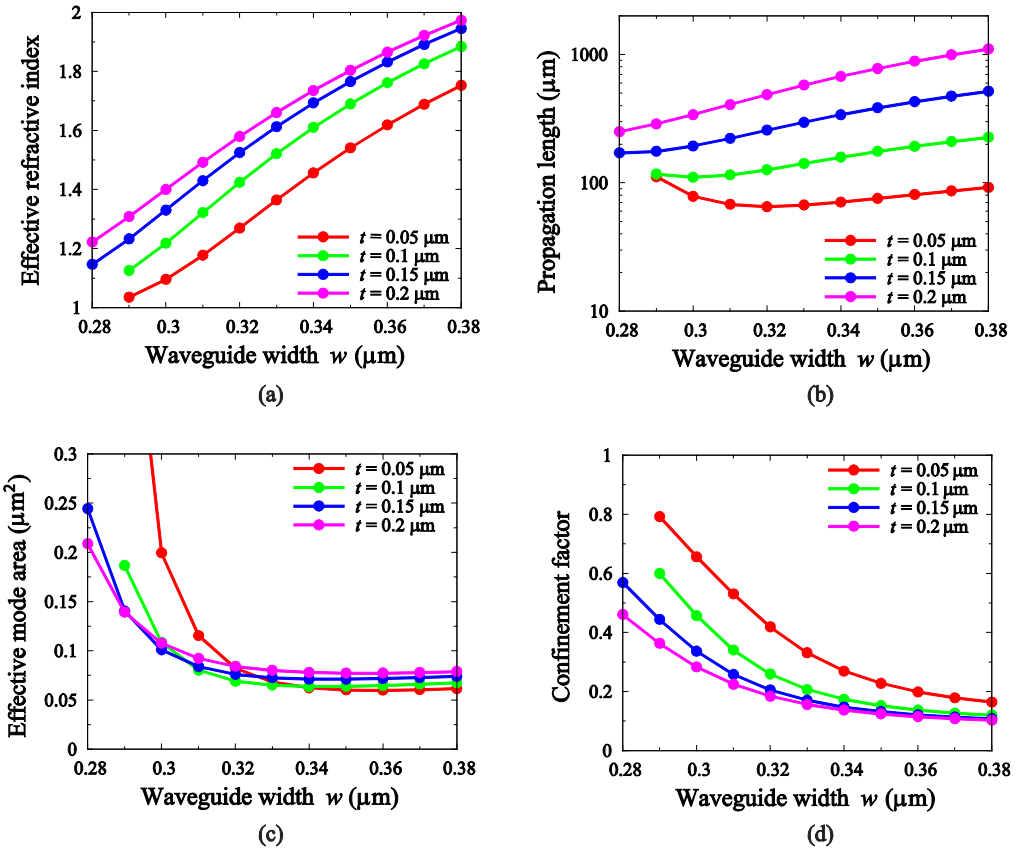


**Fig. 6.4:** (a) The effective refractive index, (b) the propagation length, (c) the effective mode area, and (d) the confinement factor as a function of the waveguide width $w$ when $h$ = 0.22 μm.

### 6.3.2 Bending and Coupling Characteristics

To verify the usefulness of the i-TE mode in the Si-based HPW, we estimate the device length of a 3-dB coupler, as shown in Fig. 6.5. The 3-dB coupler is composed of bending regions (90° bend) and a coupling region. The bending radius, the length of the coupling region, and the waveguide distance are defined as *R*, *L*, and *d*, respectively. Typically, since there exists a trade-off between the bending loss and the coupling length, we need to estimate the degree of integrations considering not only the bending but also the coupling. If the effective refractive index is large, a strong bend can be achieved. On the other hand, if the effective refractive index is small, the coupling length becomes short because the coupling length is determined by the overlap of the evanescent fields in two parallel waveguides. As the a-TM mode tends to be confined in a dielectric region, it is easy to enlarge the effective refractive index compared with the i-TE mode. However, it does not overcome the limitation of the trade-off relation. For the i-TE mode, a high effective refractive index is also obtained by tuning waveguide dimensions. Since the limitation of the integration is determined by the refractive index contrast of materials, we perform a comparison between the i-TE mode in the Si-based HPW and the TE-like mode in the Si wire waveguide.

First, we evaluated bending and coupling characteristics of the 3-dB coupler based on the Si-based HPW. As an example, we choose a waveguide distance *d* of 0.3 μm. Fig. 6.6(a) shows the coupling length $L_c$ as a function of the waveguide width *w* when *d* = 0.3 μm and *h* = 0.22 μm. The coupling length $L_c$ is given by

$$L_c = \frac{\lambda}{2(n_{\mathrm{eff}\,0} - n_{\mathrm{eff}\,1})}, \tag{6.4}$$

where $n_{\mathrm{eff}0}$ and $n_{\mathrm{eff}1}$ are the effective refractive indexes of the fundamental supermode and the first order supermode, respectively, and $\lambda$ is the operating wavelength. Note that *L* is equal to $L_c/2$ in the 3-dB coupler case. From Fig. 6.6(a), we can see that the coupling length becomes shorter as *w* decreases. Also note that almost the same coupling length is obtained even if *t* changes. Figs. 6.6(b)-(d) show the bending loss of the 90° bend as a function of the bending radius *R* when *t* = 0.05 μm, *t* = 0.1 μm, and *t* = 0.15 μm, respectively. When conducting on the bending analysis based on the VFEM [95], a total loss is outputted. Specifically, the total loss includes both the absorption loss due to metal and the bending loss. To extract the bending loss of the 90° bend, we subtract the loss in the straight condition (Fig. 6.4(b)) from the total loss obtained by the bending analysis [37]. Thus, the bending loss of the 90° bend can be calculated by

$$\textit{Bending loss}\,(\mathrm{dB}/90^\circ) = \frac{\pi R}{2}[\,\textit{total loss}\,(\mathrm{dB/\mu m}) - \textit{metallic loss}\,(\mathrm{dB/\mu m})\,]. \tag{6.5}$$

From Figs. 6.6(b)-(d), we find that a smaller *t* tends to result in reduction of the bending loss. Additionally, when we focus on a certain *t*, a strong bending can be achieved by selecting a larger *w* that remains proportional to the effective refractive index. Here, we estimate the

length of the Si HPW-based 3-dB coupler ($4R+L$). Dimensions of the HPW and $R$ are determined based on the presupposition that the bending loss is 0.01 dB/90°, and then the corresponding $L$ is given. Considering all combinations of $R$ and $L$, the shortest 3-dB coupler length ($4R+L$) of 14 μm is obtained when $t$ = 0.1 μm and $w$ = 0.33 μm ($L_{prop}$ = 142 μm). Here, the calculated total loss of the 3-dB coupler based on the HPW is about 0.6 dB when assuming that the loss of the coupling region is the same as the single straight waveguide. This low loss propagation is due to the use of the metal-assisted photonic mode. Additionally, the loss can be compensated by introducing gain materials to the low-index material or Si core [107].

Next, we estimate the length of the 3-dB coupler based on the Si wire waveguide to compare with the device length of the Si HPW-based 3-dB coupler. Fig. 6.7(a) shows a schematic of a Si wire waveguide, where $w_{si}$ and $h_{si}$ are the waveguide width and the waveguide height, respectively. The refractive indexes of Si and $SiO_2$ are the same as in the case of the HPW. We set $h_{si}$ to 0.22 μm, which is a frequently used height. Figs. 6.7(b) and (c) show the effective refractive index and the coupling length when $d$ = 0.3 μm as a function of $w_{si}$, respectively. From these figures, we can see that the coupling length is related to the effective refractive index similar to the coupling characteristics of the Si-based HPW. Theoretically, the coupling length is determined by the overlap of the evanescent fields in two parallel waveguides. To obtain a large overlap of the evanescent fields, we need to select a structure that has a low effective refractive index. Fig. 6.7(d) shows the bending loss of the Si wire waveguide with respect to the bending radius. We find that a larger $w_{si}$ leads to reduction of the bending loss. The estimated lengths of the 3-dB coupler based on the Si wire waveguide are summarized in Table 6.1. The shortest device length for the Si wire waveguide is 21.8 μm, corresponding to $w_{si}$ = 0.36 μm. According to the above results, the length of the 3-dB coupler based on the HPW is two-thirds that of the coupler based on the Si wire waveguide. By using the i-TE mode in the Si-based HPW, the high-index contrast can be realized even in the under cladding direction. In other words, the radiation from the core to the under cladding is effectively suppressed. Therefore, because the bending loss can be reduced in a structure that has a small coupling length, it is shown that a shorter 3-dB coupler length is obtained with the Si-based HPW than the Si wire waveguide.

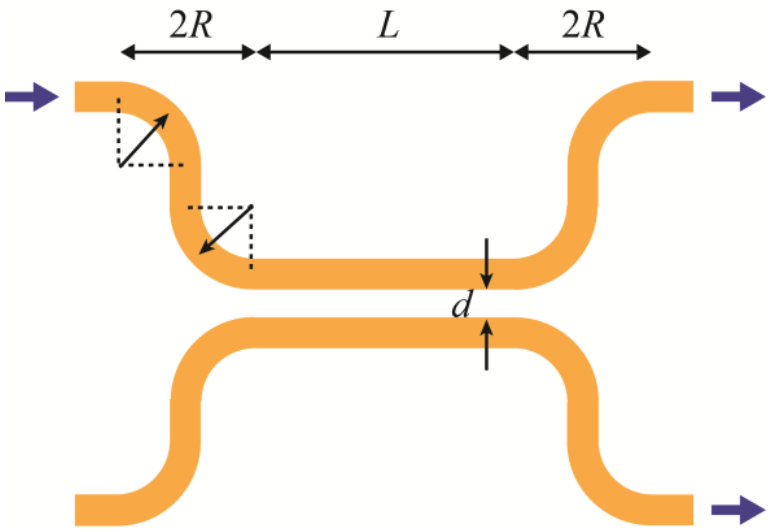


**Fig. 6.5:** Schematic of a 3-dB coupler, where *R*, *L*, and *d* are the bending radius, the length of the coupling region, and the waveguide distance, respectively. The total device length is given by 4*R*+*L* (μm).

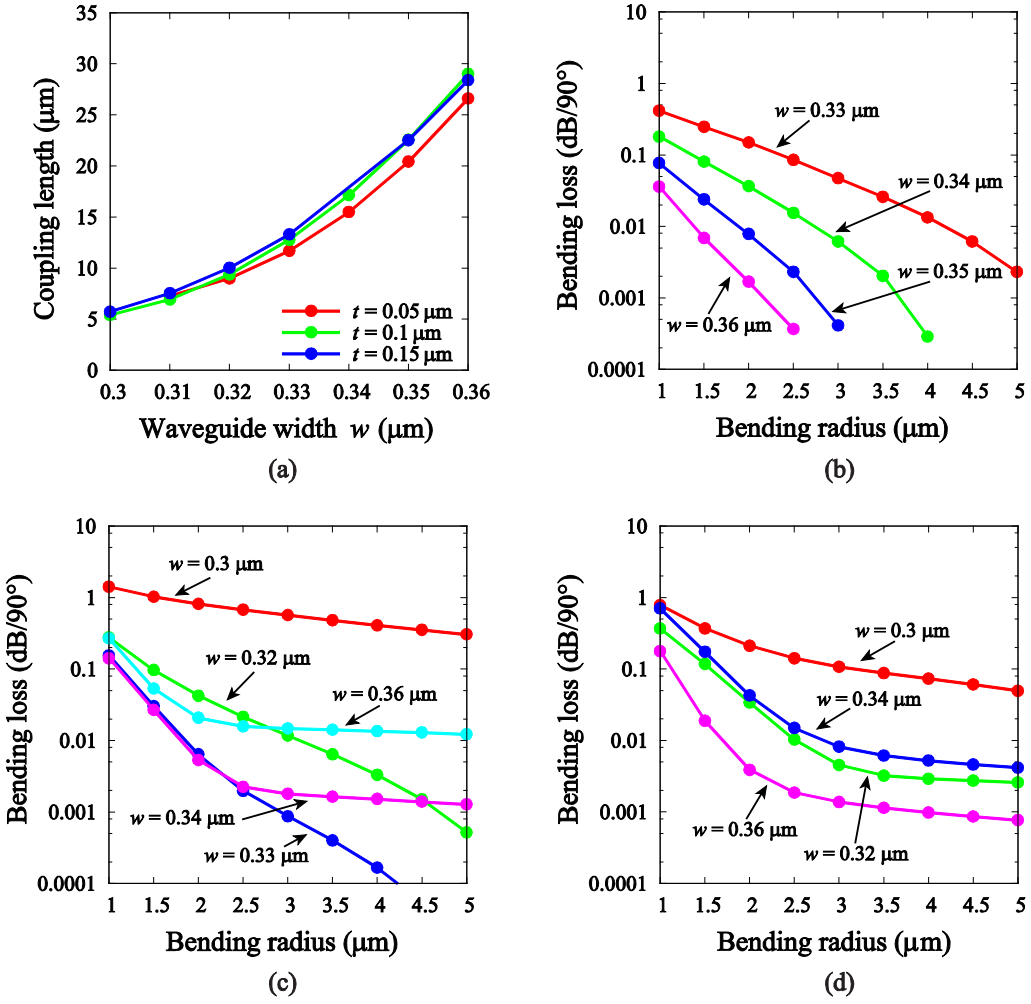


**Fig. 6.6:** (a) The coupling length as a function of $w$ in the case of $d$ = 0.3 μm, and the bending loss of the 90° bend with respect to the bending radius when (b) $t$ = 0.05 μm, (c) $t$ = 0.1 μm, and (d) $t$ = 0.15 μm ($h$ = 0.22 μm).

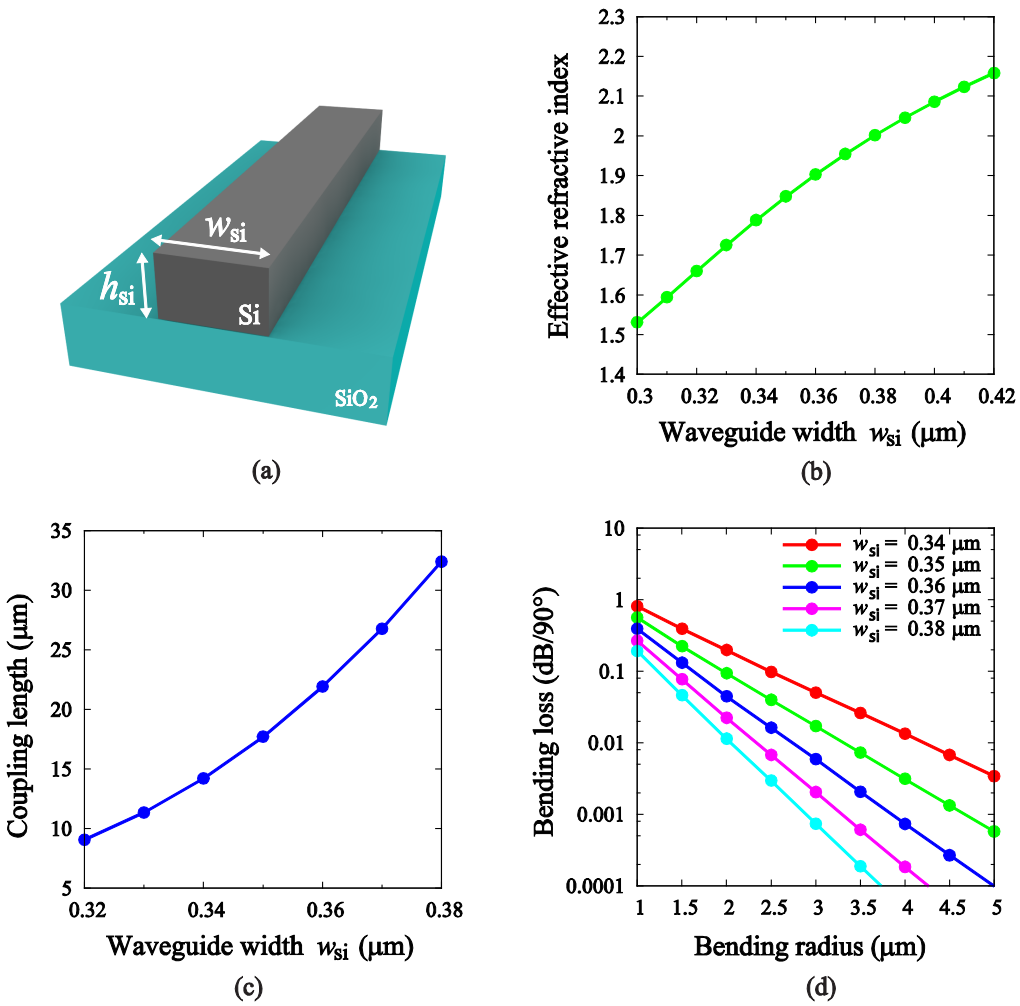


**Fig. 6.7:** (a) Schematic of a Si wire waveguide, (b) the effective refractive index as a function of $w_{Si}$, (c) the coupling length as a function of $w_{Si}$ when $d$ = 0.3 μm, and (d) the bending loss of the 90° bend with respect to the bending radius.

**Table 6.1:** Estimated length of the 3-dB coupler based on the Si wire waveguide.

| $w_{Si}$ (μm) | $L$ (μm) | $R$ (μm) when the bending loss is 0.01 dB/90° | Total 3-dB coupler length $L$+4$R$ (μm) |
|---|---|---|---|
| 0.34 | 7.1 | 4.2 | 23.9 |
| 0.35 | 8.9 | 3.3 | 22.1 |
| 0.36 | 11 | 2.7 | 21.8 |
| 0.37 | 13.4 | 2.3 | 22.6 |
| 0.38 | 16.2 | 2.1 | 24.6 |

## 6.4 Metal-Assisted Silicon Slot Waveguides

Fig. 6.8 shows a schematic of a metal-assisted silicon slot waveguide. The thin $SiO_2$ layer is sandwiched between Ag and silicon slot waveguide, and the over cladding is filled by acetylene gas. We assume that the refractive indexes of Si, $SiO_2$, acetylene gas, and Ag are 3.455, 1.445, 1.000593 [112], and $0.1453 - j11.3587$, respectively. The Si-width, slot width, and waveguide height are defined as $w_h$, $w_s$, and $h$, respectively. The thickness of $SiO_2$ layer is defined as $t$. Fig. 6.9 shows the electric field distribution of the i-TE mode in the metal-assisted silicon slot waveguide ($w_h$ = 0.29 μm, $w_s$ = 0.1 μm, $h$ = 0.22 μm, $t$ = 0.05 μm) at the wavelength of 1.55 μm. We can see that SPP is excited by the $E_y$ component (minor component).

Since the optical waveguide sensitivity is proportional to the confinement factor [86], a large optical confinement in the over cladding leads to improvement of the sensor sensitivity. When the confinement factor is large, the effective refractive index is strongly affected by the concentration change of the cover medium such as aqueous solution or gas [85]. If the effective refractive index is changed, for example, resonant wavelength of ring resonators is also changed, which returns the concentration change of aqueous solution or gas. Fig. 6.10(a) shows the effective refractive index $n_{eff}$ of the metal-assisted silicon slot waveguide and a conventional slot waveguide with a $SiO_2$ under cladding as a function of the Si-width $w_h$. We can see that the effective refractive index increases as the Si-width of the slot waveguides becomes larger. Note that guided modes of the conventional slot waveguide are radiated to the $SiO_2$ under cladding when $n_{eff}$ is not greater than 1.445. Fig. 6.10(b) shows the confinement factor in the gas region of both slot waveguides as a function of the Si-width. The confinement factor in the gas region $\Gamma_{gas}$ is given by the following equation:

$$\Gamma_{gas} = \frac{\iint_{gas} \mathrm{Re}\left( \boldsymbol{E} \times \boldsymbol{H}^* \right) \cdot \boldsymbol{i}_z dxdy}{\iint_{total} \mathrm{Re}\left( \boldsymbol{E} \times \boldsymbol{H}^* \right) \cdot \boldsymbol{i}_z dxdy}, \tag{6.6}$$

where $\boldsymbol{E}$ and $\boldsymbol{H}$ are the electric field vector and the magnetic field vector, respectively, and $^*$ denotes the complex conjugate. The confinement factor of the metal-assisted silicon slot waveguide is larger than that of the conventional slot waveguide. Fig. 6.11 shows the propagation length as a function of the Si-width.

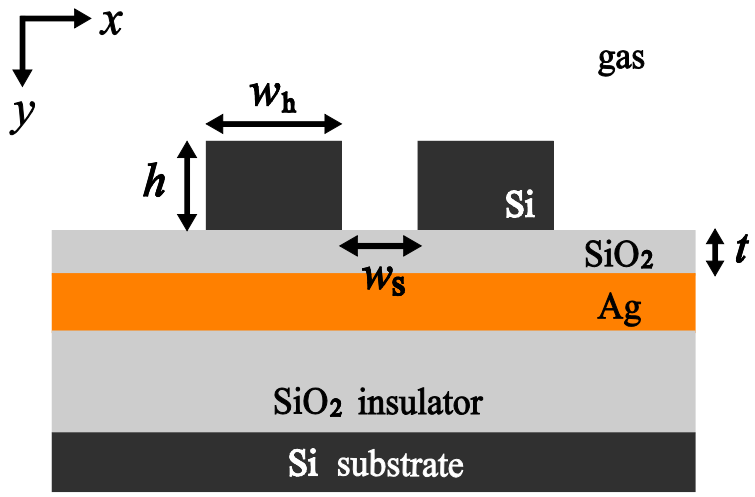


**Fig. 6.8:** Schematic of a metal-assisted silicon slot waveguide. The over cladding is filled by acetylene gas.

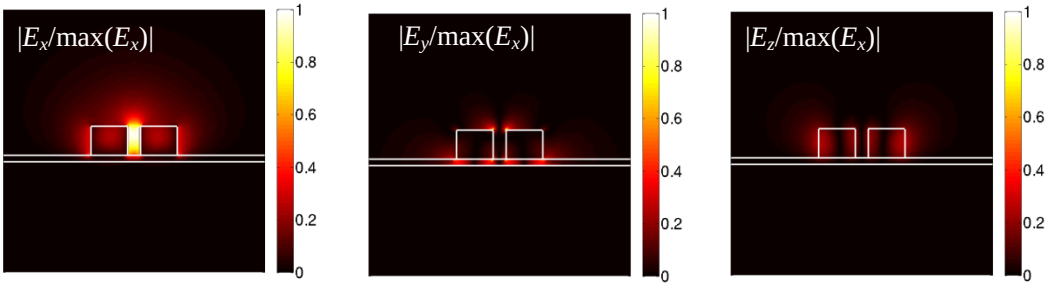


**Fig. 6.9:** The electric field distribution of the i-TE mode in the metal-assisted silicon slot waveguide ($w_h$ = 0.29 μm, $w_s$ = 0.1 μm, $h$ = 0.22 μm, $t$ = 0.05 μm) at the wavelength of 1.55 μm.

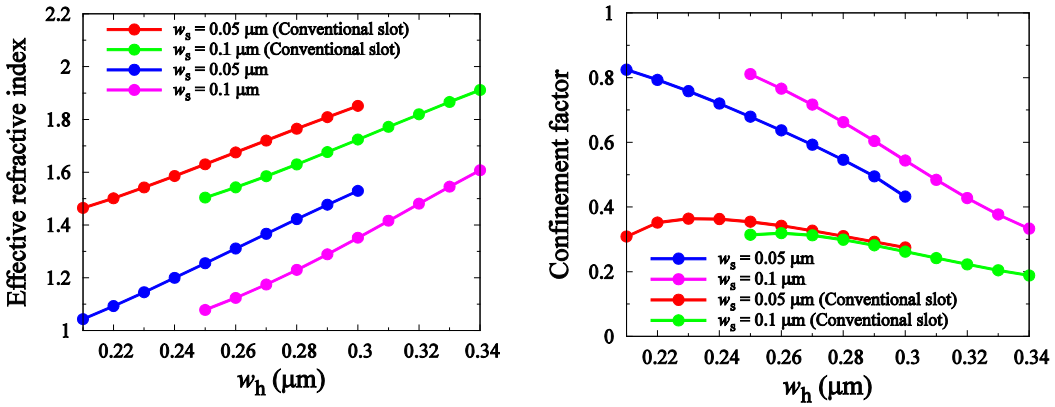


(a) (b)

**Fig. 6.10:** (a) The effective refractive index and (b) the confinement factor in the gas region as a function of the Si-width $w_h$. These characteristics of a conventional silicon slot waveguide with a $SiO_2$ under cladding are also evaluated for comparison.

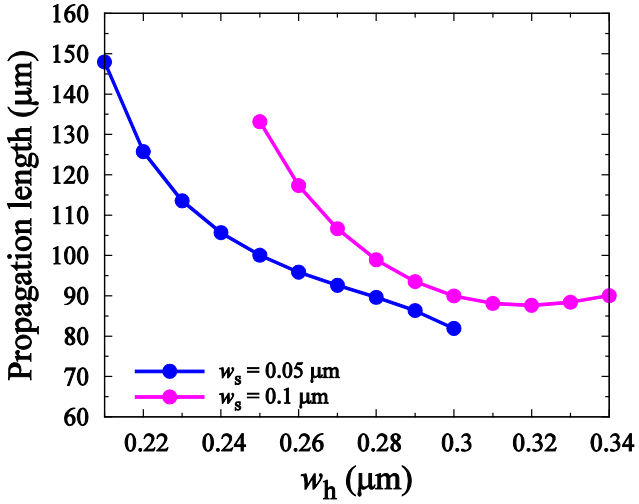


**Fig. 6.11:** The propagation length as a function of the Si-width $w_h$.

# Chapter 7

# Summary

First, we have presented a novel design method of optical XOR, XNOR, NAND, and OR logic gates with coherent detection for binary-phase-shift-keyed (BPSK) signal processing devices. The devices are composed of multi-mode interference waveguides and convert the phase information of the input signal to amplitude at the output. We have applied the finite element method for numerical simulations, and the evaluated least ON to OFF logic-level contrast ratios for the XOR, XNOR, NAND, and OR logic gates are 21.5 dB, 21.5 dB, 22.3 dB, and 22.3 dB, respectively. The proposed logic gates are extremely promising signal processing devices for BPSK signals in packet switching systems.

Second, a three-dimensional (3-D) vector finite element method (VFEM) for waveguide discontinuity problem has been newly formulated and implemented. Through the use of the 3-D VFEM, transmission characteristics of two types of crossing slot-waveguides with finite core-height have been investigated. One is a direct crossing and the other is a crossing filling up the slots locally. Results have shown that 3-D analysis considering the finite core height is indispensable.

Third, we have presented a transmission-efficient bent silicon slot waveguide and crossing silicon slot waveguide for compact silicon slot waveguide-based circuits. We have investigated, using the 3-D VFEM, the transmission characteristics of a bent silicon slot waveguide with an asymmetric slot that is connected to straight waveguides. Numerical results have shown that the transmission efficiency can be improved by optimizing a taper structure that is introduced between an asymmetric slot waveguide and its straight input/output waveguides. Next, we have proposed a 3-D crossing silicon slot waveguide that has a vertical coupler and have investigated its transmission characteristics. Numerical results have shown that the proposed crossing structure can achieve a high transmission efficiency compared with conventional structures.

Finally, we have revealed that the minor electric field component of the metal-assisted photonic mode in hybrid plasmonic waveguides (HPWs) contributes to the excitation of surface plasmon polariton (SPP). In addition, we have investigated modal properties, and bending and coupling characteristics of the metal-assisted photonic mode in a Si-based HPW.

# Acknowledgements

I would like to express my deepest gratitude to my dissertation advisor, Professor Kunimasa Saitoh, for his outstanding guidance, caring, and patience, and for providing me with an excellent atmosphere for conducting research. Without his encouragement, this paper would not have materialized. I would also like to express great thanks to my co-advisors, Professor Yoshikazu Miyanaga, Professor (specially appointed) Toshio Nojima, and Professor (specially appointed) Yasutaka Ogawa, for their encouragement and comments, which were invaluable.

My heartfelt application goes to Dr. Masanori Koshiba, who has provided constructive comments and warm encouragement. I also owe my gratitude to Associate Professor Takeshi Fujisawa, whose meticulous comments were an enormous help to me.

I would like to thank Dr. Lorenzo Rosa, Dr. Yuki Kawaguchi, Dr. Masa-aki Komatsu, Shuntaro Makino, Takui Uematsu, Masaru Nagai, Tetsuya Kitayama, Takanori Sato and the other members of our laboratory team for their valuable discussions and for making my time spent in the lab enjoyable. I would also like to thank my cram school English teacher, Yoko Ishibashi, for her warm support.

I offer deep gratitude to my parents, Akihiro and Michiko, and my younger brother, Fumiya. They have always provided heartfelt support and encouragement.

Finally, I owe many thanks to Marie Katsurai. For eight years she was always been available for discussions and teaching, to cheer me up, and to spend enjoyable time with me.

March 2014
Yuhei Ishizaka

# References


[1] D. K. Hunter, and I. Andonovic, “Approaches to optical Internet packet switching,” *IEEE Communications Magazine*, vol. 38, no. 9, pp. 116-122, Sep. 2000.

[2] D. J. Blumenthal, B. E. Olsson, G. Rossi, T. E. Dimmick, L. Ran, M. Masanovi, O. Lavrova, R. Doshi, O. Jerphagnon, J. E. Bowers, V. Kaman, L. A. Coldren, and J. Barton, “All-optical label swapping networks and technologies,” *Journal of Lightwave Technology*, vol. 18, no. 12, pp. 2058-2075, Dec. 2000.

[3] R. Clavero, J. M. Martinez, F. Ramos, and J. Marti, “All-optical packet routing scheme for optical label-swapping networks,” *Optics Express*, vol. 12, no. 18, pp. 4326-4332, Sep. 2004.

[4] V. Van, T. A. Ibrahim, P. P. Absil, F. G. Johnson, R. Grover, and P. T. Ho, “Optical signal processing using nonlinear semiconductor microring resonators,” *IEEE Journal of Selected Topics in Quantum Electronics*, vol. 8, no. 3, pp. 705-713, May-Jun. 2002.

[5] Z. J. Li, Z. W. Chen, and B. J. Li, “Optical pulse controlled all-optical logic gates in SiGe/Si multimode interference,” *Optics Express*, vol. 13, no. 3, pp. 1033-1038, Feb. 2005.

[6] Z. H. Zhu, W. M. Ye, J. R. Ji, X. D. Yuan, and C. Zen, “High-contrast light-by-light switching and AND gate based on nonlinear photonic crystals,” *Optics Express*, vol. 14, no. 5, pp. 1783-1788, Mar. 2006.

[7] T. Fujisawa, and M. Koshiba, “All-optical logic gates based on nonlinear slot-waveguide couplers,” *Journal of the Optical Society of America B*, vol. 23, no. 4, pp. 684-691, Apr. 2006.

[8] Z. H. Li, and G. F. Li, “Ultrahigh-speed reconfigurable logic gates based on four-wave mixing in a semiconductor optical amplifier,” *IEEE Photonics Technology Letters*, vol. 18, no. 9-12, pp. 1341-1343, May-Jun. 2006.

[9] Y. Zhang, Y. Zhang, and B. Li, “Optical switches and logic gates based on self-collimated beams in two-dimensional photonic crystals,” *Optics Express*, vol. 15, no. 15, pp. 9287-9292, Jul. 2007.

[10] Y.-D. Wu, T.-T. Shih, and M.-H. Chen, “New all-optical logic gates based on the local nonlinear Mach-Zehnder interferometer,” *Optics Express*, vol. 16, no. 1, pp. 248-257, Jan. 2008.

[11] Q. Liu, Z. Ouyang, C. J. Wu, C. P. Liu, and J. C. Wang, “All-optical half adder based on cross structures in two-dimensional photonic crystals,” *Optics Express*, vol. 16, no. 23, pp. 18992-19000, Nov. 2008.

[12] P. Andalib, and N. Granpayeh, “All-optical ultracompact photonic crystal AND gate based on nonlinear ring resonators,” *Journal of the Optical Society of America B*, vol. 26, no. 1, pp. 10-16, Jan. 2009.

[13] B. M. Isfahani, T. A. Tameh, N. Granpayeh, and A. R. M. Javan, “All-optical NOR gate based on nonlinear photonic crystal microring resonators,” *Journal of the Optical Society of America B*, vol. 26, no. 5, pp. 1097-1102, May 2009.

[14] J. Bai, J. Wang, J. Jiang, X. Chen, H. Li, Y. Qiu, and Z. Qiang, “Photonic NOT and NOR gates based on a single compact photonic crystal ring resonator,” *Applied Optics*, vol. 48, no. 36, pp. 6923-6927, Dec. 2009.

[15] S. Zeng, Y. Zhang, B. Li, and E. Y.-B. Pun, “Ultrasmall optical logic gates based on silicon periodic dielectric waveguides,” *Photonics and Nanostructures-Fundamentals and Applications*, vol. 8, no. 1, pp. 32-37, Jan. 2010.

[16] N. Deng, K. Chan, C.-K. Chan, and L.-K. Chen, “An all-optical, XOR logic gate for high-speed RZ-DPSK signals by FWM in semiconductor optical amplifier,” *IEEE Journal of Selected Topics in Quantum Electronics*, vol. 12, no. 4, pp. 702-707, Jul.-Aug. 2006.

[17] J. Xu, X. Zhang, Y. Zhang, J. Dong, D. Liu, and D. Huang, “Reconfigurable all-optical logic gates for multi-input differential phase-shift keying signals: Design and experiments,” *Journal of Lightwave Technology*, vol. 27, no. 23, pp. 5268-5275, Dec. 2009.

[18] J. Wang, J. Sun, X. Zhang, D. Huang, and M. M. Fejer, “Ultrafast all-optical three-input Boolean XOR operation for differential phase-shift keying signals using periodically poled lithium niobate,” *Optics Letters*, vol. 33, no. 13, pp. 1419-1421, Jul. 2008.

[19] V. R. Almeida, Q. F. Xu, C. A. Barrios, and M. Lipson, “Guiding and confining light in void nanostructure,” *Optics Letters*, vol. 29, no. 11, pp. 1209-1211, Jun. 2004.

[20] Q. F. Xu, V. R. Almeida, R. R. Panepucci, and M. Lipson, “Experimental demonstration of guiding and confining light in nanometer-size low-refractive-index material,” *Optics Letters*, vol. 29, no. 14, pp. 1626-1628, Jul. 2004.

[21] J.-M. Lee, D.-J. Kim, G.-H. Kim, O. K. Kwon, K.-J. Kim, and G. Kim, “Controlling temperature dependence of silicon waveguide using slot structure,” *Optics Express*, vol. 16, no. 3, pp. 1645-1652, Feb. 2008.

[22] A. Yuki, I. Keita, N. Nobuhiko, and A. Shigehisa, “Athermal wavelength characteristics of Si slot ring resonator embedded with Benzocyclobutene for optoelectronic integrated circuits,” *Japanese Journal of Applied Physics*, vol. 49, no. 5, May 2010.

[23] R. Su, D. Tang, W. Ding, L. Chen, and Z. Zhou, “Efficient transmission of crossing dielectric slot waveguides,” *Optics Express*, vol. 19, no. 5, pp. 4756-4761, Feb. 2011.

[24] R. Zia, M. D. Selker, P. B. Catrysse, and M. L. Brongersma, “Geometries and materials for subwavelength surface plasmon modes,” *Journal of the Optical Society of America A*, vol. 21, no. 12, pp. 2442-2446, May 2004.

[25] J. A. Dionne, L. A. Sweatlock, H. A. Atwater, and A. Polman, “Plasmon slot waveguides: Towards chip-scale propagation with subwavelength-scale localization,” *Physical Review B*, vol. 73, no. 3, 2006.

[26] D. F. P. Pile, and D. K. Gramotnev, “Channel plasmon-polariton in atriangular groove on a metal surface,” *Optics Letters*, vol. 29, no. 10, pp. 1069-1071, May 2004.

[27] S. I. Bozhevolnyi, and J. Jung, “Scaling for gap plasmon based waveguides,” *Optics Express*, vol. 16, no. 4, pp. 2676-2684, Feb. 2008.

[28] T. Holmgaard, and S. I. Bozhevolnyi, “Theoretical analysis of dielectric-loaded surface plasmon-polariton waveguides,” *Physical Review B*, vol. 75, no. 24, Jun. 2007.

[29] J. Grandidier, G. C. D. Francs, S. Massenot, A. Bouhelier, L. Markey, J. C. Weeber, C. Finot, and A. Dereux, “Gain-assisted propagation in a plasmonic waveguide at telecom wavelength,” *Nano Letters*, vol. 9, no. 8, pp. 2935-2939, Aug. 2009.

[30] A. V. Krasavin, and A. V. Zayats, “Silicon-based plasmonic waveguides,” *Optics Express*, vol. 18, no. 11, pp. 11791-11799, May 2010.

[31] R. F. Oulton, V. J. Sorger, D. A. Genov, D. F. P. Pile, and X. Zhang, “A hybrid plasmonic waveguide for subwavelength confinement and long-range propagation,” *Nature Photonics*, vol. 2, no. 8, pp. 496-500, Aug. 2008.

[32] S. Y. Zhu, T. Y. Liow, G. Q. Lo, and D. L. Kwong, “Silicon-based horizontal nanoplasmonic slot waveguides for on-chip integration,” *Optics Express*, vol. 19, no. 9, pp. 8888-8902, Apr. 2011.

[33] D. Dai, and S. L. He, “A silicon-based hybrid plasmonic waveguide with a metal cap for a nano-scale light confinement,” *Optics Express*, vol. 17, no. 19, pp. 16646-16653, Sep. 2009.

[34] M. Z. Alam, J. Meier, J. S. Aitchison, and M. Mojahedi, “Propagation characteristics of hybrid modes supported by metal-low-high index waveguides and bends,” *Optics Express*, vol. 18, no. 12, pp. 12971-12979, Jun. 2010.

[35] H. S. Chu, E. P. Li, P. Bai, and R. Hegde, “Optical performance of single-mode hybrid dielectric-loaded plasmonic waveguide-based components,” *Applied Physics Letters*, vol. 96, no. 22, May 2010.

[36] H. S. Chu, Y. Akimov, P. Bai, and E. P. Li, “Submicrometer radius and highly confined plasmonic ring resonator filters based on hybrid metal-oxide-semiconductor waveguide,” *Optics Letters*, vol. 37, no. 21, pp. 4564-4566, Nov. 2012.

[37] C. Y. Yang, E. J. Teo, T. Goh, S. L. Teo, J. H. Teng, and A. A. Bettiol, “Metal-assisted photonic mode for ultrasmall bending with long propagation length at visible wavelengths,” *Optics Express*, vol. 20, no. 21, pp. 23898-23905, Oct. 2012.

[38] M. A. Sefunc, M. Pollnau, and S. M. García-Blanco, “Low-loss sharp bends in polymer waveguides enabled by the introduction of a thin metal layer,” *Optics Express*, vol. 21, no. 24, pp. 29808-29817, Dec. 2013.

[39] K. Saitoh, and M. Koshiba, “Full-vectorial imaginary-distance beam propagation method based on a finite element scheme: Application to photonic crystal fibers,” *IEEE Journal of Quantum Electronics*, vol. 38, no. 7, pp. 927-933, Jul. 2002.

[40] Y. Tsuji, and M. Koshiba, “Finite element method using port truncation by perfectly matched layer boundary conditions for optical waveguide discontinuity problems,” *Journal of Lightwave Technology*, vol. 20, no. 3, pp. 463-468, Mar. 2002.

[41] F. L. Teixeira, and W. C. Chew, “General closed-form PML constitutive tensors to match arbitrary bianisotropic and dispersive linear media,” *IEEE Microwave and Guided Wave Letters*, vol. 8, no. 6, pp. 223-225, Jun. 1998.

[42] M. Koshiba, and Y. Tsuji, “Curvilinear hybrid edge/nodal elements with triangular shape for guided-wave problems,” *Journal of Lightwave Technology*, vol. 18, no. 5, pp. 737-743, May 2000.

[43] Z. Min, W. Ling, and P. Ye, “All optical XOR logic gates: technologies and experiment demonstrations,” *IEEE Communications Magazine*, vol. 43, no. 5, pp. S19-S24. 2005.

[44] Z. Zalevsky, A. Rudnitsky, and M. Nathan, “Nano photonic and ultra fast all-optical processing modules,” *Optics Express*, vol. 13, no. 25, pp. 10272-10284, Dec. 2005.

[45] R. Vilar, J. M. Martinez, F. Ramos, and J. Marti, “All-optical decrementing of a packet's time-to-live (TTL) field using logic XOR gates,” *Optics Express*, vol. 16, no. 24, pp. 19734-19740, Nov. 2008.

[46] K. Mishina, A. Maruta, S. Mitani, T. Miyahara, K. Ishida, K. Shimizu, T. Hatta, K. Motoshima, and K.-i. Kitayama, “NRZ-OOK-to-RZ-BPSK modulation-format conversion using SOA-MZI wavelength converter,” *Journal of Lightwave Technology*, vol. 24, no. 10, pp. 3751-3758, Oct. 2006.

[47] Z. Liu, S. Xiao, L. Cai, and Z. Liang, “Multi-format receiver for non-return-to-zero binary-phase-shift-keyed and non-return-to-zero amplitude-shit-keyed signals,” *Optics Express*, vol. 17, no. 4, pp. 2918-2925, Feb. 2009.

[48] A. H. Gnauck, S. Chandrasekhar, J. Leuthold, and L. Stulz, “Demonstration of 42.7-Gb/s DPSK receiver with 45 photons/bit sensitivity,” *IEEE Photonics Technology Letters*, vol. 15, no. 1, pp. 99-101, Jan. 2003.

[49] A. H. Gnauck, G. Raybon, S. Chandrasekhar, J. Leuthold, C. Doerr, L. Stulz, and E. Burrows, “25 x 40-gb/s copolarized DPSK transmission over 12 x 100-km NZDF with 50-GHz,” *IEEE Photonics Technology Letters*, vol. 15, no. 3, pp. 467-469, Mar. 2003.

[50] T. Mizuochi, K. Ishida, T. Kobayashi, J. Abe, K. Kinjo, K. Motoshima, and K. Kasahara, “A comparative study of DPSK and OOKWDM transmission over transoceanic distances and their performance degradations due to nonlinear phase noise,” *Journal of Lightwave Technology*, vol. 21, no. 9, pp. 1933-1943, Sep. 2003.

[51] M. L. Gilmore, F. R. Steel, and J. A. Tempka, *Digital detection system for differential phase shift keyed signals*,to Google Patents, 1976.

[52] C. Xu, X. Liu, and X. Wei, “Differential phase-shift keying for high spectral efficiency optical transmissions,” *IEEE Journal of Selected Topics in Quantum Electronics*, vol. 10, no. 2, pp. 281-293, Mar.-Apr. 2004.

[53] A. H. Gnauck, and P. J. Winzer, “Optical phase-shift-keyed transmission,” *Journal of Lightwave Technology*, vol. 23, no. 1, pp. 115-130, Jan. 2005.

[54] E. Ip, A. P. T. Lau, D. J. F. Barros, and J. M. Kahn, “Coherent detection in optical fiber systems,” *Optics Express*, vol. 16, no. 2, pp. 753-791, Jan. 2008.

[55] V. Ferrero, and S. Camatel, “Optical phase locking techniques: an overview and a novel method based on Single Side Sub-Carrier modulation,” *Optics Express*, vol. 16, no. 2, pp. 818-828, Jan. 2008.

[56] M. J. Fice, A. Chiuchiarelli, E. Ciaramella, and A. J. Seeds, “Homodyne coherent optical receiver using an optical injection phase-lock loop,” *Lightwave Technology, Journal of*, vol. 29, no. 8, pp. 1152-1164. Apr. 2011.

[57] J. M. Kahn, and K. P. Ho, “Spectral efficiency limits and modulation/detection techniques for DWDM systems,” *IEEE Journal of Selected Topics in Quantum Electronics*, vol. 10, no. 2, pp. 259-272, Mar.-Apr. 2004.

[58] P. A. Besse, M. Bachmann, H. Melchior, L. B. Soldano, and M. K. Smit, “Optical bandwidth and fabrication tolerances of multimode interference couplers,” *Lightwave Technology, Journal of*, vol. 12, no. 6, pp. 1004-1009. 1994.

[59] D. Dai, and S. He, “Optimization of ultracompact polarization-insensitive multimode interference couplers based on Si nanowire waveguides,” *IEEE Photonics Technology Letters*, vol. 18, no. 17-20, pp. 2017-2019, Sep.-Oct. 2006.

[60] J. Xiao, X. Liu, and X. Sun, “Design of an ultracompact MMI wavelength demultiplexer in slot waveguide structures,” *Optics Express*, vol. 15, no. 13, pp. 8300-8308, Jun. 2007.

[61] L. B. Soldano, and E. C. M. Pennings, “Optical multi-mode interference devices based on self-imaging: principles and applications,” *Journal of Lightwave Technology*, vol. 13, no. 4, pp. 615-627, Apr. 1995.

[62] E. Bonek, W. R. Leeb, A. L. Scholtz, and H. K. Philipp, “Optical PLLs see the light,” *Journal*, vol. 22, no. 13, pp. 65-70, 1983.

[63] K.-P. Ho, *Phase-modulated optical communication systems*: Springer Science Business Media Inc, 2005.

[64] T. Vallaitis, S. Bogatscher, L. Alloatti, P. Dumon, R. Baets, M. L. Scimeca, I. Biaggio, F. Diederich, C. Koos, W. Freude, and J. Leuthold, “Optical properties of highly nonlinear silicon-organic hybrid (SOH) waveguide geometries,” *Optics Express*, vol. 17, no. 20, pp. 17357-17368, Sep. 2009.

[65] A. Martinez, J. Blasco, P. Sanchis, J. V. Galan, J. Garcia-Ruperez, E. Jordana, P. Gautier, Y. Lebour, S. Hernandez, R. Guider, N. Daldosso, B. Garrido, J. M. Fedeli, L. Pavesi, and J. Marti, “Ultrafast All-Optical Switching in a Silicon-Nanocrystal-Based

Silicon Slot Waveguide at Telecom Wavelengths," *Nano Letters*, vol. 10, no. 4, pp. 1506-1511, Apr. 2010.

[66] M. Komatsu, K. Saitoh, and M. Koshiba, "Design of miniaturized silicon wire and slot waveguide polarization splitter based on a resonant tunneling," *Optics Express*, vol. 17, no. 21, pp. 19225-19234, Oct. 2009.

[67] F. Dell'Olio, and V. M. N. Passaro, "Optical sensing by optimized silicon slot waveguides," *Optics Express*, vol. 15, no. 8, pp. 4977-4993, Apr. 2007.

[68] C. A. Barrios, K. B. Gylfason, B. Sanchez, A. Griol, H. Sohlstroem, M. Holgado, and R. Casquel, "Slot-waveguide biochemical sensor," *Optics Letters*, vol. 32, no. 21, pp. 3080-3082, Nov. 2007.

[69] A. Di Falco, L. O'Faolain, and T. F. Krauss, "Chemical sensing in slotted photonic crystal heterostructure cavities," *Applied Physics Letters*, vol. 94, no. 6, 2009.

[70] P. A. Anderson, B. S. Schmidt, and M. Lipson, "High confinement in silicon slot waveguides with sharp bends," *Optics Express*, vol. 14, no. 20, pp. 9197-9202, Oct. 2006.

[71] C. Ma, Q. Zhang, and E. Van Keuren, "Right-angle slot waveguide bends with high bending efficiency," *Optics Express*, vol. 16, no. 19, pp. 14330-14334, Sep. 2008.

[72] C. Ma, S. Qi, Q. Zhang, and E. Van Keuren, "High efficiency right-angle bending structures in continuous slot waveguides," *Journal of Optics: A Pure and Applied Optics*, vol. 11, no. 10, Oct. 2009.

[73] A. Taflove, and S. C. Hagness, *Computational electrodynamics: the finite-difference time-domain method*: Artech House, 2000.

[74] Z. Sheng, D. Dai, and S. He, "Comparative study of losses in ultrasharp silicon-on-insulator nanowire bends," *IEEE Journal of Selected Topics in Quantum Electronics*, vol. 15, no. 5, pp. 1406-1412, Sep.-Oct. 2009.

[75] J.-M. Jin, *The finite element method in electromagnetics*: Wiley, 1993.

[76] Y. Ishizaka, Y. Kawaguchi, K. Saitoh, and M. Koshiba, "Design of optical XOR, XNOR, NAND, and OR logic gates based on multi-mode interference waveguides for binary-phase-shift-keyed signal," *Journal of Lightwave Technology*, vol. 29, no. 18, pp. 2836-2846, Sep. 2011.

[77] M. Koshiba, *Optical waveguide theory by the finite element method*: KTK Scientific, 1992.

[78] M. Koshiba, and K. Hirayama, "Application of finite-element method to arbitrarily shaped discontinuities in a dielectric slab wave-guide," *IEEE Proceedings-H Microwaves Antennas and Propagation*, vol. 135, no. 1, pp. 8-12, Feb. 1988.

[79] S. Yoneta, M. Koshiba, and Y. Tsuji, "Combination of beam propagation method and finite element method for optical beam propagation analysis," *Journal of Lightwave Technology*, vol. 17, no. 11, pp. 2398-2404, Nov. 1999.

[80] R. Dyczij-Edlinger, D. M. Kingsland, G. H. Peng, S. G. Perepelitsa, S. V. Polstyanko, and J. F. Lee, "Application of anisotropic absorbers to the analysis of MMIC devices

by the finite element method," *IEEE Transactions on Magnetics*, vol. 32, no. 3, pp. 854-857, May 1996.

[81] D. M. Kingsland, J. Gong, J. L. Volakis, and J. F. Lee, "Performance of an anisotropic artificial absorber for truncating finite-element meshes," *IEEE Transactions on Antennas and Propagation*, vol. 44, no. 7, pp. 975-982, Jul. 1996.

[82] A. C. Polycarpou, M. R. Lyons, and C. A. Balanis, "A two-dimensional finite element formulation of the perfectly matched layer," *IEEE Microwave and Guided Wave Letters*, vol. 6, no. 9, pp. 338-340, Sep. 1996.

[83] S. Groiss, I. Bardi, O. Biro, K. Preis, and K. R. Richter, "Finite element analysis of multiport filters using perfectly matched layers," *IEEE Transactions on Magnetics*, vol. 33, no. 2, pp. 1480-1483, Mar. 1997.

[84] J. P. Berenger, "A perfectly matched layer for the absorption of electromagnetic-waves," *Journal of Computational Physics*, vol. 114, no. 2, pp. 185-200, Oct. 1994.

[85] T. Itoh, G. Pelosi, and P. O. Silvester, Eds., *Finite element software for microwave engineering*: Wiley, 1996.

[86] [Online]. Available: http://gid.cimne.upc.es.

[87] Z. Wang, N. Zhu, Y. Tang, L. Wosinski, D. Dai, and S. He, "Ultracompact low-loss coupler between strip and slot waveguides," *Optics Letters*, vol. 34, no. 10, pp. 1498-1500, May 2009.

[88] M. Hochberg, T. Baehr-Jones, G. Wang, J. Huang, P. Sullivan, L. Dalton, and A. Scherer, "Towards a millivolt optical modulator with nano-slot waveguides," *Optics Express*, vol. 15, no. 13, pp. 8401-8410, Jun. 2007.

[89] Y. Enami, B. Yuan, M. Tanaka, J. Luo, and A. K.-Y. Jen, "Electro-optic polymer/TiO2 multilayer slot waveguide modulators," *Applied Physics Letters*, vol. 101, no. 12, 2012.

[90] Q. Liu, S. Gao, Z. Li, Y. Xie, and S. He, "Dispersion engineering of a silicon-nanocrystal-based slot waveguide for broadband wavelength conversion," *Applied Optics*, vol. 50, no. 9, pp. 1260-1265, Mar. 2011.

[91] Q. Liu, J. S. Kee, and M. K. Park, "A refractive index sensor design based on grating-assisted coupling between a strip waveguide and a slot waveguide," *Optics Express*, vol. 21, no. 5, pp. 5897-5909, Mar. 2013.

[92] Y. Ishizaka, Y. Kawaguchi, K. Saitoh, and M. Koshiba, "Three-dimensional rinite-element solutions for crossing slot-waveguides with finite core-height," *Journal of Lightwave Technology*, vol. 30, no. 21, pp. 3394-3400, Nov. 2012.

[93] N.-N. Feng, J. Michel, and L. C. Kimerling, "Optical field concentration in low-index waveguides," *IEEE Journal of Quantum Electronics*, vol. 42, no. 9-10, pp. 885-890, Sep.-Oct. 2006.

[94] P. Sanchis, J. Blasco, A. Martinez, and J. Marti, "Design of silicon-based slot waveguide configurations for optimum nonlinear performance," *Journal of Lightwave Technology*, vol. 25, no. 5, pp. 1298-1305, May 2007.

[95] K. Kakihara, N. Kono, K. Saitoh, and M. Koshiba, “Full-vectorial finite element method in a cylindrical coordinate system for loss analysis of photonic wire bends,” *Optics Express*, vol. 14, no. 23, pp. 11128-11141, Nov. 2006.

[96] H. Sun, A. Chen, D. Abeysinghe, A. Szep, and R. S. Kim, “Reduction of scattering loss of silicon slot waveguides by RCA smoothing,” *Optics Letters*, vol. 37, no. 1, pp. 13-15, Jan. 2012.

[97] Y. Halioua, A. Bazin, P. Monnier, T. J. Karle, G. Roelkens, I. Sagnes, R. Raj, and F. Raineri, “Hybrid III-V semiconductor/silicon nanolaser,” *Optics Express*, vol. 19, no. 10, pp. 9221-9231, May 2011.

[98] R. Sun, P. Dong, N.-N. Feng, C.-Y. Hong, J. Michel, M. Lipson, and L. Kimerling, “Horizontal single and multiple slot waveguides: optical transmission at $\lambda$ = 1550 nm,” *Optics Express*, vol. 15, no. 26, pp. 17967-17972, Dec. 2007.

[99] A. V. Tsarev, “Efficient silicon wire waveguide crossing with negligible loss and crosstalk,” *Optics Express*, vol. 19, no. 15, pp. 13732-13737, Jul. 2011.

[100] Y. Xu, J. Wang, J. Xiao, and X. Sun, “Design of a compact silicon-based slot-waveguide crossing,” *Applied Optics*, vol. 52, no. 16, pp. 3737-3744, Jun. 2013.

[101] C.-H. Chen, and C.-H. Chiu, “Taper-integrated multimode-interference based waveguide crossing design,” *IEEE Journal of Quantum Electronics*, vol. 46, no. 11, pp. 1656-1661, Nov. 2010.

[102] T. Tsuchizawa, K. Yamada, H. Fukuda, T. Watanabe, J. Takahashi, M. Takahashi, T. Shoji, E. Tamechika, S. Itabashi, and H. Morita, “Microphotonics devices based on silicon microfabrication technology,” *IEEE Journal of Selected Topics in Quantum Electronics*, vol. 11, no. 1, pp. 232-240, Jan.-Feb. 2005.

[103] A. V. Krasavin, and A. V. Zayats, “Guiding light at the nanoscale: numerical optimization of ultrasubwavelength metallic wire plasmonic waveguides,” *Optics Letters*, vol. 36, no. 16, pp. 3127-3129, Aug. 2011.

[104] S. A. Maier, and H. A. Atwater, “Plasmonics: Localization and guiding of electromagnetic energy in metal/dielectric structures,” *Journal of Applied Physics*, vol. 98, no. 1, 2005.

[105] C. Horvath, D. Bachman, M. Wu, D. Perron, and V. Van, “Polymer hybrid plasmonic waveguides and microring resonators,” *IEEE Photonics Technology Letters*, vol. 23, no. 17, pp. 1267-1269, Sep. 2011.

[106] C. C. Huang, “Hybrid plasmonic waveguide comprising a semiconductor nanowire and metal ridge for low-loss propagation and nanoscale confinement,” *IEEE Journal of Selected Topics in Quantum Electronics*, vol. 18, no. 6, pp. 1661-1668, Nov.-Dec. 2012.

[107] L. F. Gao, L. X. Tang, F. F. Hu, R. M. Guo, X. J. Wang, and Z. P. Zhou, “Active metal strip hybrid plasmonic waveguide with low critical material gain,” *Optics Express*, vol. 20, no. 10, pp. 11487-11495, May 2012.

[108] A. Amirhosseini, and R. Safian, “A hybrid plasmonic waveguide for the propagation of surface plasmon polariton at 1.55 μm on SOI Substrate,” *IEEE Transactions on Nanotechnology*, vol. 12, no. 6, pp. 1031-1036, Nov. 2013.

[109] M. Koshiba, *Optical waveguide analysis*: McGraw-Hill, 1992.

[110] J. B. Driscoll, X. Liu, S. Yasseri, I. Hsieh, J. I. Dadap, and R. M. Osgood, “Large longitudinal electric fields ($E_z$) in silicon nanowire waveguides,” *Optics Express*, vol. 17, no. 4, pp. 2797-2804, Feb. 2009.

[111] I. D. Rukhlenko, M. Premaratne, and G. P. Agrawal, “Effective mode area and its optimization in silicon-nanocrystal waveguides,” *Optics Letters*, vol. 37, no. 12, pp. 2295-2297, Jun. 2012.

[112] J. T. Robinson, L. Chen, and M. Lipson, “On-chip gas detection in silicon optical microcavities,” *Optics Express*, vol. 16, no. 6, pp. 4296-4301, Mar. 2008.

# List of Author's Publications

## Papers

(1) T. Uematsu, T. Kitayama. Y. Ishizaka, K. Saitoh, "Ultra-broadband silicon-wire polarization beam combiner/splitter based on a wavelength insensitive coupler with a point-symmetrical configuration," *IEEE Photonics Journal*, vol. 6, no. 1, pp. 4500108-1-4500108-8, Feb. 2014.

(2) Y. Ishizaka, K. Saitoh, and M. Koshiba, "Transmission-efficient structures of bent and crossing silicon slot waveguides," *IEEE Photonics Journal*, vol. 5, no. 5, pp. 6601809 -1-6601809-9, Oct. 2013.

(3) S. Makino, Y. Ishizaka, K. Saitoh, and M. Koshiba, "Proposal of coupled ring resonator based on one-dimensional photonic crystal nanocavity," *IEEE/OSA Journal of Lightwave Technology*, vol. 31, no. 15, pp. 2565-2569, Aug. 2013.

(4) S. Makino, Y. Ishizaka, K. Saitoh, and M. Koshiba, "Slow-light-enhanced nonlinear characteristics in slot waveguides composed of photonic crystal nanobeam cavities," *IEEE Photonics Journal*, vol. 5, no. 2700309-1-700309-9, Apr. 2013.

(5) Y. Ishizaka, Y. Kawaguchi, K. Saitoh, and M. Koshiba, "Three-dimensional finite-element solutions for crossing slot-waveguides with finite core-height," *IEEE/OSA Journal of Lightwave Technology*, vol. 30, no. 21, pp. 3394-3400, Nov. 2012.

(6) T. Uematsu, Y. Ishizaka, Y. Kawaguchi, K. Saitoh, and M Koshiba, "Design of a compact two-mode multi/demultiplexer consisting of multi-mode interference waveguides and a wavelength insensitive phase shifter for mode-division multiplexing transmission," *IEEE/OSA Journal of Lightwave Technology*, vol. 30, no. 15, pp. 2421-2426, Aug. 2012.

(7) Y. Ishizaka, Y. Kawaguchi, K. Saitoh, and M. Koshiba, "Design of optical XOR, XNOR, NAND, and OR logic gates based on multi-mode interference waveguides for binary-phase-shift-keyed signal," *IEEE/OSA Journal of Lightwave Technology*, vol. 29, no. 18, pp. 2836-2846, Sep. 2011.

(8) Y. Ishizaka, Y. Kawaguchi, K. Saitoh, and M. Koshiba, "Design of ultra compact all-optical XOR and AND logic gates with low power consumption," *Optics Communications*, vol. 284, no. 14, pp. 3528-3533, Jul. 2011.

## International Conferences

(1) T. Uematsu, N. Hanzawa, K. Saitoh, Y. Ishizaka, K. Masumoto, T. Sakamoto, T. Matsui, K. Tsujikawa, and F. Yamamoto, “PLC-type LP11 mode rotator with single-trench waveguide for mode-division multiplexing transmission”, Optical Fiber Communication Conference and National Fiber Optic Engineers Conference (OFC/NFOEC), Mar. 2014.

(2) S. Makino, Y. Ishizaka, K. Saitoh, and M. Koshiba, “Structural dependence of nonlinear characteristics in coupled resonator optical waveguides based on slotted nanobeam cavities,” Proceedings of the Frontiers in Optics 2013/Laser Science XXIX (FiO/LS), FW4E.5, Orlando, USA, Oct. 2013.

(3) Y. Ishizaka, K. Saitoh, and M. Koshiba, “Surface plasmon nanocavities composed of metallic wall and 1-D photonic crystal,” Proceedings of the IEEE Photonics Conference (IPC), pp. 627-628, Bellevue, USA, Sep. 2013.

(4) Y. Ishizaka, K. Saitoh, and M. Koshiba, “Metallic wall-based plasmon nanocabities with 1-D photonic crystals,” Proceedings of the IEEE Photonics Society Summer Topical Meeting, pp. 58-59, Hawaii, USA, Jul. 2013.

(5) S. Makino, Y. Ishizaka, K. Saitoh, and M. Koshiba, “A proposal of coupled resonator optical waveguides based on slotted nanobeam cavities,” Proceedings of the IEEE Photonics Society Summer Topical Meeting, pp. 46-47, Hawaii, USA, Jul. 2013.

(6) S. Makino, Y. Ishizaka, K. Saitoh, and M. Koshiba, “Structural dependence of nonlinear characteristics in slot waveguides composed of photonic crystal nanobeam cavities,” Proceedings of the Conference on Lasers and Electro-Optics Pacific Rim (CLEO-PR), TuPI-4, Kyoto, Japan, Jun.-Jul. 2013.

(7) M. Nagai, Y. Ishizaka, K. Saitoh, and M. Koshiba, “Propagation length and coupling characteristics of a hybrid plasmonic waveguide with a uniform silica layer,” Proceedings of the Conference on Lasers and Electro-Optics Pacific Rim (CLEO-PR), TuPI-16, Kyoto, Japan, Jun.-Jul. 2013.

(8) Y. Ishizaka, Y. Kawaguchi, K. Saitoh, and M. Koshiba, “Transmission characteristics of crossing slot-waveguides with finite core-height,” Proceedings of the OptoElectronics and Communications Conference (OECC), pp. 887-888, Busan, Korea, Jul. 2012.

(9) Y. Ishizaka, Y. Kawaguchi, K. Saitoh, and M. Koshiba, “An architecture proposal of reconfigurable optical logic gates for BPSK signal,” Proceedings of the OptoElectronics and Communications Conference (OECC), pp.699-700, Kaohsiung, Taiwan, Jul. 2011.

(10) Y. Ishizaka, Y. Kawaguchi, K. Saitoh, and M. Koshiba, “Design of all-optical XOR and AND logic gates based on multi-mode interference devices,” Proceedings of the International Conference on Advanced Optoelectronics & Lasers (CAOL), pp. 53-55, Sevastopol, Ukraine, Sep. 2010.

## Domestic Conferences

(1) 牧野 俊太郎, 石坂 雄平, 齊藤 晋聖, “横スロット導波路に基づく 1-D PC-CROW の提案,” 電子情報通信学会大会総合大会，C-3-39，新潟，2014 年 3 月.

(2) 長井 優，石坂 雄平，齊藤 晋聖，“ハイブリッドプラズモニック導波路に基づくフォトニック-プラズモニックモード変換器の提案,”電子情報通信学会大会総合大会，C-3-40，新潟，2014 年 3 月.

(3) 佐藤 孝憲，牧野 俊太郎，石坂 雄平，齊藤 晋聖，“3 次元有限要素モードソルバによる 1-D PC-CROW の非線形特性調査,” 電子情報通信学会大会総合大会，C-3-41，新潟，2014 年 3 月.

(4) 石坂 雄平，長井 優，齊藤 晋聖，小柴 正則，“非主要電界成分と結合したプラズモニックモードに関する検討,”電子情報通信学会ソサイエティ大会, C-3-64, 福岡，2013 年 9 月.

(5) 北山 哲也，石坂 雄平，齊藤 晋聖，“位相情報に基づく AND 光論理ゲートの設計,” 電子情報通信学会ソサイエティ大会，C-3-2，福岡，2013 年 9 月.

(6) 牧野 俊太郎，石坂 雄平，齊藤 晋聖，小柴 正則，“スロットナノビーム共振器に基づく結合共振器導波路の非線形特性調査,” 電子情報通信学会ソサイエティ大会，C-3-7，福岡，2013 年 9 月.

(7) 長井 優，石坂 雄平，齊藤 晋聖，“一様なシリカ層を有するハイブリッドプラズモニック導波路を用いたモード変換器の提案,” 電子情報通信学会ソサイエティ大会，C-3-65，福岡，2013 年 9 月.

(8) 植松 卓威，齊藤 晋聖，半澤 信智，坂本 泰志，松井 隆，辻川 恭三，増本 浩平，石坂 雄平，小柴 正則，“モード多重伝送のための平面光導波路型モード合分波器の広帯域化に関する検討,”電子情報通信学会ソサイエティ大会, C-3-78, 福岡，2013 年 9 月.

(9) 石坂 雄平，齊藤 晋聖，小柴 正則，“3 次元ベクトル有限要素法によるスロット交差導波路解析,” 電子情報通信学会総合大会，CS-5-6，岐阜，2013 年 3 月.

(10) 牧野 俊太郎，石坂 雄平，齊藤 晋聖，小柴 正則，“1-D PC-CROW に基づくスロット導波路における非線形特性調査,” 電子情報通信学会総合大会，C-3-47，岐阜，2013 年 3 月.

(11) 長井 優，石坂 雄平，齊藤 晋聖，小柴 正則，“一様なシリカ層を有するハイブリッドプラズモニック導波路の結合特性評価,” 電子情報通信学会総合大会，C-3-51，岐阜，2013 年 3 月.

(12) 長井 優，石坂 雄平，小松 正明，齊藤 晋聖，小柴 正則，“一様なシリカ層を有するハイブリッドプラズモニック導波路の伝搬長評価,” 電気・情報関係学会北海道支部連合大会，17，札幌，2012 年 10 月.

(13) 牧野 俊太郎，石坂 雄平，川口 雄揮，齊藤 晋聖，小柴 正則，“1 次元フォトニック結晶結合共振器導波路の非線形特性評価,” 電子情報通信学会ソサイエティ大会，C-3-46，富山，2012 年 9 月.

(14) 植松 卓威，石坂 雄平，小松 正明，齊藤 晋聖，小柴 正則，“広帯域点対称 MZI 型偏波スプリッタの設計，”電子情報通信学会ソサイエティ大会，C-3-29，富山，2012 年 9 月．

(15) 石坂 雄平，齊藤 晋聖，小柴 正則，“フォトニック結晶微小共振器解析のための 3 次元ベクトル有限要素法，”電子情報通信学会ソサイエティ大会，C-3-44，富山，2012 年 9 月．

(16) 植松 卓威，石坂 雄平，川口 雄揮，齊藤 晋聖，小柴 正則，“MMI 導波路型 2 モード合分波器の特性評価，”電子情報通信学会総合大会，C-3-88，岡山，2012 年 3 月．

(17) 石坂 雄平，川口 雄揮，齊藤 晋聖，小柴 正則，“垂直結合器を有する立体スロット交差導波路に関する検討，”電子情報通信学会総合大会，C-3-48，岡山，2012 年 3 月．

(18) 石坂 雄平，川口 雄揮，齊藤 晋聖，小柴 正則，“3 次元ベクトル有限要素法によるスロット交差導波路の特性評価，”電子情報通信学会ソサイエティ大会，C-3-54，札幌，2011 年 9 月．

(19) 石坂 雄平，川口 雄揮，齊藤 晋聖，小柴 正則，“BPSK ラベル処理のための NAND 光論理回路の設計，”電子情報通信学会総合大会，C-3-75，東京，2011 年 3 月．

(20) 石坂 雄平，川口 雄揮，齊藤 晋聖，小柴 正則，“フォトニック結晶導波路を用いたマルチモード干渉デバイスによる AND 光論理回路の設計，”電子情報通信学会ソサイエティ大会，C-3-5，大阪，2010 年 9 月．

## Technical Reports

(1) 長井 優，石坂 雄平，齊藤 晋聖，“一様なシリカ層を有するハイブリッドプラズモニック導波路の基本特性に関する調査，”光エレクトロニクス研究会，OPE2013-89，函館，2013 年 8 月．

(2) 石坂 雄平，齊藤 晋聖，小柴 正則，“3 次元ベクトル有限要素法の開発とその光導波路・共振器解析への応用，”光エレクトロニクス研究会，熱海，2013 年 4 月．

(3) 石坂 雄平，齊藤 晋聖，小柴 正則，“金属壁とフォトニック結晶で挟み込んだ表面プラズモン共振器の 3 次元ベクトル有限要素解析，”電子情報通信学会光エレクトロニクス研究会，OPE2013-28，大阪，2013 年 1 月，

(4) 石坂 雄平，齊藤 晋聖，小柴 正則，“フォトニック結晶微小共振器設計のための 3 次元ベクトル有限要素法ソルバの開発，”電子情報通信学会エレクトロニクスシミュレーション研究会，EST2012-36，札幌，2012 年 7 月．

## Awards

(1) IEEE 札幌支部から「2013 年若手研究者年間優秀論文賞　最優秀論文賞」を受賞，2014 年 2 月 6 日．

(2) 電子情報通信学会 エレクトロニクスソサイエティから「エレクトロニクスソサイエティ学生奨励賞」を受賞，2013 年 9 月 24 日．

(3) 電子情報通信学会 光エレクトロニクス(OPE)研究会から「2013 年度光エレクトロニクス研究会　学生ポスター優秀賞」を受賞，2013 年 4 月 25 日．

(4) IEEE 札幌支部から「2012 年若手研究者年間優秀論文賞　最優秀論文賞」を受賞，2013 年 1 月 28 日．

(5) 電子情報通信学会北海道支部から「平成 23 年度電子情報通信学会北海道支部学生員奨励賞」を受賞，2012 年 3 月 22 日．